WIRELESS SENSOR NETWORK OPTIMIZATION FOR RADIO TOMOGRAPHIC IMAGING

THESIS

Grant T. Nafziger, Captain, USAF

AFIT-ENG-MS-20-M-047

DEPARTMENT OF THE AIR FORCE
AIR UNIVERSITY

AIR FORCE INSTITUTE OF TECHNOLOGY

Wright-Patterson Air Force Base, Ohio

DISTRIBUTION STATEMENT A
APPROVED FOR PUBLIC RELEASE; DISTRIBUTION UNLIMITED.

The views expressed in this document are those of the author and do not reflect the official policy or position of the United States Air Force, the United States Department of Defense or the United States Government. This material is declared a work of the U.S. Government and is not subject to copyright protection in the United States.

AFIT-ENG-MS-20-M-047

WIRELESS SENSOR NETWORK OPTIMIZATION FOR RADIO TOMOGRAPHIC IMAGING

THESIS

Presented to the Faculty

Department of Electrical and Computer Engineering

Graduate School of Engineering and Management

Air Force Institute of Technology

Air University

Air Education and Training Command

in Partial Fulfillment of the Requirements for the

Degree of Master of Science in Electrical Engineering

Grant T. Nafziger, B.S.E.E.

Captain, USAF

March 19, 2020

DISTRIBUTION STATEMENT A
APPROVED FOR PUBLIC RELEASE; DISTRIBUTION UNLIMITED.

AFIT-ENG-MS-20-M-047

WIRELESS SENSOR NETWORK OPTIMIZATION FOR RADIO TOMOGRAPHIC IMAGING

THESIS

Grant T. Nafziger, B.S.E.E.
Captain, USAF

Committee Membership:

Dr. Richard K. Martin, Ph.D
Chair

Dr. Michael A. Temple, Ph.D
Member

Maj J. Addison Betances, Ph.D
Member

AFIT-ENG-MS-20-M-047

Abstract

Radio tomographic imaging (RTI) is a form of device-free, passive localization (DFPL) that uses a wireless sensor network (WSN) typically made up of affordable, low-power transceivers. The intent for RTI is to have the ability to monitor a given area, localizing and tracking obstructions within. The specific advantages rendered by RTI include the ability to provide imaging, localization, and tracking where other well developed methods like optical surveillance fall short. RTI can function through optical obstructions such as smoke and even physical obstructions like walls. This provides a tool that is particularly valuable for tactical operations like emergency response and military operations in urban terrain (MOUT).

Many methods to optimize the performance of RTI systems have been explored, but little work that focuses on the sequence of transceiver reports can be found in the body of literature. This thesis provides an exploration of the effects from attempting to optimize the transmission sequence in a WSN by creating a metric to quantify the value of the information a transceiver will report and using it to develop a dynamic, utility-driven, token passing process.

After deriving a metric from the Fisher information matrix of the imaging solution, it was combined with a weighting based on the time each node last reported across the WSN. Modeling and simulation was performed to determine if the novel transmission sequence provided any benefit to the localization and tracking performance. The results showed a small improvement in two different localization methods when packet loss in the WSN reached 50%. These results provide a proof-of-concept that warrants further exploration and suggest that performance improvements may be realized by implementing a transmission sequence based on the metric developed in this thesis.

Acknowledgements

I would like to thank my advisor, Dr. Richard Martin, for the steadfast guidance and sounding board for ideas, concerns, and successes that he provided throughout this process.

Grant T. Nafziger

Table of Contents

Page

Abstract iv

Acknowledgements v

List of Figures viii

List of Tables xiv

I. Introduction 1

1.1 Problem Background 1
1.2 Research Motivation 2
1.3 Research Objectives 3
1.4 Document Overview 4

II. Background and Literature Review 5

2.1 Radio Tomographic Imaging 5
2.1.1 Wireless Sensor Networks 6
2.1.2 Mathematical Models 7
2.1.2.1 Linear Formulation 8
2.1.2.2 Weight Matrix 10
2.1.2.3 Noise Model 14
2.1.3 Image Estimation 14
2.1.3.1 Regularization 15
2.2 Position Tracking 19
2.2.1 Maximum A Posteriori 20
2.2.2 K-Means Clustering 20
2.2.3 Particle Filtering 21
2.2.4 Kalman Filtering 22
2.2.4.1 Application in RTI 26

III. Methodology 29

3.1 Modeling and Simulation 29
3.1.1 Processing Methods 29
3.1.1.1 Sequential Processing 29
3.1.1.2 Information, Currency, History, and Utility 33
3.1.2 Wireless Sensor Network Model 37
3.1.3 Position Tracking 42
3.2 Simulation Set-up 43

Page

IV. Results and Analysis 46

4.1 Node Selection Based on Highest Utility 46
4.2 Position Tracking 52
4.2.1 Experiment 1 Results 52
4.2.2 Experiment 2 Results 61
4.2.3 Experiment 3 Results 63
4.2.4 Experiment 4 Results 65
4.2.5 Experiment 5 Results 67

V. Conclusions 69

5.1 Future Work 70

Appendix A. Additional Results 72

1.1 Experiment 2 Results 72
1.2 Experiment 3 Results 76
1.3 Experiment 4 Results 80
1.4 Experiment 5 Results 84
Bibliography 88
Acronyms 94

List of Figures

Figure Page

1. Illustrative wireless sensor network diagram. 7

2. Measurement matrix with time synchronous columns. 31

3. Example reports by transmitter for the first round of communication. 32

4. Example reports by transmitter for the second round of communication. 33

5. All links made with node $n = 54$, highlighted in red. 39

6. Modeled WSN with scene pixel outline and dynamic target path. 40

7. Modeled WSN with scene pixel outline utilizing 28 nodes and 2 ft node spacing. 41

8. Illustration of three paths with randomized starting points. 44

9. Number of reports per node for 108000 reports, arranged in the WSN setup. 47

10. Information value for each node overlaid with number of reports per node for 108000 reports selected for highest utility. 48

11. Utility and history for node 54 over time. 49

12. Currency values for links between nodes 54 and 24 (high information value) and nodes 54 and 2 (low information value). 50

13. Close-up on currency values for links between nodes 54 and 24 (high information value) and nodes 54 and 2 (low information value) in the first four seconds. 50

14. Illustration of links starting at node 54 and ending at nodes 2 (low information link) and 24 (high information link). 51

Figure Page

15. Position tracking results for one run of the MAP and image-based centroid localization methods for the x (top) and y (bottom) directions using method 3. 53

16. Experiment 1 RMSE and K-means averaged dispersion with 95% confidence intervals over 1000 realizations of the dynamic path during steady state runtime, with 0% packet loss. 54

17. Experiment 1 RMSE and K-means averaged dispersion with 95% confidence intervals over 1000 realizations of the dynamic path for full path duration, with 0% packet loss. 55

18. Experiment 1 RMSE versus time for the three methods averaged over 1000 realizations, shaded portion indicates transient data that was removed to obtain the "steady-state" RMSE results. 56

19. Experiment 1 RMSE and K-means averaged dispersion with 95% confidence intervals over 1000 realizations of the dynamic path during steady state runtime, with 20% packet loss. 57

20. Experiment 1 RMSE and K-means averaged dispersion with 95% confidence intervals over 1000 realizations of the dynamic path for full path duration, with 20% packet loss. 58

21. Experiment 1 RMSE and K-means averaged dispersion with 95% confidence intervals over 1000 realizations of the dynamic path during steady state runtime, with 50% packet loss. 58

22. Experiment 1 RMSE and K-means averaged dispersion with 95% confidence intervals over 1000 realizations of the dynamic path for full path duration, with 50% packet loss. 59

23. Experiment 1 RMSE and K-means averaged dispersion with 95% confidence intervals over 1000 realizations of the dynamic path during steady state runtime, with 85% packet loss. 59

Figure Page

24. Experiment 1 RMSE and K-means averaged dispersion with 95% confidence intervals over 1000 realizations of the dynamic path for full path duration, with 85% packet loss. 60

25. Experiment 2 RMSE and K-means averaged dispersion with 95% confidence intervals over 1000 realizations of the dynamic path during steady state runtime, with 0% packet loss. 61

26. Experiment 2 RMSE and K-means averaged dispersion with 95% confidence intervals over 1000 realizations of the dynamic path during steady state runtime, with 50% packet loss. 62

27. Experiment 3 RMSE and K-means averaged dispersion with 95% confidence intervals over 1000 realizations of the dynamic path during steady state runtime, with 0% packet loss. 63

28. Experiment 3 RMSE and K-means averaged dispersion with 95% confidence intervals over 1000 realizations of the dynamic path during steady state runtime, with 50% packet loss. 64

29. Experiment 4 RMSE and K-means averaged dispersion with 95% confidence intervals over 1000 realizations of the dynamic path during steady state runtime, with 0% packet loss. 65

30. Experiment 4 RMSE and K-means averaged dispersion with 95% confidence intervals over 1000 realizations of the dynamic path during steady state runtime, with 50% packet loss. 66

31. Experiment 5 RMSE and K-means averaged dispersion with 95% confidence intervals over 1000 realizations of the dynamic path during steady state runtime, with 0% packet loss. 67

32. Experiment 5 RMSE and K-means averaged dispersion with 95% confidence intervals over 1000 realizations of the dynamic path during steady state runtime, with 50% packet loss. 68

Figure Page

33. Experiment 2 RMSE and K-means averaged dispersion with 95% confidence intervals over 1000 realizations of the dynamic path for full path duration, with 0% packet loss. 72

34. Experiment 2 RMSE and K-means averaged dispersion with 95% confidence intervals over 1000 realizations of the dynamic path during steady state runtime, with 20% packet loss. 73

35. Experiment 2 RMSE and K-means averaged dispersion with 95% confidence intervals over 1000 realizations of the dynamic path for full path duration, with 20% packet loss. 73

36. Experiment 2 RMSE and K-means averaged dispersion with 95% confidence intervals over 1000 realizations of the dynamic path for full path duration, with 50% packet loss. 74

37. Experiment 2 RMSE and K-means averaged dispersion with 95% confidence intervals over 1000 realizations of the dynamic path during steady state runtime, with 85% packet loss. 74

38. Experiment 2 RMSE and K-means averaged dispersion with 95% confidence intervals over 1000 realizations of the dynamic path for full path duration, with 85% packet loss. 75

39. Experiment 3 RMSE and K-means averaged dispersion with 95% confidence intervals over 1000 realizations of the dynamic path for full path duration, with 0% packet loss. 76

40. Experiment 3 RMSE and K-means averaged dispersion with 95% confidence intervals over 1000 realizations of the dynamic path during steady state runtime, with 20% packet loss. 77

41. Experiment 3 RMSE and K-means averaged dispersion with 95% confidence intervals over 1000 realizations of the dynamic path for full path duration, with 20% packet loss. 77

Figure Page

42. Experiment 3 RMSE and K-means averaged dispersion with 95% confidence intervals over 1000 realizations of the dynamic path for full path duration, with 50% packet loss. 78

43. Experiment 3 RMSE and K-means averaged dispersion with 95% confidence intervals over 1000 realizations of the dynamic path during steady state runtime, with 85% packet loss. 78

44. Experiment 3 RMSE and K-means averaged dispersion with 95% confidence intervals over 1000 realizations of the dynamic path for full path duration, with 85% packet loss. 79

45. Experiment 4 RMSE and K-means averaged dispersion with 95% confidence intervals over 1000 realizations of the dynamic path for full path duration, with 0% packet loss. 80

46. Experiment 4 RMSE and K-means averaged dispersion with 95% confidence intervals over 1000 realizations of the dynamic path during steady state runtime, with 20% packet loss. 81

47. Experiment 4 RMSE and K-means averaged dispersion with 95% confidence intervals over 1000 realizations of the dynamic path for full path duration, with 20% packet loss. 81

48. Experiment 4 RMSE and K-means averaged dispersion with 95% confidence intervals over 1000 realizations of the dynamic path for full path duration, with 50% packet loss. 82

49. Experiment 4 RMSE and K-means averaged dispersion with 95% confidence intervals over 1000 realizations of the dynamic path during steady state runtime, with 85% packet loss. 82

50. Experiment 4 RMSE and K-means averaged dispersion with 95% confidence intervals over 1000 realizations of the dynamic path for full path duration, with 85% packet loss. 83

Figure Page

51. Experiment 5 RMSE and K-means averaged dispersion with 95% confidence intervals over 1000 realizations of the dynamic path for full path duration, with 0% packet loss. 84

52. Experiment 5 RMSE and K-means averaged dispersion with 95% confidence intervals over 1000 realizations of the dynamic path during steady state runtime, with 20% packet loss. 85

53. Experiment 5 RMSE and K-means averaged dispersion with 95% confidence intervals over 1000 realizations of the dynamic path for full path duration, with 20% packet loss. 85

54. Experiment 5 RMSE and K-means averaged dispersion with 95% confidence intervals over 1000 realizations of the dynamic path for full path duration, with 50% packet loss. 86

55. Experiment 5 RMSE and K-means averaged dispersion with 95% confidence intervals over 1000 realizations of the dynamic path during steady state runtime, with 85% packet loss. 86

56. Experiment 5 RMSE and K-means averaged dispersion with 95% confidence intervals over 1000 realizations of the dynamic path for full path duration, with 85% packet loss. 87

List of Tables

Table Page

1. Summary of information and time-based metrics. 38

2. Parameters used for WSN model. 41

3. List of experiments conducted. 45

WIRELESS SENSOR NETWORK OPTIMIZATION FOR RADIO TOMOGRAPHIC IMAGING

I. Introduction

This chapter presents a brief background of the research topic area and provides context and motivation for the research accomplished in the thesis. It presents the specific research objectives pursued in the thesis and provides an overview of the remainder of the document.

1.1 Problem Background

Radio tomographic imaging (RTI) uses a network of transceivers, termed a wireless sensor network (WSN), that produces an image using the amount of attenuation calculated on the links between tranceivers. The imaging is essentially a map of the attenuation in the scene contained within the boundaries of the WSN, where obstructions attenuate the radio frequency (RF) signals to a greater degree than free space and show up in the imaging as regions of higher attenuation. This is accomplished by recording the received signal strength (RSS) between transceiver pairs, and the imaging or the raw RSS measurements can be used to localize and track obstructions inside the WSN. This technique does not require an obstruction to have any type of device and falls under a broader category of localization techniques called device-free, passive localization (DFPL) often referred to simply as device-free localization (DFL) [1–5]. Various other methods for DFPL exist to include radio grids where the tranceivers are in a grid in the scene rather than around the perimeter of the scene; RF fingerprinting, where a map is created and localization occurs by

comparing the network measurements to a database of measurements with targets at various locations; RF backscatter, where scattering caused by obstructions is used rather than attenuation on line-of-sight links; and passive radar, that uses signals of opportunity to illuminate targets rather than transmitting its own radar pulses [1].

The range of devices suitable for passive imaging methods mentioned above is also wide. Simple transceivers are typically used for RTI as a way to make it a cost-effective form of surveillance. One widely used type of transceiver is called a TelosB mote, and became a de-facto standard for RTI systems after Wilson and Patwari utilized them successfully for an RTI system in [6]. Many of the simple transceivers are IEEE 802.15.4 compliant devices, including the IPv6 Over Low-Power Wireless Personal Area Networks (6LoWPAN) due to the low power requirements and low cost for 802.15.4 compliant radio integrated circuits [1, 5, 7]. Some implementations use the simplest hardware possible by only recording whether a packet was received or dropped and building the image based on the resultant binary matrix [8]. The RF methods can also be achieved using IEEE 802.11 (Wi-Fi) compliant devices [1, 5]. Additionally, ultra-wideband (UWB) radios can be used for both RTI and RF backscatter imaging [1, 9], and passive radar uses highly prevalent RF signals like those used for cellular phones and Wi-Fi [1].

1.2 Research Motivation

RTI systems have been proven useful for localization in a variety of scenarios [6, 10, 11]. These applications can be put to great use in tactical operations including emergency response situations like structure fires and active shooters, military operations in urban terrain (MOUT) where situational awareness on the interior of a building can provide life-saving information, and general surveillance of controlled areas where typical methods may be cost-prohibitive or inappropriate for the specific

application. These potential uses have made RTI a promising area of research, with many publications presenting methods to improve or optimize RTI systems for better imaging results [2, 3, 12–19]. Various publications have also explored improving the measurement models used in RTI [12, 18, 20–29]. Additionally, RTI becomes more difficult when tracking multiple targets, and solutions have been sought to resolve this problem as well [4, 30]. The central problem explored in this thesis is an understudied area of RTI: the order of transmission of the nodes in the WSN, which implicitly affects the relative frequency of transmission of the nodes.

1.3 Research Objectives

The lack of research focused on optimizing RTI systems by adjusting the sequence in which the nodes report RSS measurements provides an open opportunity for this thesis to explore the potential for such an approach as a means to improve the localization and tracking capabilities of RTI. Specifically, this thesis will focus on creating a metric by which to judge the value of a given node's reported information at a given time in the transmission sequence. Discussed in chapter III, the utility metric is based in part on the Fisher information matrix derived by Wilson and Patwari in [6].

The results in this thesis will mainly consist of generation of the selection metrics developed and used for dynamically selecting the next node for transmit, enumeration of the simulated relative frequency of transmission for each node, and simulated location tracking results for dynamic scenes using dynamic node selection and sequential transmission methods.

The output of the thesis will be a comparison of the simulated location tracking results between the two modeled transmission order methods in addition to graphical representations of how the utility metric affects the transmission order. The results and output will mainly provide a framework to apply the dynamic selection method

to future simulations and experiments to further test potential benefits.

1.4 Document Overview

The thesis document is structured into five chapters. This chapter provides a brief overview of the problem background, specific research problem statement, and document structure. Chapter II provides a detailed background on RTI including models, imaging solutions, and target tracking methods. Chapter III provides a description of the specific steps and methodology taken to address the objectives stated above, and chapter IV presents and discusses the subsequent results. Finally, chapter V provides a summary of the results and discussion of their significance to RTI and presents a context for which the work accomplished in this thesis can be applied in future work to further explore the concepts presented or potentially benefit the conduct of future experiments.

II. Background and Literature Review

This chapter reviews existing literature for previous work that has been conducted on radio tomographic imaging (RTI) and device-free localization (DFL). It explores multiple mathematical bases for localization of obstructions within wireless sensor networks, and reviews some of the methods that have been implemented to improve RTI systems. It also covers work that has occurred on the Air Force Institute of Technology's RTI system.

2.1 Radio Tomographic Imaging

Radio tomographic imaging is a form of DFL that provides a method for localizing obstructions inside the perimeter of a wireless sensor network (WSN). This form of localization does not rely on the objects being tracked to be tagged in any way, like with a radio frequency identification device (RFID) chip or Global Positioning System (GPS) receiver [1]. A typical RTI system uses the received signal strength (RSS) between pairs of sensors to detect possible obstructions and localize them. The work accomplished in [6] lays a fundamental groundwork for setting up functional RTI systems, and provides a mathematical basis for estimating the position of obstructions within a WSN.

Since the publication of [6] many other methods of DFL have been explored, including the implementation of methods to improve RTI that uses WSNs. One particular method used to enhance RTI that will be further explored in this thesis was the implementation of Bayesian filtering methods in [16]. Additionally, physical methods have also been found to improve the performance of RTI systems as in [11] where antennae on the sensors in the network were rotated to improve imaging and localization performance.

2.1.1 Wireless Sensor Networks

The work in [6] provides much of the information needed for setting up a WSN to perform RTI, short of providing specific details on the sensors within the network. A sensor network is set up with radio frequency (RF) transceivers around the perimeter of a scene, where the transceivers are referred to as nodes in [6]. The transceivers form a unique link with every other transceiver in the network, and report the signal strength on that link. When an obstruction passes through the link, the signal is attenuated. Using the RSS to detect attenuation, the obstruction can be localized within the perimeter of the WSN. Figure 1 shows one such configuration modeled after figure 1 in [6].

Figure 1 above illustrates how the links between nodes can contribute information to localize objects within the WSN. A grid can be overlaid, where each square represents a pixel in the estimated image. Links passing through and near pixels provide information used to determine whether an obstruction is present. This is also shown in [6], where the lower bound on the mean-squared error is reduced as a result of more links crossing a given pixel.

Token Passing Protocol Many RTI systems use a token passing protocol in a time division multiple access (TDMA) communication scheme such that each node has a turn to send a report to the base station and all other nodes [2, 3, 6, 10, 11, 31]. After the first node transmits it passes the token to the next node, or if it fails to transmit within the allotted time window the token is automatically passed to the next node in the sequence. This allows the use of reasonably simple devices that will not interfere with each other as they take turns reporting RSS around the WSN. Typically each node will take its turn sequentially such that the reporting order is $\{1, 2, 3, \ldots, N-1, N\}$ where N is the total number of nodes [2, 3, 6, 10, 11, 31].

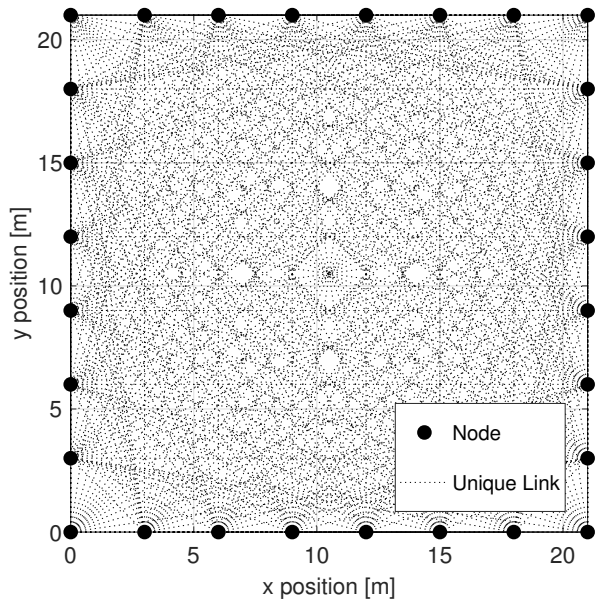

Figure 1: Illustrative wireless sensor network diagram.

Specifically, an open-source protocol developed by the Sensing and Processing Across Networks (SPAN) laboratory at the Department of Electrical Engineering at the University of Utah named "spin" is used in the Air Force Institute of Technology (AFIT) RTI system. As configured, it allocates evenly-divided time slots for each transceiver across one second. If a transceiver fails to transmit within its allotted time slot, it is given an 80 ms window to re-transmit before it times out and the base station passes the token to the next transceiver in the sequence.

2.1.2 Mathematical Models

Localization cannot occur without utilizing models for the environment as well as the RSS for a given link. Using these models, the system is represented overall using a linear model, allowing an approach that is very common in estimation. The problem presents some unique challenge, primarily in that RTI systems rely on ill-posed inverses that require methods such as Tikhonov Regularization to prevent small

noise variances from overwhelming any signal data upon inversion, which is described in [6, 32, 33].

2.1.2.1 Linear Formulation

One of the most widely-used models for RTI in the literature is the linear formulation as used by Wilson and Patwari in [6], whose methods and general approach can also be seen in [2, 3, 11, 14, 21, 22, 29, 33].

As shown in [6], the RSS of a given link, i, can be represented mathematically by

$$y_i(t) = P_i - L_i - S_i(t) - F_i(t) - v_i(t) \tag{2.1}$$

where [6]

- P_i is the transmitted power
- $S_i(t)$ is the "shadowing" loss, or loss due to objects attenuating the signal
- $F_i(t)$ is the fading loss, caused by interference in the presence of multipath
- L_i is the static loss due to distance, device characteristics, etc.
- $v_i(t)$ is the measurement noise

all of which are measured in decibels. In the linear formulation the major item of interest is $S_i(t)$ which can be described as [6]

$$S_i(t) = \sum_{j=1}^{N} w_{ij} x_j(t) \tag{2.2}$$

where w_{ij} is the "weight" - a measure of the impact link i has on pixel j, and $x_j(t)$ is the attenuation in pixel j at time t. Operating under the assumption that many of the losses are static, the change in RSS can be found by subtracting a measurement

of the scene with no obstructions from a measurement of the scene when obstructions are present [6]. This requires a calibration period with an empty scene, which is both a contextual and logistical consideration for deploying an RTI system that uses the linear formulation. It does allow for the change in RSS on a given link between calibration time t_c and time t to be represented as [6]

$$\triangle y_i = y_i(t) - y_i(t_c) = S_i(t) - S_i(t_c) + F_i(t) - F_i(t_c) + v_i(t) - v_i(t_c) \tag{2.3}$$

The differences in fading loss $F_i(t)$ and measurement noise, $v_i(t)$ can be combined into a single noise term n_i, and (2.2) can be incorporated to turn (2.3) into:

$$\triangle y_i = \sum_{j=1}^{N} w_{ij} x_j(t) - \sum_{j=1}^{N} w_{ij} x_j(t_c) + n_i \tag{2.4}$$

$$\triangle y_i = \sum_{j=1}^{N} w_{ij} (x_j(t) - x_j(t_c)) + n_i \tag{2.5}$$

$$\triangle y_i = \sum_{j=1}^{N} w_{ij} \triangle x_j + n_i \tag{2.6}$$

This can then be represented in vector and matrix form as:

$$\triangle \mathbf{y} = \mathbf{W} \triangle \mathbf{x} + \mathbf{n} \tag{2.7}$$

where $\triangle \mathbf{y}$ is a vector of the change in RSS on each link, $\triangle \mathbf{x}$ is a vector of the change in attenuation in each pixel, $\mathbf{n}$ is a vector of the measurement noise on each link, and $\mathbf{W}$ is the weight matrix containing the per-pixel weights for each link [6]. Represented more simply, the calibration can be taken as given in further discussion and the linear form of the RTI problem will be written

$$\mathbf{y} = \mathbf{W}\mathbf{x} + \mathbf{n} \tag{2.8}$$

There are many variations of weight matrices, $\mathbf{W}$, that relate the RSS to the image.

2.1.2.2 Weight Matrix

Martin, et al. [22] identified various weight models, and posited that each weight model can be expressed as

$$\mathbf{W} = \mathbf{S} \odot \mathbf{\Omega} \tag{2.9}$$

where $\mathbf{S}$ is a binary matrix identifying which links affect which pixels, $\mathbf{W}$ is a magnitude matrix that further defines how links affect pixels, and $\odot$ is the element-wise product of the two matrices. The three common selection matrices identified in [22] for a link m and pixel n are

$$S_{m,n}^{Ellipse} = \begin{cases} 1, & \text{if } d_{1,m,n} + d_{2,m,n} < d_m + \lambda \\ 0, & \text{otherwise} \end{cases} \tag{2.10}$$

$$S_{m,n}^{Line} = \begin{cases} 1, & \text{if link } m \text{ intersects pixel } n \\ 0, & \text{otherwise} \end{cases} \tag{2.11}$$

$$S_{m,n}^{All} = 1 \tag{2.12}$$

where d_m is the total link length of link m, $d_{1,m,n}$ is the distance from the center of pixel n to one endpoint of link m, $d_{2,m,n}$ is the distance from the center of pixel n to the other endpoint of link m, and λ is a parameter that can be selected to determine the length of the major axis of the ellipse that exceeds the length of link m, expressed as $\lambda_{m,n} = d_{1,m,n} + d_{2,m,n} - d_m$. The $\mathbf{S}^{Ellipse}$ selection matrix is the most frequently used in literature, found in a variety of RTI publications, including [6, 10, 11, 14, 15, 19, 29, 31, 33–35] among many others. This is likely due to the fact that an elliptical pattern around the transmitter and receiver corresponds to the

electromagnetic Fresnel ellipsoid that is related to the diffraction patterns around an obstruction, explored in literature while investigating robust physical models for RTI as seen in [27, 28, 36].

Network Shadowing (NeSh) The NeSh model, originally developed by Patwari in [23] and [26] and formally applied to an RTI system in [6] inherently uses the $\mathbf{S}^{Ellipse}$ selection matrix and applies a magnitude for a link m and pixel n [22]

$$\Omega_{m,n}^{NeSh} = 1/\sqrt{d_m} \tag{2.13}$$

Applying (2.13) and (2.10) to (2.9) results in a weight matrix $\mathbf{W}^{NeSh}$ such that for a link m and pixel n

$$W_{m,n}^{NeSh} = \begin{cases} 1/\sqrt{d_m}, & \text{if } d_{1,m,n} + d_{2,m,n} < d_m + \lambda \\ 0, & \text{otherwise} \end{cases}. \tag{2.14}$$

The NeSh weighting model can be seen in use in [6,11,21,36]. However, given that the ellipse selection matrix is implicitly used in the NeSh model, many other publications have models that behave similarly.

Line The line model is a more simplistic approach that was used in [37] specifically for its simplicity, as well as its proven use for some medical imaging techniques. It uses the $\mathbf{S}^{Line}$ selection matrix and a scale factor of $\Omega_{m,n}^{Line} = L_{m,n}$ resulting in a weight matrix [21, 37]

$$W_{m,n}^{Line} = \begin{cases} L_{m,n}, & \text{if link } m \text{ intersects pixel } n \\ 0, & \text{otherwise} \end{cases} \tag{2.15}$$

where $L_{m,n}$ is the length of the portion of the link-line m that passes through pixel n. This maps the drop in RSS directly to the amount of the link-line being obstructed.

NeSh-Line The NeSh-Line model is an approach that is not found often in the literature. Used primarily in [38] and [39], it uses the $\mathbf{S}^{Line}$ selection matrix and a magnitude matrix that is a combination of the NeSh and line models, such that [22]

$$W_{m,n}^{NeSh-Line} = \begin{cases} L_{m,n}/\sqrt{d_m}, & \text{if link } m \text{ intersects pixel } n \\ 0, & \text{otherwise} \end{cases}. \tag{2.16}$$

The authors in [38] and [39] directly borrow the $1/\sqrt{d_m}$ scaling of the NeSh model from [23] and apply it to the line model, which directly relates the RSS to the length of the link-line being obstructed. This model incorporates both the conclusion that the information provided by a link is inversely proportional to its total length, and that the length of the link being obstructed is directly proportional to the drop in RSS. While the elliptical selection matrix is implicit to the NeSh model, the NeSh-Line model essentially assumes an ellipse so narrow it can be approximated as a line.

Exponential The exponential model relates RSS to the total link length, the distance between the transmitter and the target, and the distance between the receiver and the target [20]. This model lends itself to what Li in [20] calls a "pixel-free" measurement model, as the RSS can be modeled using only the position of the target, rather than a vector of pixel intensity values. To relate this to a pixel-by-pixel image, the vector of pixel intensity values can be used instead, with obstructed pixels taking a value greater than zero and unobstructed pixels taking a value of zero. Rather than using the λ_k^i from [20] which depends only on transmitter, receiver, and target position, $\lambda_{m,n}$ as defined above can be used to relate the position of the

transmitter, receiver, and obstructed pixel (effectively target location). The resultant weight matrix is [20, 22]

$$W_{m,n}^{Exp} = \begin{cases} \exp(-\lambda_{m,n}/(2\sigma_w)), & \text{if } \lambda_{m,n} \geq 0 \\ 0, & \text{otherwise} \end{cases}. \tag{2.17}$$

This model essentially uses the $\mathbf{S}^{All}$ selection matrix, with zeroes where nodes have "links" with themselves. This model, scaled by $1/\sqrt{d_m}$ is also used in [16].

Inverse Area Hamilton [36] proposes a unique model that uses the inverse of the area of confocal ellipses. A minimum and maximum semi-minor axis length (controlling the ellipse width) is chosen to bound the extent of the ellipses, with the maximum being chosen based on the width of the first Fresnel ellipse to more accurately model effects due to diffracted paths [36]. A variation of the specific model [36] used can be seen in use in [11, 14, 22], which use the excess path length to create the confocal ellises. Taking the area of an ellipse to be [22]

$$A(d_m, \lambda) = \frac{\pi}{4}(d_m + \lambda)\sqrt{2d_m\lambda + \lambda^2} \tag{2.18}$$

and relating it to the existing framework discussed thus far results in the following magnitudes [22]

$$\Omega_{m,n}^{InvArea} = \begin{cases} \frac{1}{A(d_m,\lambda_{min})}, & \text{if } \lambda_{m,n} < \lambda_{min} \\ \frac{1}{A(d_m,\lambda_{m,n})}, & \text{if } \lambda_{m,n} \geq \lambda_{min} \end{cases}. \tag{2.19}$$

This magnitude matrix is then applied using the ellipse selection matrix, resulting in the following weight matrix elements for link m and pixel n

$$W_{m,n}^{InvArea} = \begin{cases} \Omega_{m,n}^{InvArea}, & \text{if } d_{1,m,n} + d_{2,m,n} < d_m + \lambda_{m,n} \\ 0, & \text{otherwise} \end{cases}. \tag{2.20}$$

2.1.2.3 Noise Model

The noise element from (2.8), $\mathbf{n}$, has been explored in much of the existing literature. Experimental data and subsequent statistical analysis led many researchers to model the noise as additive white Gaussian noise (AWGN), which is explicitly stated in [18, 20, 22, 27, 36, 38, 39] as well as others. Wilson and Patwari explore a Gaussian mixture model (GMM) in [6], where the noise is a mixture of two Gaussian distributions, a low-variance Gaussian and high-variance Gaussian. This was based on work performed on indoor wireless communications channels performed in [40] that found a two-state Markov model with a fading and non-fading state modeled wireless channels more accurately; however, Roberts [40] used a Rician distribution rather than Gaussian. The general consensus in literature appears to be that an AWGN model adequately represents the noise in an RTI system, with even the results comparing experimental measurements with both modeled AWGN and GMM noise in [6] showing reasonably close agreement.

2.1.3 Image Estimation

With models established for $\mathbf{W}$ and $\mathbf{n}$ from (2.8), the problem can be solved for $\mathbf{x}$. When modeling a true image, attenuated pixels are selected and filled in based on the extent of the obstruction. For RTI the main goal is to localize humans in most contexts [6]. To model a human inside of an RTI grid, Wilson and Patwari assume the

human body to be a uniformly attenuating cylinder of radius R_H [6]. The position of the uniformly attenuating cylinder model can then be used to construct the truth image using [6]

$$x_{cj} = \begin{cases} 1, & \text{if } ||x_j - c_H|| < R_H \\ 0, & \text{otherwise} \end{cases} \tag{2.21}$$

where x_{cj} is the center of pixel j, x_j is pixel j and c_H is the location of the human obstruction. The approximate size of a human used by [6] is $R_H = 1.3$ ft.

The above provides mathematical representations for all parts of (2.8). The image can then be solved for in the least-squared error sense [6]

$$\hat{\mathbf{x}}_{LS} = \underset{\mathbf{x}}{\operatorname{argmin}} ||\mathbf{W}\mathbf{x} - \mathbf{y}||_2^2. \tag{2.22}$$

To obtain the least-squares solution, the gradient of (2.22) is set to zero, yielding [6]

$$\hat{\mathbf{x}}_{LS} = (\mathbf{W}^T\mathbf{W})^{-1}\mathbf{W}^T\mathbf{y}. \tag{2.23}$$

The inversion of $\mathbf{W}^T\mathbf{W}$ in (2.23) requires $\mathbf{W}$ to be full rank in order to work, which is not true for RTI systems [6]. This was alluded to above as the ill-posed inverse problem that requires some form of regularization to prevent small values from approaching infinity upon inversion. The process of regularization adds information to allow inversion without issue [6].

2.1.3.1 Regularization

Various methods of regularization exist that provide a solution to the ill-posed inverse problem of RTI systems [2, 33]. The challenge for making RTI image reconstruction possible via the least-squares method becomes a balance between how well a given method works versus how computationally expensive it is. This is mostly due

to the context of using resource-constrained devices for RTI for a highly deployable system and the importance of having near-real-time imaging.

Linear Back Projection Linear back projection is one of the simplest methods for reconstructing an RTI image [2, 33]. Rather than taking an inverse, $\mathbf{W}^T$ is used to map the RSS to pixel values such that [2, 33]

$$\hat{\mathbf{x}} = \mathbf{W}^T\mathbf{y}. \tag{2.24}$$

While providing an easy-to-implement solution, [33] found linear back projection fails to account for the effect of noise, making the resultant image sub-par. However, [33] found that linear back projection can successfully localize a single, stationary human inside of a WSN.

Tikhonov Regularization Tikhonov regularization is a common method found in much of the literature. It is used as a regularization technique for reconstruction or comparison purposes in [2, 3, 6, 10, 15, 17, 19, 21, 22, 25, 29, 32, 33, 37, 41]. Tikhonov regularization adds a term to the objective function such that [6]

$$f(x) = \frac{1}{2}||\mathbf{Wx} - \mathbf{y}||^2 + \frac{\alpha}{2}||\mathbf{Qx}||^2 \tag{2.25}$$

where $\mathbf{Q}$ is the Tikhonov matrix and α is a weighting parameter that determines how much the regularization drives the solution. Wilson and Patwari use a difference matrix for $\mathbf{Q}$ in [6], which approximates the first derivative. The image is two-dimensional, requiring the derivative be taken along the x and y directions, represented by the difference matrices $\mathbf{D}_x$ and $\mathbf{D}_y$, respectively [6].

Incorporating the difference matrices into (2.25) results in

$$f(x) = \frac{1}{2}||\mathbf{W}\mathbf{x} - \mathbf{y}||^2 + \frac{\alpha}{2}\left(||\mathbf{D}_x\mathbf{x}||^2 + ||\mathbf{D}_y\mathbf{x}||^2\right) \tag{2.26}$$

Once regularized, the problem can then be solved in the least-squares sense as in (2.23) where the gradient is taken, set to zero, and the estimate $\hat{\mathbf{x}}_{LS}$ becomes [6]

$$\hat{\mathbf{x}}_{LS} = \left(\mathbf{W}^T\mathbf{W} + \alpha\left(\mathbf{D}_x^T\mathbf{D}_x + \mathbf{D}_y^T\mathbf{D}_y\right)\right)^{-1}\mathbf{W}^T\mathbf{y} \tag{2.27}$$

which can conveniently be expressed as a linear transformation with transformation matrix Π where

$$\Pi = \left(\mathbf{W}^T\mathbf{W} + \alpha\left(\mathbf{D}_x^T\mathbf{D}_x + \mathbf{D}_y^T\mathbf{D}_y\right)\right)^{-1}\mathbf{W}^T \tag{2.28}$$

$$\hat{\mathbf{x}}_{LS} = \Pi\mathbf{y}. \tag{2.29}$$

The transformation matrix, Π, does not depend on measurements, allowing it to be precalculated and applied to measurement vectors as they are reported by the WSN [6]. These attributes make Tikhonov regularization a good balance between computational complexity and the quality of the solution.

Covariance Weighted Least Squares In the weighted least squares using covariance approach to regularization, an *a priori* covariance matrix is used [11]. This approach is another popular and effective approach in the literature, found at use in [11, 14, 16, 26, 42]. This approach also expresses the estimate as a linear transformation of the RSS measurements as in (2.29), where Π is [11]

$$\Pi = (\mathbf{W}^T\mathbf{W} + \mathbf{C}_x^{-1}\sigma_N^2)^{-1}\mathbf{W}^T \tag{2.30}$$

where σ_N^2 is the weighting parameter for regularization and $\mathbf{C}_x$ is the a priori covariance matrix. The elements of $\mathbf{C}_x$ are often expressed by [11]

$$[\mathbf{C}_x]_{i,j} = \sigma_x^2 \exp\left(\frac{-d_{i,j}}{\delta_c}\right) \tag{2.31}$$

where σ_x^2 is the variance of the pixels and $d_{i,j}$ is the distance between the center of pixel i and pixel j. The weighted least squares method using the *a priori* covariance, much like Tikhonov regularization, is also a good balance between computational complexity and the quality of the solution for a real time RTI system.

Projected Landweber Iteration An example of a more computationally intensive method that is not particularly useful for real-time imaging in an RTI system is presented in [33] - a method called projected Landweber iteration. It begins by taking the gradient of the objective function $f(x)$ where [33]

$$f(\mathbf{x}) = \frac{1}{2}||\mathbf{W}\mathbf{x} - \mathbf{y}||^2 = \frac{1}{2}(\mathbf{y} - \mathbf{W}\mathbf{x})^T(\mathbf{y} - \mathbf{W}\mathbf{x}) \tag{2.32}$$

$$\nabla f(\mathbf{x}) = \mathbf{W}^T(\mathbf{W}\mathbf{x} - \mathbf{y}) \tag{2.33}$$

The projected Landweber iteration method then uses a projection operator, $P[\cdot]$ whose argument is a steepest-descent algorithm to calculate the next step such that [33]

$$\hat{\mathbf{x}}_{k+1} = P\left[\hat{\mathbf{x}}_k - \mu\mathbf{W}^T(\mathbf{W}\hat{\mathbf{x}}_k - \mathbf{y})\right] \tag{2.34}$$

and the projection operator, operating element-by-element, is defined as

$$P[f(\mathbf{x})] = \begin{cases} 0 & \text{if } f(\mathbf{x}) < 0 \\ f(\mathbf{x}) & \text{if } 0 \leq f(\mathbf{x}) \leq 1 \\ 1 & \text{otherwise} \end{cases} \cdot \tag{2.35}$$

Similarly to the linear back projection method, this method does not require taking the inverse, and so avoids the issue of small values in $\mathbf{W}$ causing issues; however, because it is an iterative method, [33] found that it can take many iterations to arrive at a desirable result. Additionally, [33] found that too many iterations can also cause degradation of the image, and without a formula to calculate the optimal number of iterations, it must be found empirically. These attributes make the projected Landweber iteration method a much less efficient process that does not fit the context of a rapidly deployable, real-time imaging system, which is typically the most common context for RTI systems.

2.2 Position Tracking

One goal seen throughout literature is to track a moving target within the RTI network. This can be achieved in a variety of ways with a range of advantages and results. A natural progression from the imaging results in RTI is using the resultant image to localize targets, an approach seen in [4, 11, 23, 37] and others. Another method explored frequently is using a state-space approach where the target's state is tracked. Depending on the specific implementation, the state space may be just position or both position and velocity. Some of the Bayesian approaches to target tracking using an RTI WSN seen in [16] use a purely state-space approach to track the target. A few of the approaches used are detailed below.

2.2.1 Maximum A Posteriori

The maximum a posteriori (MAP) estimator is one of the most straightforward approaches that can be used to localize the target. It is used in a wide array of the literature, and is particularly favored in [6]. It uses the image calculated in (2.23), which is a vector of pixel intensities. Taking each element of $\hat{\mathbf{x}}_{LS}$ to represent the intensity of pixel j, denoted by $\hat{x}_j$, the MAP estimate for the target location can be defined as [43]

$$\hat{p}_{MAP} = \underset{j}{\operatorname{argmax}}\ p\left(\hat{x}_j|\mathbf{y}\right). \tag{2.36}$$

Taking into account the cylindrical human model in (2.21), with a small radius, and the white Gaussian noise model as described in section 2.1.2.3, $\hat{p}_{MAP}$ reduces similarly to a direct-current signal in the presence of white Gaussian noise to be [43]

$$\hat{p}_{MAP} = \underset{j}{\operatorname{argmax}}\ \hat{x}_j. \tag{2.37}$$

The index for the highest intensity pixel is then mapped to a coordinate using the same mapping that generates the image from the pixel vector.

2.2.2 K-Means Clustering

Another method to localize targets that was found to be of particular use with multiple targets present is K-means clustering. This approach was applied in [4] to localize multiple targets. It is somewhat related to the MAP approach, but rather than picking the location of the maximum pixel intensity, a threshold is chosen for the pixel intensity such that only pixels at or above the threshold intensity value are used in the K-means algorithm [4]. The pixels are then grouped into K clusters, and

the following cost function is minimized to find an optimal cluster centroid [4]

$$J = \sum_{i=1}^{K} \sum_{x_j \in S_i} ||x_j - C_i||^2 \tag{2.38}$$

where S_i is the set of pixels in cluster i, x_j is the jth pixel in the set of clustered pixels, and C_i is the centroid of cluster i. The centroid is taken to be the target location, and provides a sub-pixel coordinate versus MAP which will only yield coordinates for pixel centers.

2.2.3 Particle Filtering

Another tracking method that is more computationally intensive and uses Bayesian methods to track position and velocity in a state space is particle filtering. Kaltiokallio implemented this approach in [16]. In general, particle filtering was difficult to implement due to the "degeneracy problem" that results in much of the data used having a zero weight [44]. This led to the use of a "sequential importance resampling" algorithm which resamples particles when needed, typically after some predefined number of steps [44]. The sequential importance resampling approach was used in [16], which allows approximation of the posterior probability density function (PDF) as [44]

$$p(\mathbf{x}_k|\mathbf{z}_{1:k}) \approx \sum_{i=1}^{M} w_k^i \delta(\mathbf{x}_k - \mathbf{x}_k^i) \tag{2.39}$$

where $\mathbf{z}_{1:k}$ is the collection of RSS measurements on all links, containing measurement vectors from time step 1 through time step k; M is the number of particles; w_k^i is the weight for particle i; $\mathbf{x}_k^i$ is the state of particle i; $\delta(\cdot)$ is the dirac delta function; and $\mathbf{x}_k$ is the actual state. Using this, the prediction and update stages for the particle

filter then become [16]

$$\mathbf{x}_k^i \sim p(\mathbf{x}_k|\mathbf{x}_k^i) \tag{2.40}$$

$$w_k^i = \prod_{l=1}^{L} \exp\left(-\frac{(z_l(k) - h_l(\mathbf{x}_k^i))^2}{2\sigma_r^2}\right) \tag{2.41}$$

where $z_l(k)$ is the RSS of link l at time k corresponding to the , L is the total number of links, σ_r^2 is the measurement noise variance, and

$$h_l(\mathbf{x}_k) \triangleq \phi e^{-\triangle_l(k)/\lambda_{filt}} \tag{2.42}$$

$$\triangle_l(k) = ||\mathbf{p}_i - \mathbf{p}_k|| + ||\mathbf{p}_j - \mathbf{p}_k|| - ||\mathbf{p}_i - \mathbf{p}_j|| \tag{2.43}$$

is the measurement model used in [16] where λ_{filt} is a tunable parameter to control the rate of decay and ϕ is the maximum change in RSS when a link line is crossed. All $\mathbf{p}$ vectors are position vectors such that $\mathbf{p} = [p_x \quad p_y]^T$ with $\mathbf{p}_i$ denoting the position of the transmitter, $\mathbf{p}_j$ denoting the position of the receiver, and $\mathbf{p}_k$ denoting the position of the target which is contained in the state vector $\mathbf{x}_k$ [16]. The model in (2.42) is an exponential decay model that uses an ellipse defined by (2.43) where the transmitter and receiver are the foci of the ellipse. This is similar to the weight models that use an elliptical selection matrix as defined in (2.10); however, this model results in a continuous ellipse that will provide a decaying RSS measurement as the target moves further away from the link line, whereas the elliptical selection matrix defines a fixed ellipse outside of which the RSS goes to zero.

2.2.4 Kalman Filtering

A Bayesian filtering method that is widely popular in position tracking is using a Kalman filter, which assumes a linear Gaussian dynamic and measurement model [44]. Kaltiokallio [16] applied this to RTI, calculating an image from the RSS

measurements, then mapping that image to a kinematic state.

State and Measurement Models The dynamic state and measurement models are expressed as [16, 44]

$$\mathbf{x}_k = \mathbf{F}_k \mathbf{x}_{k-1} + \mathbf{q}_{k-1} \tag{2.44}$$

$$\mathbf{z}_k = \mathbf{H}_k \mathbf{x}_k + \mathbf{r}_k, \tag{2.45}$$

respectively; where $\mathbf{x}_k$ is the state vector of the target containing position and velocity, $\mathbf{F}_k$ is the dynamic model, $\mathbf{q}_{k-1} \sim \mathcal{N}(\mathbf{0},\ \mathbf{Q}_{k-1})$ is the process noise, $\mathbf{H}_k$ is the measurement model matrix that maps the state vector $\mathbf{x}_k$ to the measurement vector, and $\mathbf{r}_k$ is the measurement noise. The Kalman filter assumes a Gaussian prior distribution on the initial state vector $\mathbf{x}_0 \sim \mathcal{N}(\mathbf{m}_0,\ \mathbf{P}_0)$, whose statistics are then utilized for subsequent prediction and update stages in the filtering process [44].

Prediction and Update The filter's prediction step is then [16, 44]

$$\mathbf{m}_k^- = \mathbf{F}_{k-1} \mathbf{m}_{k-1} \tag{2.46}$$

$$\mathbf{P}_k^- = \mathbf{F}_{k-1} \mathbf{P}_{k-1} \mathbf{F}_{k-1}^T + \mathbf{Q}_{k-1} \tag{2.47}$$

where

- $\mathbf{m}_k^-$ is the predicted filter mean/estimated state
- $\mathbf{F}_{k-1}$ is the dynamic model for the previous time step
- $\mathbf{m}_{k-1}$ is the filter mean/estimated state for the previous time step
- $\mathbf{P}_k^-$ is the predicted filter covariance
- $\mathbf{P}_{k-1}$ is the filter covariance for the last time step

- $\mathbf{Q}_{k-1}$ is the process noise for the previous time step.

After predicting the statistics for the next state using an estimated prior distribution for the state without using any new measurement, the filter then updates its gain and makes a final state estimate based on the predicted state and measurement data. This step is expressed by [16, 44]

$$\mathbf{S}_k = \mathbf{H}_k \mathbf{P}_k^- \mathbf{H}_k^T + \mathbf{R}_k \tag{2.48}$$

$$\mathbf{K}_k = \mathbf{P}_k^- \mathbf{H}_k^T \mathbf{S}_k^{-1} \tag{2.49}$$

$$\mathbf{m}_k = \mathbf{m}_k^- + \mathbf{K}_k \left(\mathbf{z}_k - \mathbf{H}_k \mathbf{m}_k^- \right) \tag{2.50}$$

$$\mathbf{P}_k = \mathbf{P}_k^- - \mathbf{K}_k \mathbf{S}_k \mathbf{K}_k^T \tag{2.51}$$

where

- $\mathbf{S}_k$ is referred to as the innovation covariance of the filter
- $\mathbf{K}_k$ is the Kalman gain of the filter
- $\mathbf{m}_k$ is the calculated mean of the Kalman filter, also the estimated state
- $\mathbf{P}_k$ is the calculated filter covariance.

The prediction and update stages are initialized using $\mathbf{m}_0$ and $\mathbf{P}_0$ as the first available prior information [44].

Extended Kalman Filter The extended Kalman Filter (EKF) is an extension of Kalman filtering to non-linear filtering [44]. Assuming the dynamic and measurement model noises are additive, the state and measurement models seen in

(2.44) and (2.45) are alternatively expressed as [44]

$$\mathbf{x}_k = \mathbf{f}(\mathbf{x}_{k-1}) + \mathbf{q}_{k-1} \tag{2.52}$$

$$\mathbf{z}_k = \mathbf{h}(\mathbf{x}_k) + \mathbf{r}_k, \tag{2.53}$$

where $\mathbf{f}(\cdot)$ is the dynamic model function and $\mathbf{h}(\cdot)$ is the measurement model function, both of which are not necessarily linear. Given the non-linearity, the use of an EKF approximates the prior distribution as Gaussian such that $p(\mathbf{x}_k|\mathbf{y}_{1:k}) \simeq \mathcal{N}(\mathbf{x}_k|\mathbf{m}_k, \mathbf{P}_k)$, by using Taylor series approximations to the non-linearities [44]. This approximation results in a linearization of the processes local to the optimal solution, and is dependent on a process that is not highly non-linear and has differentiable measurement and dynamic models [44]. The prediction and update stages are then expressed as [44]

$$\mathbf{m}_k^- = \mathbf{f}(\mathbf{m}_{k-1}) \tag{2.54}$$

$$\mathbf{P}_k^- = \mathbf{F}_\mathbf{x}(\mathbf{m}_{k-1})\mathbf{P}_{k-1}{\mathbf{F}_\mathbf{x}}^T(\mathbf{m}_{k-1}) + \mathbf{Q}_{k-1} \tag{2.55}$$

$$\mathbf{S}_k = \mathbf{H}_\mathbf{x}(\mathbf{m}_k^-)\mathbf{P}_k^-{\mathbf{H}_\mathbf{x}}^T(\mathbf{m}_k^-) + \mathbf{R}_k \tag{2.56}$$

$$\mathbf{K}_k = \mathbf{P}_k^-{\mathbf{H}_\mathbf{x}}^T(\mathbf{m}_k^-)\mathbf{S}_k^{-1} \tag{2.57}$$

$$\mathbf{m}_k = \mathbf{m}_k^- + \mathbf{K}_k\left(\mathbf{z}_k - \mathbf{h}(\mathbf{m}_k^-)\right) \tag{2.58}$$

$$\mathbf{P}_k = \mathbf{P}_k^- - \mathbf{K}_k\mathbf{S}_k\mathbf{K}_k^T \tag{2.59}$$

where $\mathbf{F}_\mathbf{x}$ is the Jacobian matrix of the dynamic model function and similarly, $\mathbf{H}_\mathbf{x}$ is the Jacobian matrix of the measurement model function.

2.2.4.1 Application in RTI

Kalman Filter In [16], a standard Kalman filter and extended Kalman filter were applied to an RTI system. A state-space model was used such that the state of the target was represented by [16]

$$\mathbf{x}_k = [p_x(k) \quad v_x(k) \quad p_y(k) \quad v_y(k)]^T \tag{2.60}$$

where p_x and p_y are the x and y coordinates of the target, respectively, and v_x and v_y are the velocity of the target in the x and y directions, respectively. This specific notation can be confusing as the estimated image in RTI is denoted as $\hat{\mathbf{x}}$. To discriminate more easily between the state vector and estimated image vector, the estimated image will be denoted using $\hat{\mathbf{x}}_{img}$ in this section.

In the Kalman filtering approach implemented in [16], $\mathbf{F}$ and $\mathbf{H}$ do not change with each time step, as $\mathbf{H}$ is a straightforward mapping from the four-element vector $\mathbf{x}_k$ to a two-element vector with just the position, which will be denoted as $\mathbf{p}_k$ (unrelated to the filter covariance matrix $\mathbf{P}_k$). Additionally, the measurement model in (2.45) is based on the MAP estimation of the target location from the RTI image, which essentially dissociates the actual RSS measurements from the Kalman filter "measurement" model [16]. The initial state estimate is taken from (2.37) and the measurement model in (2.45) becomes [16]

$$\mathbf{p}_k = \mathbf{H}\mathbf{x}_k + \mathbf{n}_k^{img}, \text{where} \tag{2.61}$$

$$\mathbf{H} = \begin{bmatrix} 1 & 0 & 0 & 0 \\ 0 & 0 & 1 & 0 \end{bmatrix} \tag{2.62}$$

which models a state based on the statistics of the image, where $\mathbf{n}_k^{img}$ is the noise associated with the estimated image in (2.23) because the "measurement" in this case

is the coordinate pair obtained from the MAP estimate. Thus, the Kalman Filter state update in (2.50) becomes $\mathbf{m}_k = \mathbf{m}_k^- + \mathbf{K}_k \left(\mathbf{p}_k - \mathbf{H}_k \mathbf{m}_k^-\right)$. This is notable because the Kalman filter in this particular application does not relate RSS measurements directly to the state space, instead the RSS is used to produce an initial position estimate in the state space and the Kalman filter is subsequently used to track the state [16]. A similar implementation of this Kalman filter approach for RTI is also found in [24,42].

Extended Kalman Filter The EKF as implemented in [16] relates the RSS measurements directly to the state space. The dynamic model $\mathbf{F}$ remains the same linear dynamic model used for the Kalman filter making the prediction stage the same seen in (2.46), but (2.42) is used as the non-linear measurement model where $h_l(\mathbf{x}_k) \triangleq \phi e^{-\triangle_l(k)/\lambda_{filt}}$ such that the RSS measurement model, (2.53), is given by $\mathbf{y}_k = \mathbf{h}(\mathbf{x}_k) + \mathbf{n}_k$. With the non-linearity in the measurement model, the Jacobian matrix $\mathbf{H_x}$ is used in the filter prediction and update stages, where the Jacobian for a link l is given by [16] as

$$\mathcal{H}_l(\mathbf{x}_k) = \begin{bmatrix} \frac{\delta h_l(\mathbf{x}_k)}{\delta p_x} & 0 & \frac{\delta h_l(\mathbf{x}_k)}{\delta p_y} & 0 \end{bmatrix}^T, \text{where} \tag{2.63}$$

$$\begin{bmatrix} \frac{\delta h_l(\mathbf{x}_k)}{\delta p_x} & \frac{\delta h_l(\mathbf{x}_k)}{\delta p_y} \end{bmatrix}^T = \frac{h_l(\mathbf{x}_k)}{\lambda_{filt}} \left(\frac{\mathbf{p}_i - \mathbf{p}_k}{||\mathbf{p}_i - \mathbf{p}_k||} + \frac{\mathbf{p}_j - \mathbf{p}_k}{||\mathbf{p}_j - \mathbf{p}_k||} \right) \tag{2.64}$$

and the Jacobian matrix for L total links is then

$$\mathbf{H_x} = \begin{bmatrix} \mathcal{H}_1(\mathbf{x}_k)^T & \dots & \mathcal{H}_L(\mathbf{x}_k)^T \end{bmatrix}^T. \tag{2.65}$$

This is then used in the update stages of the EKF in (2.56) - (2.59).

While considered a non-linear filtering method, the extended Kalman filter relies on the ability to differentiate the non-linear process it is filtering in order for linearization to occur [44]. This is why the Jacobian of the measurement model is used for the

update stages of the extended Kalman filter, producing a linearized approximation of the non-linear measurement.

III. Methodology

3.1 Modeling and Simulation

3.1.1 Processing Methods

The current Air Force Institute of Technology (AFIT) radio tomographic imaging (RTI) system processes received signal strength (RSS) measurements using the same methods developed in [6]. That method looks at the total number of *unique* links in the wireless sensor network (WSN). The immediate ramifications of viewing each two-way radio frequency (RF) link as a single, unique link are that two RSS measurements are obtained for a single link at two different time instances. Using the typical method of creating the image, the base station will wait until all nodes have reported to update the image, meaning it must take pairs of RSS measurements for each unique link and turn them into a single measurement to update the image. This results in time-averaged measurements that reflect on average what happened on a given link between the time of the first and second RSS measurements. Depending on the dynamics of the scene, this can be problematic. In addition, [16] found this method to be problematic when implementing certain tracking algorithms.

3.1.1.1 Sequential Processing

Tracking position with an extended Kalman Filter (EKF) is more readily facilitated when using measurements that are taken in the same time instant. The RTI graphical user interface (GUI) post processes RSS measurements taken from all transceivers once they become available at the base station. Another way to process the RSS measurements is to break the measurement matrix into vectors representing RSS measurements taken in the same time instant. An important distinction should be made such that the time that a measurement is taken (the RSS on a given link)

is not the same time it is reported. Each report in an RTI WSN contains RSS measurements taken at different times. The measurement matrix $\mathbf{Z}$ is constructed such that the element $z_{i,j}$ is the RSS from transmitter j to receiver i. Taking a five-node RTI system as an example:

$$\mathbf{Z} = \begin{bmatrix} 0 & z_{1,2} & z_{1,3} & z_{1,4} & z_{1,5} \\ z_{2,1} & 0 & z_{2,3} & z_{2,4} & z_{2,5} \\ z_{3,1} & z_{3,2} & 0 & z_{3,4} & z_{3,5} \\ z_{4,1} & z_{4,2} & z_{4,3} & 0 & z_{4,5} \\ z_{5,1} & z_{5,2} & z_{5,3} & z_{5,4} & 0 \end{bmatrix}. \tag{3.1}$$

This approach is detailed in [16] and is achieved using the communication protocol as detailed in [11]. The measurement matrix as constructed in (3.1) assumes that one round of data from the entire WSN has already been collected. Figure 2 shows how the measurement matrix is constructed. For each communication round, a matrix with an upper triangle and lower triangle is constructed. The upper triangle consists of measurements that were taken the previous round and are being reported now, and the lower triangle consists of measurements taken from the current round.

Figure 3 shows what each transmitter would report on the initial round of communication. The most current measurements would be built in the lower triangle of the measurement matrix. At time k, there are enough measurements in the matrix to extract time-synchronous RSS readings. The first column of $\mathbf{Z}$ all occurred at time $k - 4$.

Continuing the measurement cycle into the second round as shown in figure 4 and stacking the complete measurement matrices, the result in figure 2 is obtained. After the first complete round, each subsequent time step enables a new time-synchronous measurement vector to be used in the tracking solution. This results in an overall

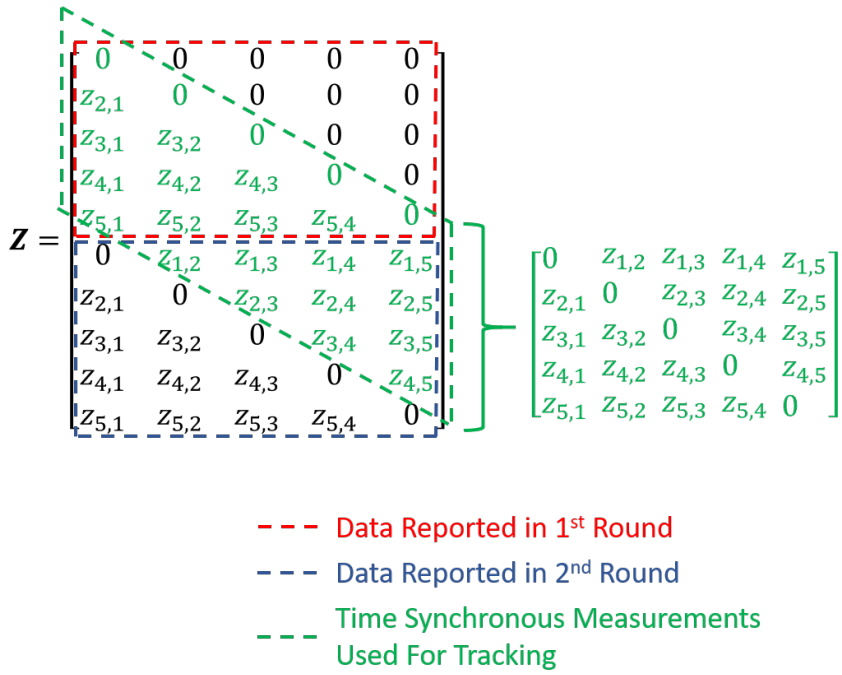

Figure 2: Measurement matrix with time synchronous columns.

delay in the tracking solution of $N\tau_{tx}$ where N is the total number of nodes in the WSN and τ_{tx} is the time it takes for each individual node to report.

An alternative sequential processing method this thesis explores is utilizing each report as the base station receives it. This means each time a node transmits, a row of $\mathbf{Z}$ is obtained and utilized to update any imaging and position tracking methods. It is important to note that when a node reports its collected RSS measurements, the other nodes use that transmission to calculate the RSS on links made with the reporting node. For example, referring to (3.2), when node 1 reports RSS measurements at time $k = 6$, the first row in (3.2) is obtained. This same report from node 1 isalso used by nodes 2, 3, 4, and 5 to obtain the RSS measurements in the first column of (3.2). The report-by-report sequential processing method excludes the use of the EKF as implemented in [16]. Associating times with the RSS measurements in the five-node example above, where $z(k)$ is an RSS measurement at time k, the first full

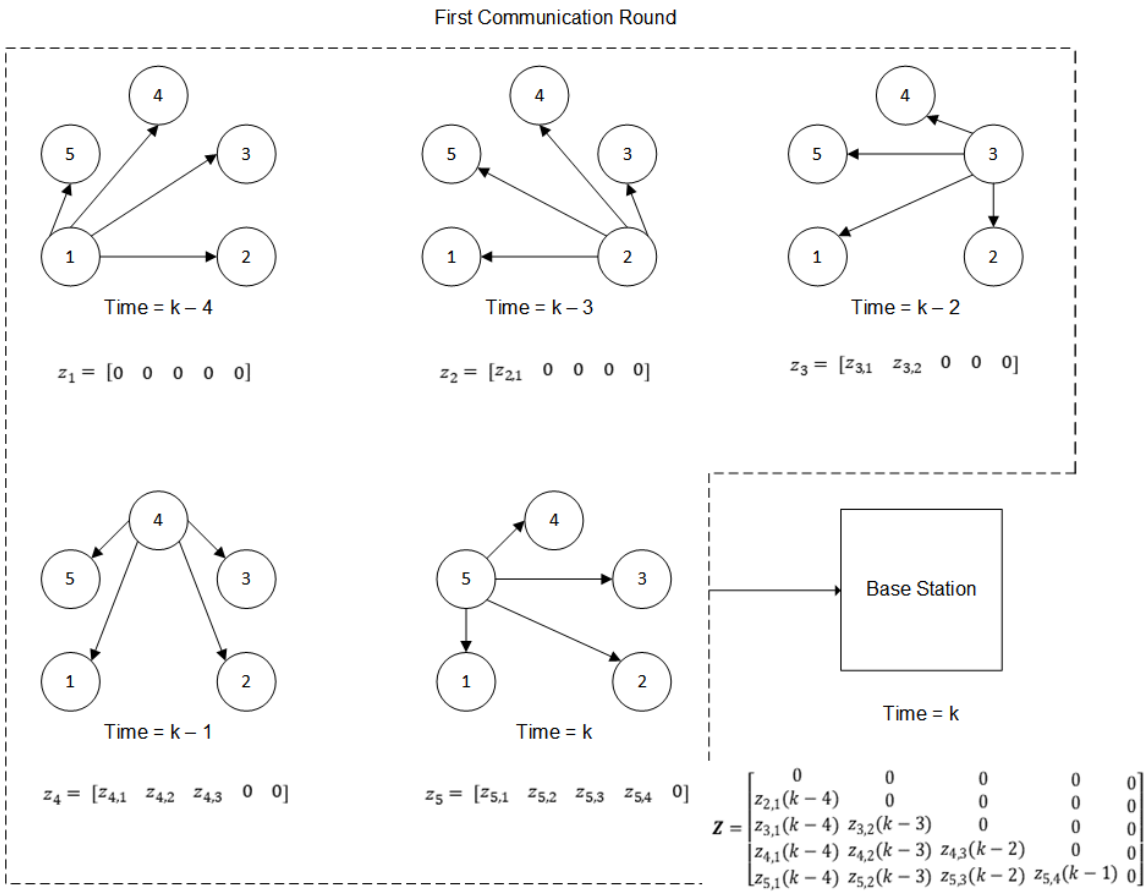

Figure 3: Example reports by transmitter for the first round of communication.

measurement matrix starting with a report from node 1 at time $k = 1$ would be

$$\mathbf{Z} = \begin{bmatrix} 0 & z_{1,2}(2) & z_{1,3}(3) & z_{1,4}(4) & z_{1,5}(5) \\ z_{2,1}(6) & 0 & z_{2,3}(3) & z_{2,4}(4) & z_{2,5}(5) \\ z_{3,1}(6) & z_{3,2}(7) & 0 & z_{3,4}(4) & z_{3,5}(5) \\ z_{4,1}(6) & z_{4,2}(7) & z_{4,3}(8) & 0 & z_{4,5}(5) \\ z_{5,1}(6) & z_{5,2}(7) & z_{5,3}(8) & z_{5,4}(9) & 0 \end{bmatrix} \tag{3.2}$$

This method uses new information as soon as it is available at the base station, however the challenge becomes the implementation of a smoothing filter in real time, as each report contains recent and old measurements.

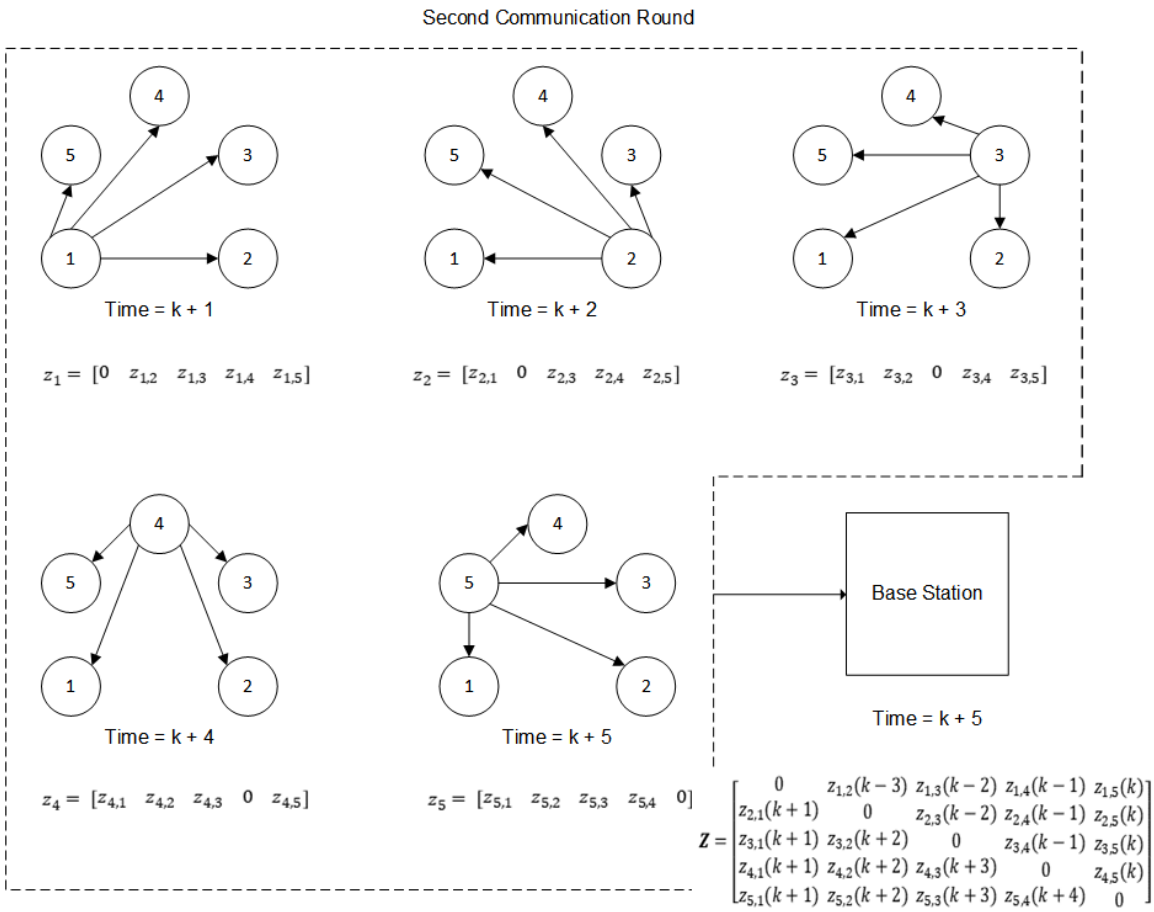

Figure 4: Example reports by transmitter for the second round of communication.

3.1.1.2 Information, Currency, History, and Utility

The different time steps at which each RSS measurement is taken can impact how useful the information might be, particularly when considering dynamic targets. When constructing an RTI image, or using RSS data to track target position, a variety of factors can be considered. This thesis will examine the following factors:

- the information value of a given link, based on the number of pixels it crosses
- the currency of information in a report of RSS measurements
- the reporting history of a node, specifically the time it last reported

and will incorporate them into a "utility" metric that identifies an ideal node to report in the next time step. This approach assumes that a token passing, time division multiple access (TDMA) protocol is used, but rather than using a sequential transmission order as discussed in section 2.1.1 it proposes that the next node to transmit will be the node with the highest utility.

Wilson [6] performed an analysis of the lower error bound on estimating the image, $\hat{\mathbf{x}}$, in an RTI system. In doing so, the Fisher information matrix for data obtained from RSS measurements was determined to be [6]

$$\mathbf{J} = E\left[\left(\nabla_x[\ln\ P(\mathbf{y}|\mathbf{x})]\right)\left(\nabla_x[\ln\ P(\mathbf{y}|\mathbf{x})]\right)^T\right] \tag{3.3}$$

and when taking the noise statistics into account, this becomes [6]

$$\mathbf{J} = \gamma \mathbf{W}^T \mathbf{W} \tag{3.4}$$

where γ is a scale factor based on the noise statistics, and is not necessarily important for the purposes of this thesis. As such, $\mathbf{W}^T\mathbf{W}$ is used to determine the information value of a given link and pixel. Changing the notation slightly to distinguish between the traditional Fisher information matrix and the information matrix used in this thesis, the information matrix here is

$$\mathbf{I} = \mathbf{W}^T \mathbf{W}. \tag{3.5}$$

The trace of the above matrix represents the information value of each pixel, and can be mathematically represented as:

$$I_p = \sum_{p=1}^{P}\left(\sum_{l=1}^{L} W_{l,p}^2\right) \tag{3.6}$$

where l is the link number, p is the pixel number, P is the total number of pixels, and L is the total number of links. To find the information contained on a link rather than in a pixel, the order of the summations can be switched, and the inner summation represents the per-link information value:

$$I_p = \sum_{p=1}^{P} \left(\sum_{l=1}^{L} W_{l,p}^2 \right) = \sum_{l=1}^{L} \left(\sum_{p=1}^{P} W_{l,p}^2 \right), \text{where} \tag{3.7}$$

$$I_l = \sum_{p=1}^{P} W_{l,p}^2. \tag{3.8}$$

This is a metric by which the value of information in a given link can be quantified, with a higher number meaning the link contains more information about the scene within the WSN. If the values are then summed over the set of links made with node n, the information value per node can be found, such that

$$I_n = \sum_{l \in n} I_l \tag{3.9}$$

where $l \in n$ are all of the links made with node n. This provides a per-node information value which essentially represents which nodes receive the most information about the scene. By sorting this in descending order, the node transmission order for the first round of RSS reports in one of the token passing methods under test, discussed below in section 3.2, can be established. Using only the information metric would result in only the node with the highest information content transmitting repeatedly, which would essentially render the imaging useless: if no other node transmits, no RSS values would be reported, and the entire scene would be reported as empty.

To force the system to choose a different node to transmit, a "history" metric was introduced. The history metric tracks the last time a given node transmitted.

The longer it has been since a node has transmitted its report, the more valuable the report becomes because the more likely the entire report contains current, unreported information. Immediately after transmitting, a node's history value zeros out, because transmitting again from the same node would provide a report with the exact same information that was just received. The history metric for a given node n is mathematically defined as

$$H_n = 1 - e^{-\alpha_h t_h} \tag{3.10}$$

where α_h is a tuneable parameter to control the rate of decay, and t_h is the time elapsed since node n last transmitted, which can be expressed as $t_h = t_{now} - t_{tx}$ where t_{now} is the current time and t_{tx} is the time the node last transmitted. Note that history can also be expressed for each link with a given node, but will be the same value for all L links made with the given node n.

Another metric to take into consideration contained within every report in the WSN is termed "currency," which is a per-link quantity that captures how current a given RSS measurement within a report is. The motivation behind tracking the currency of each RSS measurement is that the older an RSS measurement is, the less valuable it is, particularly for a dynamic scene. If the information in an RSS measurement is not current in a dynamic scene, it can become irrelevant. The currency metric is mathematically defined by

$$C_l = e^{-\alpha_c t_c} \tag{3.11}$$

where α_c is a tunable parameter to control the rate of decay, and t_c is the time elapsed since the reporting node has received a report on link l, which can be expressed as $t_c = t_{now} - t_{rx}$ where t_{now} is the same as above and t_{rx} is the time since node n

received a report on link l to create an RSS measurement.

Using the three metrics of information (3.8), history (3.10), and currency (3.11) identified above, a third metric can be calculated to choose an ideal node to report next. This is the utility of the node and is calculated using

$$U_n = H_n \left[\sum_{l \in n} C_l I_l \right] \tag{3.12}$$

where $l \in n$ are all of the links formed with node n and p are all of the pixels in the estimated image. Figure 5 shows an example of all l links that are made with node $n = 54$. Table 1 summarizes the metrics discussed above, providing a succinct definition for each.

3.1.2 Wireless Sensor Network Model

The wireless sensor network modeled in this thesis utilizes 60 nodes arranged in a rectangle. Much of the work was done using a modeled dynamic scene where the cylindrical human model, defined in (2.21), traverses a rectangular path. This is shown in figure 6 below, where the outline of the image and the pixels contained in the image is represented by blue dotted lines, and the dynamic path model is represented by the red line with an arrow indicating clockwise movement. The nodes are represented by the black circles. The particular WSN configuration shown in figure 6 was chosen to reflect the current hardware setup that the AFIT RTI system uses, allowing for a more direct comparison between the model and previous experimental data collected from the physical system. An additional WSN configuration was also simulated with only 28 nodes and larger spacing between nodes to provide an example of a WSN with less information. This configuration is pictured in figure 7.

The imaging solution was obtained using the covariance-weighted least squares solution discussed in section 2.1.3.1. RSS measurements were modeled using (2.1)

Table 1: Summary of information and time-based metrics.

Metric	Symbol	Meaning	Equation
Information	I_l	Fisher information value for a given link l	(3.8)
	I_n	Fisher information value for a given node n	(3.9)
History	H_n	Scaling factor based on the last time a node n transmitted RSS values	(3.10)
Currency	C_l	Scaling factor based on the last time an RSS value was reported on link l	(3.11)
Utility	U_n	Utility value of a node found by multiplying the three metrics above	(3.12)

where $\mathbf{n}$ is a vector of independent, identically-distributed additive white Gaussian noise (AWGN) such that

$$\mathbf{n} \sim \mathcal{N}(\mathbf{0}, \sigma_n^2 \mathbf{I}) = \mathcal{N}(\mathbf{0}, \mathbf{N}) \tag{3.13}$$

The specific solution used took the form [16]

$$\hat{\mathbf{x}} = \left(\mathbf{W}^T \mathbf{N}^{-1} \mathbf{W} + \mathbf{C}_x^{-1}\right)^{-1} \mathbf{W}^T \mathbf{N}^{-1} \mathbf{y}, \text{where} \tag{3.14}$$

$$\mathbf{y} = \mathbf{W}\mathbf{x} + \mathbf{n} \tag{3.15}$$

where $\mathbf{C}_x$ is the covariance of the pixels in the image, and is defined in (2.31). Considering (3.13), (3.14) is equivalent to using the pi matrix defined in (2.30) to find the estimated image. A summary of the parameter values used for the RSS model and solution method is listed in table 2.

The model assumes that one round around the WSN takes one second. With 60 nodes, the time allotted to each node for transmission is $\tau_{tx} = 1/60^{\text{th}}$ of a second. Additionally, a provision was made to account for dropped packets. In the physical RTI system that AFIT uses, packets are frequently dropped due to multipath interference, poor line-of-sight to the base station, or just errors in the transmission. This is handled in the physical system by giving the transmitter another attempt at

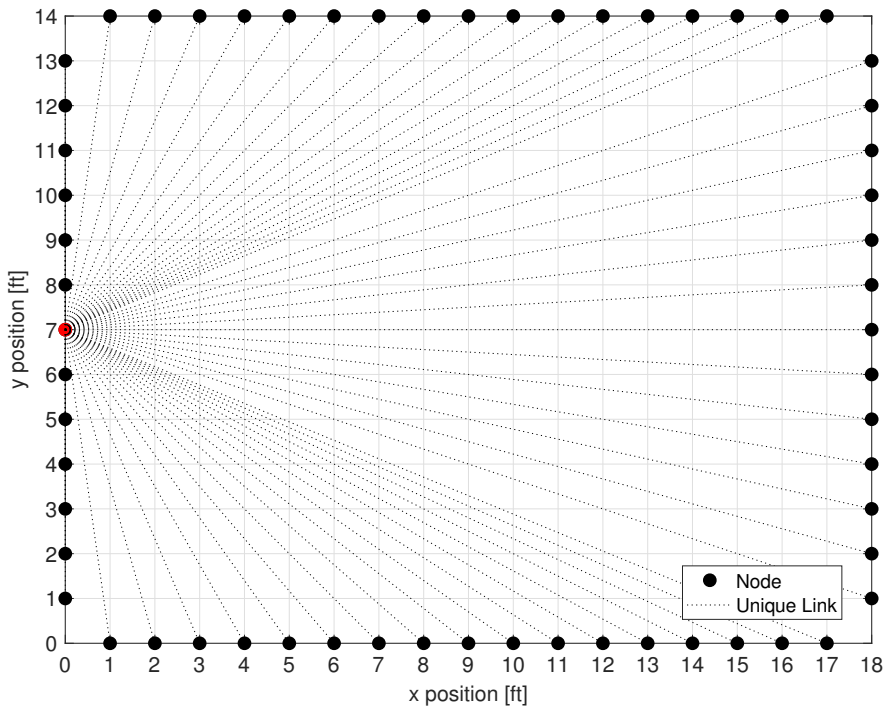

Figure 5: All links made with node $n = 54$, highlighted in red.

transmission, and then moves on in the normal order recording a NaN as the RSS measurement for the report that failed to successfully transmit. Upon image reconstruction, when the two RSS measurements are averaged, if a NaN value and good reading are found on the same link the good reading is used; if two NaN values are on the same link, a NaN is reported. For the imaging solution all NaN values are set to zero, and (2.23) is used to estimate the image.

To replicate this in the model, the report used in the event of a dropped packet is a report of all zeros. Reporting all zeros is the technique used by the AFIT RTI system, keeping the model a faithful representation of an existing physical system. While it is technically not the correct method, as reporting a zero indicates no change on a given link, few efficient alternatives exist to handle the NaN values that result from a dropped packet. The correct way to handle such a situation is to eliminate the

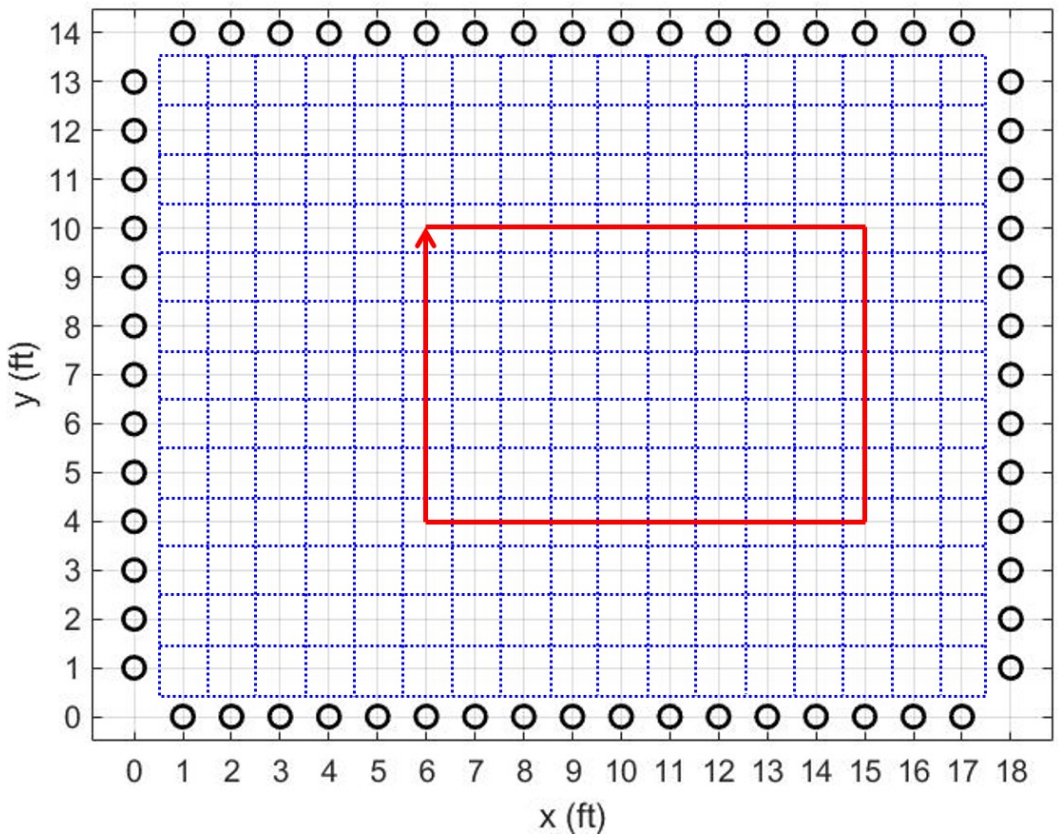

Figure 6: Modeled WSN with scene pixel outline and dynamic target path.

node from the model and recompute the weight matrix, but this is computationally burdensome. Another alternative could be using the last successful report from the node, which uses outdated information in a potentially dynamic scene, where the use of zeros essentially assumes no target is present. No matter the method used, a dropped packet results in a loss of information. A variety of packet loss rates were simulated for the experiments, and are summarized in table 3 and section 3.2.

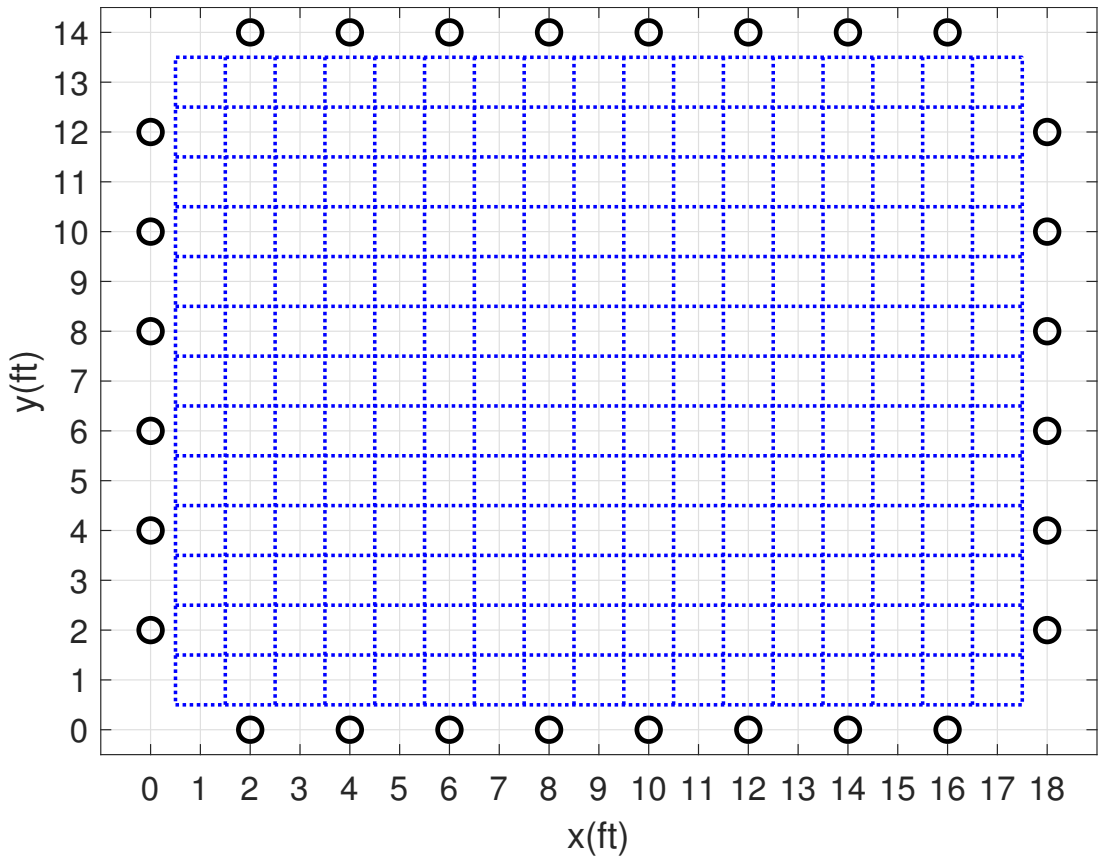

Figure 7: Modeled WSN with scene pixel outline utilizing 28 nodes and 2 ft node spacing.

Table 2: Parameters used for WSN model.

Variable	Parameter	Significance of Parameter
$\mathbf{C}_x$ (2.31)	$\sigma_x^2 = 0.1$ dB^2	Variance of the pixel intensity in the image.
	$\delta_c = 1.3$ ft	Tuneable space constant used to control the decay rate in the pixel covariance.
$\mathbf{W}^{NeSh}$ (2.14)	$\lambda = 0.03$ ft	Excess path length beyond foci of ellipse.
$\mathbf{x}$ (2.21)	$R_H = 1.3$ ft	Radius of cylindrical human model used to form truth image.
$\mathbf{N}$ (3.13)	$\sigma_n^2 = 16$ dB^2	Variance of the AWGN.

3.1.3 Position Tracking

To compare the utility selection method to the standard round-robin method, the maximum a posteriori (MAP) and the k-means methods of position estimation were used to track position over time and the performance of the different transmission orders was compared. The positioning error was calculated for the duration of the dynamic scene for each method to identify any differences in performance using the root-mean-squared error (RMSE), given by

$$\text{RMSE} = \sqrt{\frac{\sum_{m=1}^{M} (||\hat{\mathbf{p}}_m - \mathbf{p}_m||)^2}{M}} \tag{3.16}$$

where $\hat{\mathbf{p}}_m$ is the mth target position estimate, $\mathbf{p}_m$ is the mth true target position, each occurring in the same time instant, and M is the total number of true and estimated position coordinates. Additionally, the dispersion of the clusters used for the k-means calculation between the two methods was also compared, defined in [3] as

$$\sigma_{centroid} = \sqrt{\frac{\sum_{j=1}^{J} ||x_j - C||^2 \cdot \hat{x}_j}{\sum_{j=1}^{J} \hat{x}_j}} \tag{3.17}$$

where $||x_j - C||$ is the Euclidean distance between the jth pixel in the cluster and the cluster centroid, and $\hat{x}_j$ is the intensity of the jth pixel in the cluster. Weighting the distance between the pixel and centroid by the percent of the total intensity that the specific pixel represents ensures that pixels that just meet the threshold to be included in the cluster do not have an out-sized contribution to the dispersion of the cluster, as lower intensity values will typically be found farther from the centroid.

3.2 Simulation Set-up

The simulation runs were set up using the dynamic target path pictured in figure 6 with randomization added. The distance traveled in the x and y directions remained the same, but the top left corner of the rectangular path was shifted based on discrete uniform random variables such that $x_{shift} \sim \mathcal{U}\{-4, 1\}$ feet and $y_{shift} \sim \mathcal{U}\{-2, 2\}$ feet to keep the edges of the dynamic target path within the scene being monitored by the WSN. Randomization was added to the path location in order to provide some level of randomization for the simulation runs because the utility-based and round robin node selection methods are purely deterministic. Figure 8 shows what three path realizations with a randomly drawn starting point might look like, as well as marking the boundary inside of which the paths can be drawn. In the figure, path one has $[x_{shift}, y_{shift}] = [0, 0]$ feet, path two has $[x_{shift}, y_{shift}] = [-4, 2]$ feet, and path three has $[x_{shift}, y_{shift}] = [-1, -2]$ feet.

Three different token passing methods were simulated for 1000 realizations of the dynamic path. The token passing methods will be referred to by the following definitions:

- Method 1: Standard, sequential token passing method for all communication rounds, as discussed in paragraph 2.1.1.

- Method 2: The first round of RSS reports from each node uses the standard sequential token passing, all subsequent rounds prioritize the next node to transmit based on the utility values determined by (3.12).

- Method 3: The first round of RSS reports prioritizes the transmission sequence based on the information value per node shown in (3.9), all subsequent rounds prioritize the next node to transmit based on the utility values determined by (3.12).

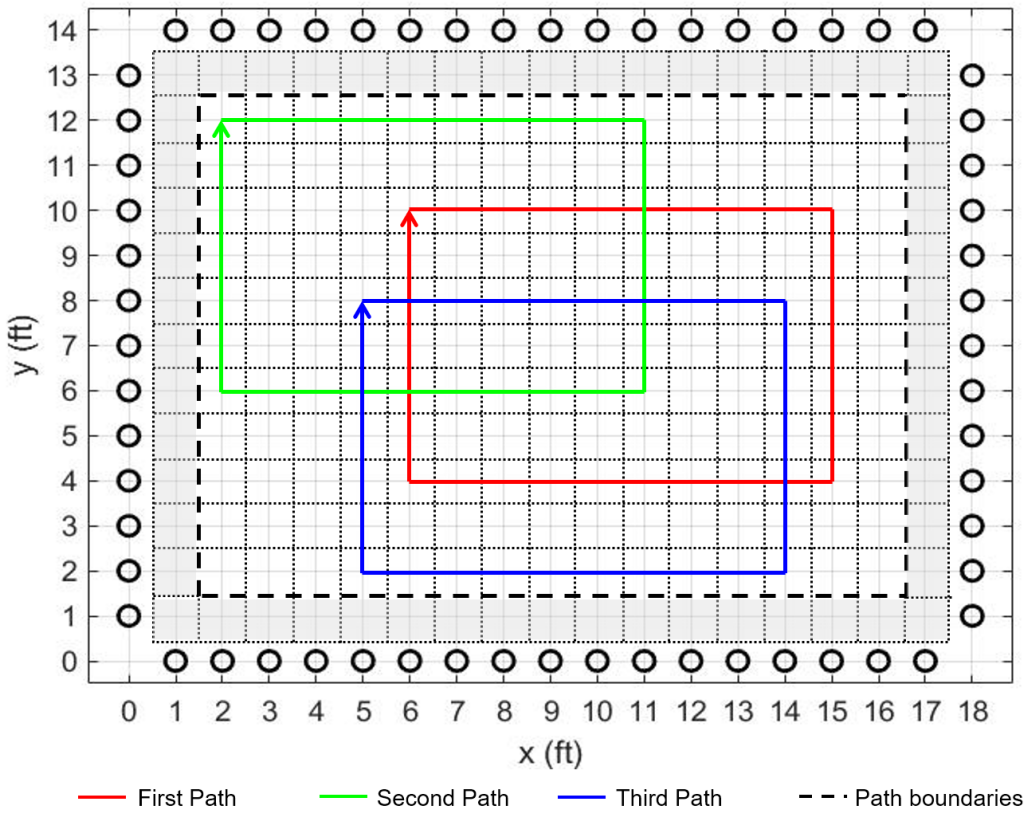

Figure 8: Illustration of three paths with randomized starting points.

The k-means clustering and MAP localization methods were used to track the position of the target over each realization of the dynamic path, and the dispersion of the k-means cluster was also calculated. Five experiments were run, using 1000 realizations of the dynamic path each. Table 3 summarizes the differences between each experiment. The average RMSE, k-means cluster dispersion, and average RMSE over time were calculated for each packet loss rate.

Table 3: List of experiments conducted.

Experiment	Weight Matrix	Parameter	Packet Loss Rates	WSN Configuration
1	NeSh (2.14)	$\lambda = 0.03$ ft	0%, 20%, 50%, 85%	60 nodes 1 ft spacing
2	NeSh (2.14)	$\lambda = 0.06$ ft	0%, 20%, 50%, 85%	60 nodes 1 ft spacing
3	NeSh (2.14)	$\lambda = 0.015$ ft	0%, 20%, 50%, 85%	60 nodes 1 ft spacing
4	Line (2.15)	N/A	0%, 20%, 50%, 85%	60 nodes 1 ft spacing
5	NeSh (2.14)	$\lambda = 0.06$ ft	0%, 20%, 50%, 85%	28 nodes 2 ft spacing

IV. Results and Analysis

4.1 Node Selection Based on Highest Utility

Implementing the utility metric, U_n, in (3.12) and selecting the node with the highest utility to transmit using the Network Shadowing (NeSh) weight model results in a non-sequential selection pattern where the nodes with the highest information metric are typically selected more often than those with a lower information metric. This is reflected in figure 9 which shows the total number of reports each node makes when the system chooses a node to transmit 108000 times. This was done by simulating the wireless sensor network (WSN) using the experiment 1 setup with 0% packet loss, summarized in table 2, running for thirty minutes to ensure there were enough node selections to reach a steady run-time state. Note that the vertical axis showing the total number of reports starts at 1400 to better visualize the difference between the bars.

Figure 10 shows the same data arranged side-by-side in a histogram, overlaid on the information values for each node, obtained from (3.9). This shows that the pattern in the number of times that each node reports is driven largely by the information metric, specified in (3.6), but it is important to note that unless other nodes report, no matter the information value, no new information will be received. In addition to showing that the utility selection method largely relies on the information value of each node, the result highlights the fact that the utility selection method as developed in section 3.1.1.2 is deterministic.

Figure 11 shows the utility and history for node 54 over time on the same time axis for one iteration of the dynamic scene illustrated in figure 6. Node 54 was chosen because it is a high-information node that transmits more frequently than other nodes, making it more likely that an underlying pattern would emerge over

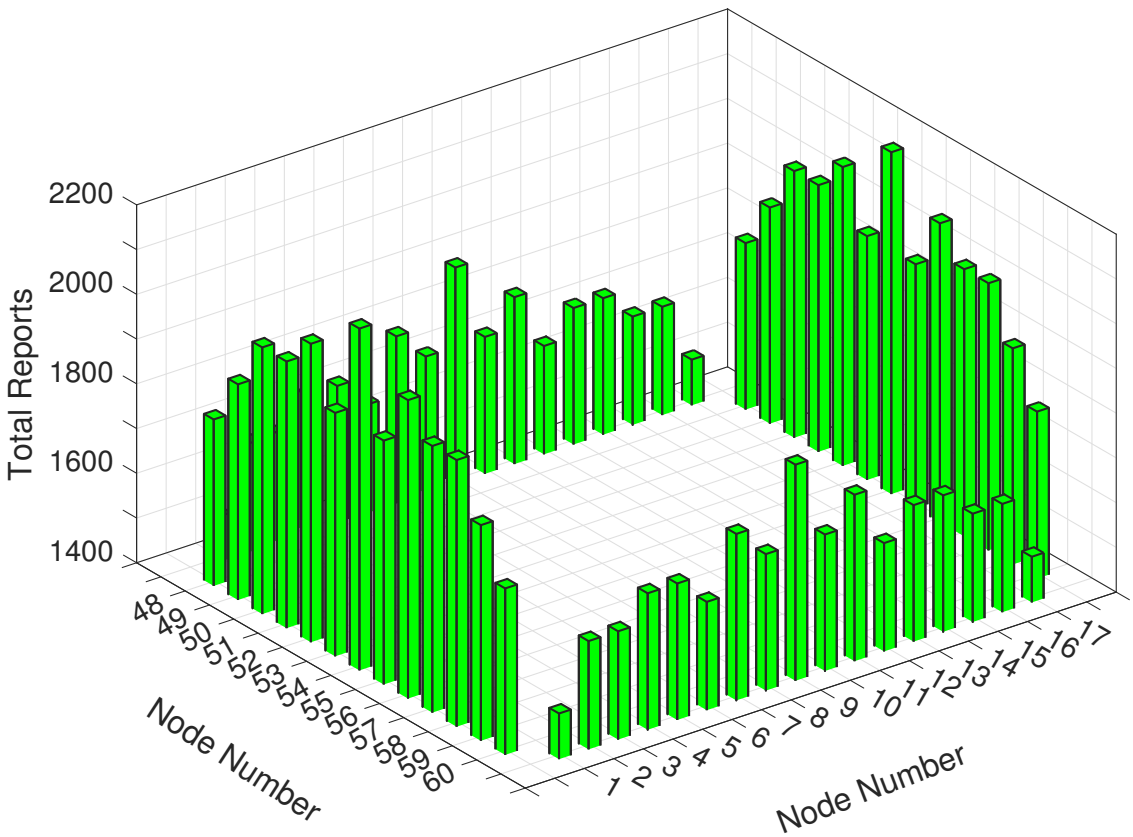

Figure 9: Number of reports per node for 108000 reports, arranged in the WSN setup.

more transmissions. Examining the two, it is clear that the history of a node has the intended effect: upon transmit, the history of a node is set to zero, driving the utility to zero as well, making that node the least useful to transmit in the next time step. Given that the history for a given node is the same across all links created with that node, there is no link-by-link effect. This provides a fairly coarse control that readily achieves its intended purpose: forcing a different node selection for the next transmission. There is no apparent underlying pattern in either the utility or the history that seems to have an effect on the relative frequency that the node is selected to transmit.

Where the history metric provides a coarse control to ensure no back-to-back repeat transmissions, the currency metric provides a much finer control with a less

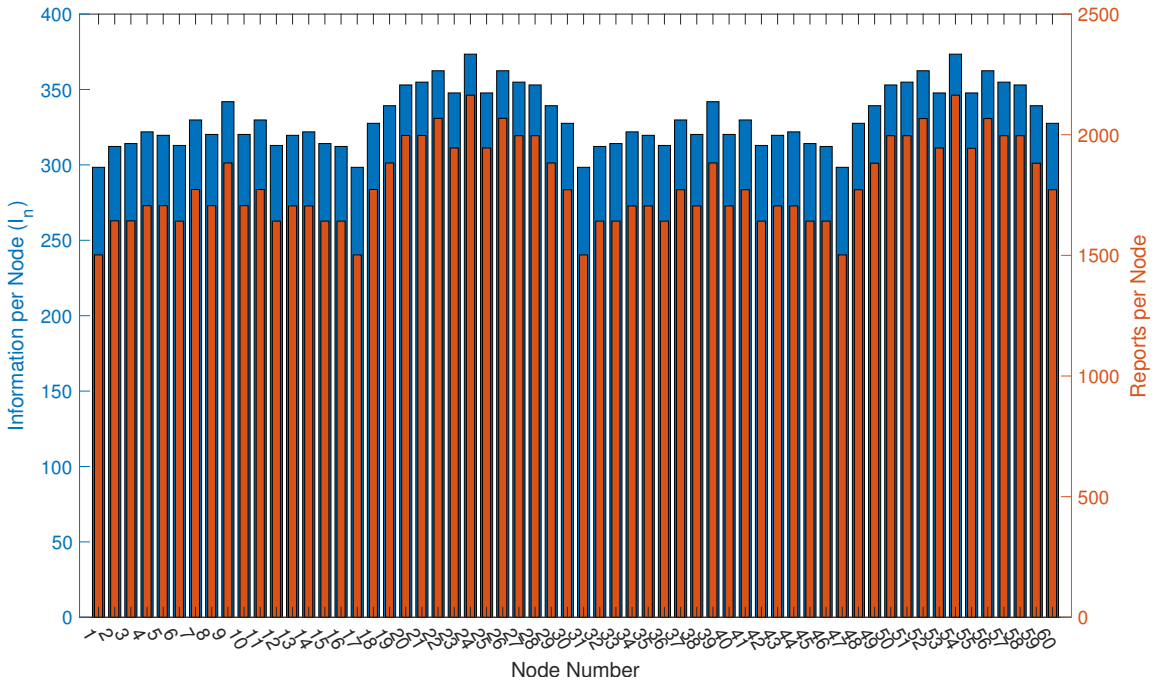

Figure 10: Information value for each node overlaid with number of reports per node for 108000 reports selected for highest utility.

impactful effect on the utility of a given node. Figure 12 shows the currency over time for a high information value link and a low information value link. The high information link transmits 41 times total while the low information link transmits 25 times over a 31 second time span. Changing the decay rate for the currency, α_c, does not drastically impact the behavior of the system, but can change the relative selection frequency of specific nodes by a small amount.

While figure 12 provides a view of the currency for two links across the duration of the entire dynamic scene, figure 13 provides a close-up view of the same links in the same realization of the dynamic scene over only a few seconds. The close-up helps illustrate the fact that the higher information link reports nearly twice as often, and shows how little the difference is between the minimum value of the high information link currency and low information link currency. This difference is amplified when the α_c decay rate is higher, reducing the impact that a given link has on a node's overall

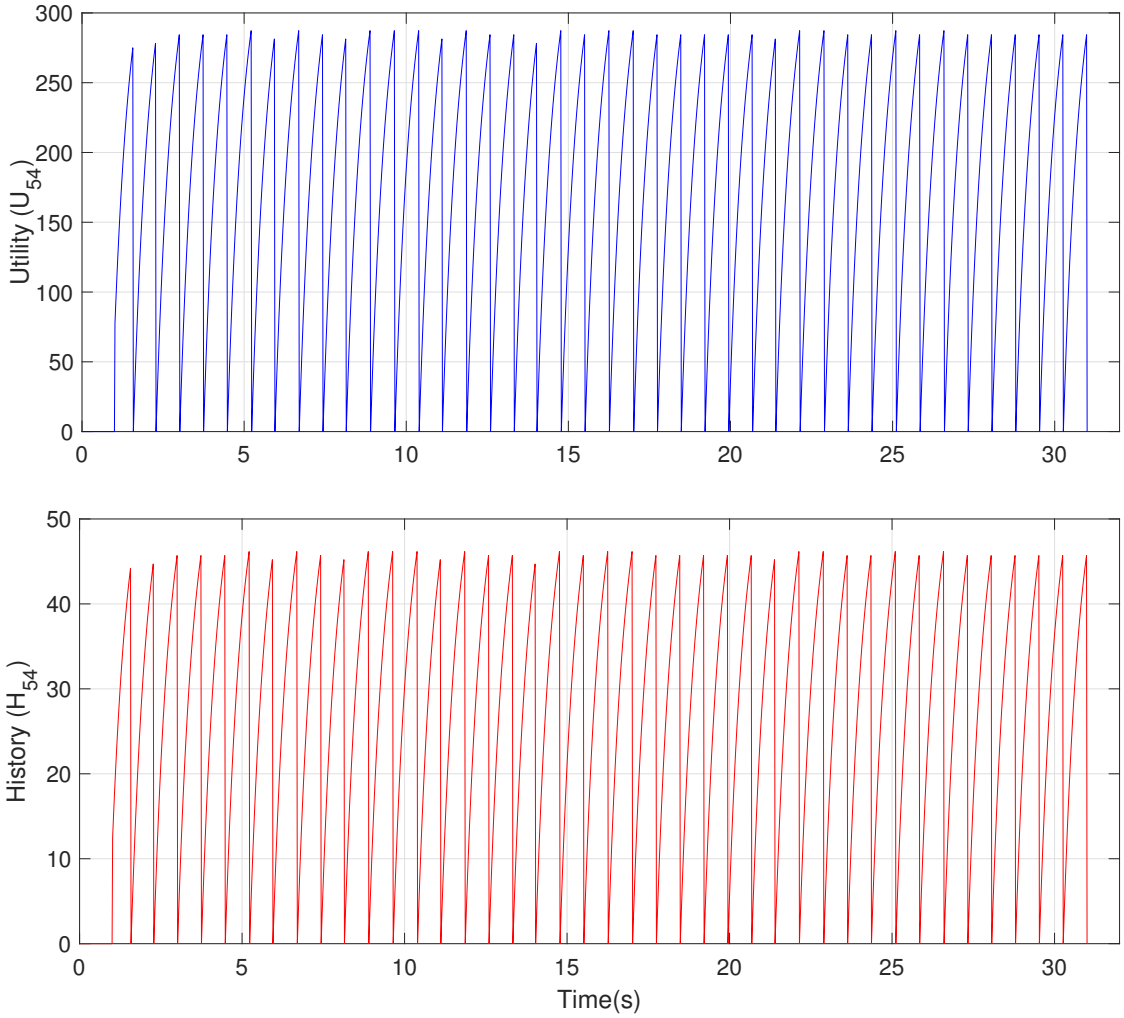

Figure 11: Utility and history for node 54 over time.

utility value. The reverse is true when reducing α_c. Figure 14 shows an illustration of the two links, where it can be seen that the high information link passes directly through the center of many pixels, and the lower information link passes diagonally through only a few pixels.

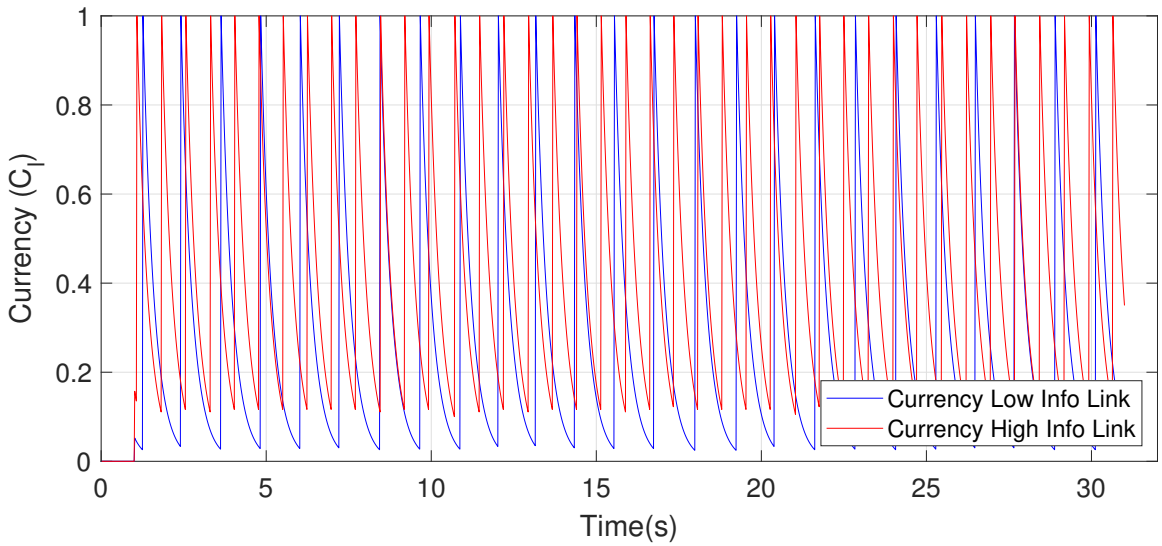

Figure 12: Currency values for links between nodes 54 and 24 (high information value) and nodes 54 and 2 (low information value).

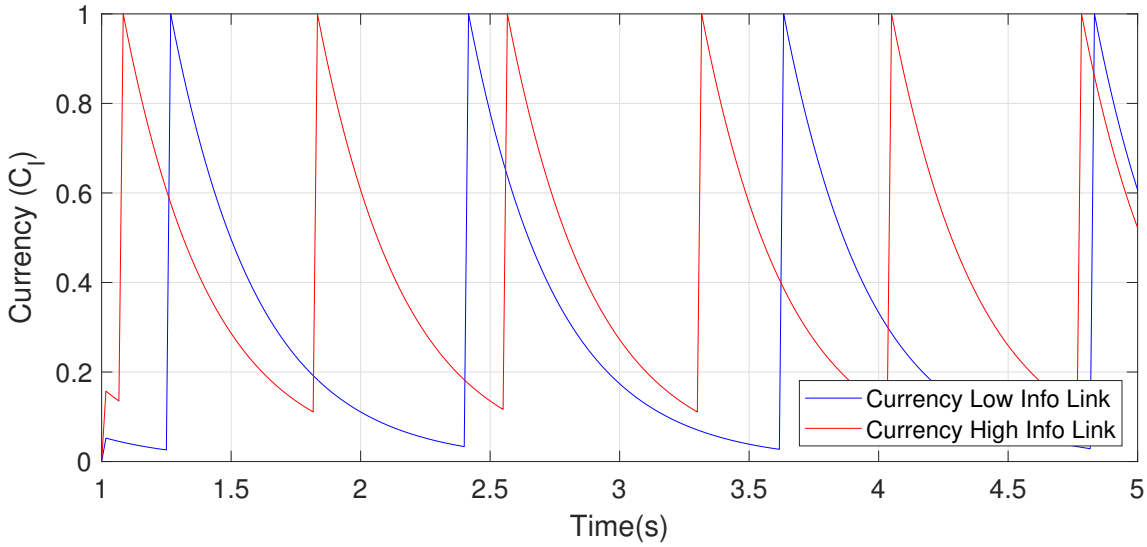

Figure 13: Close-up on currency values for links between nodes 54 and 24 (high information value) and nodes 54 and 2 (low information value) in the first four seconds.

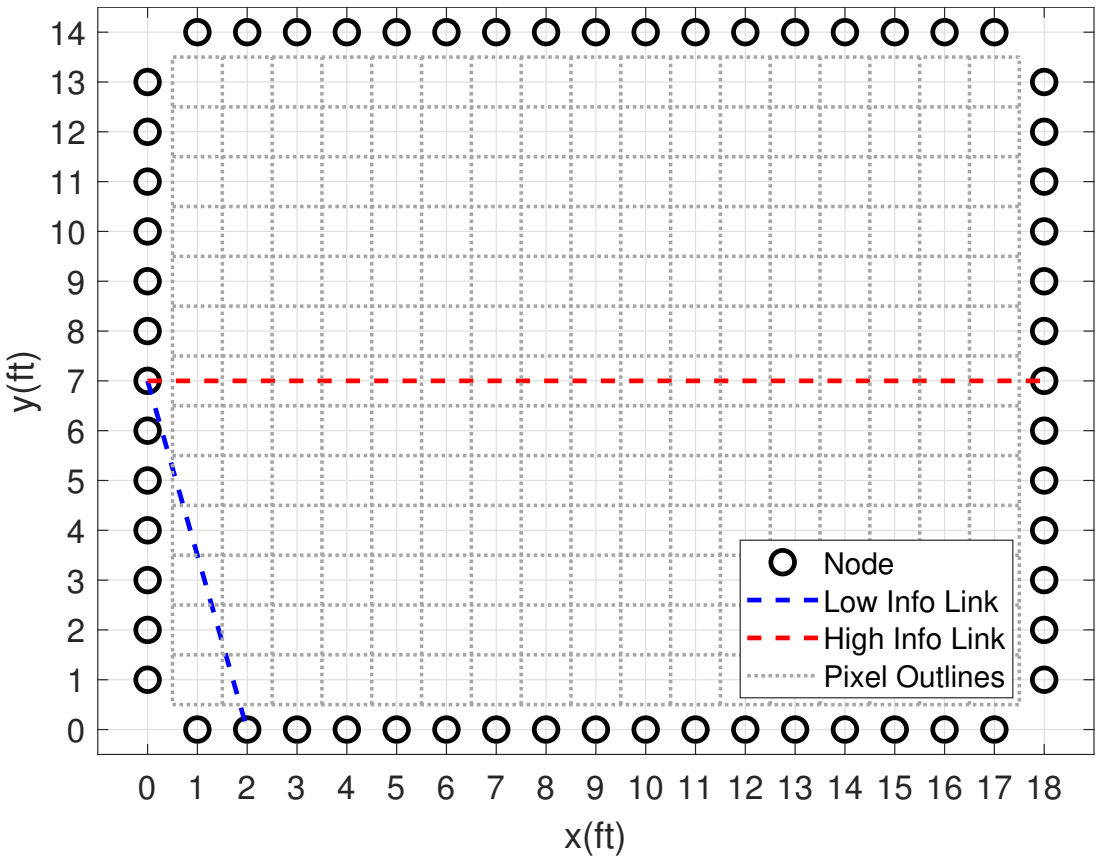

Figure 14: Illustration of links starting at node 54 and ending at nodes 2 (low information link) and 24 (high information link).

4.2 Position Tracking

The impact on the relative transmission frequency for the nodes when using the utility metric can be clearly seen in the section above. Rather than having one transmission per node per communication round, the information value of a given link leads to an emphasis on reporting the received signal strength (RSS) for the most information dense links. This section explores the actual impact on position tracking that using the utility metric provides. Figure 15 illustrates the output of the simulation. Each run provides a position estimate using the K-means cluster centroid and the maximum a posteriori (MAP) estimate. Additionally, the dispersion of clusters used to find the centroid was calculated.

4.2.1 Experiment 1 Results

Using the simulation setup described in section 3.1.3, the root-mean-squared error (RMSE) for the K-means and MAP estimates and the average dispersion across all K-means estimates over 1000 random realizations of the dynamic path were calculated. The 95% confidence interval for each of these metrics was also calculated and the information is displayed in figure 16. To reiterate the token passing methods under test: method 1 is the standard, sequential token passing method; method 2 uses sequential token passing until all nodes have reported once, then switches to prioritizing the node with the highest utility; and method 3 prioritizes the initial transmission sequence based on the information value of each node, then switches to prioritizing the node with the highest utility. From figure 16, it can be seen that the K-means centroid position RMSE and MAP estimate RMSE are statistically identical between all token passing methods during steady-state operation of the WSN, and the K-means cluster dispersion is higher when using method 3. Examining the results for the full path duration in figure 17, which takes into account the transient

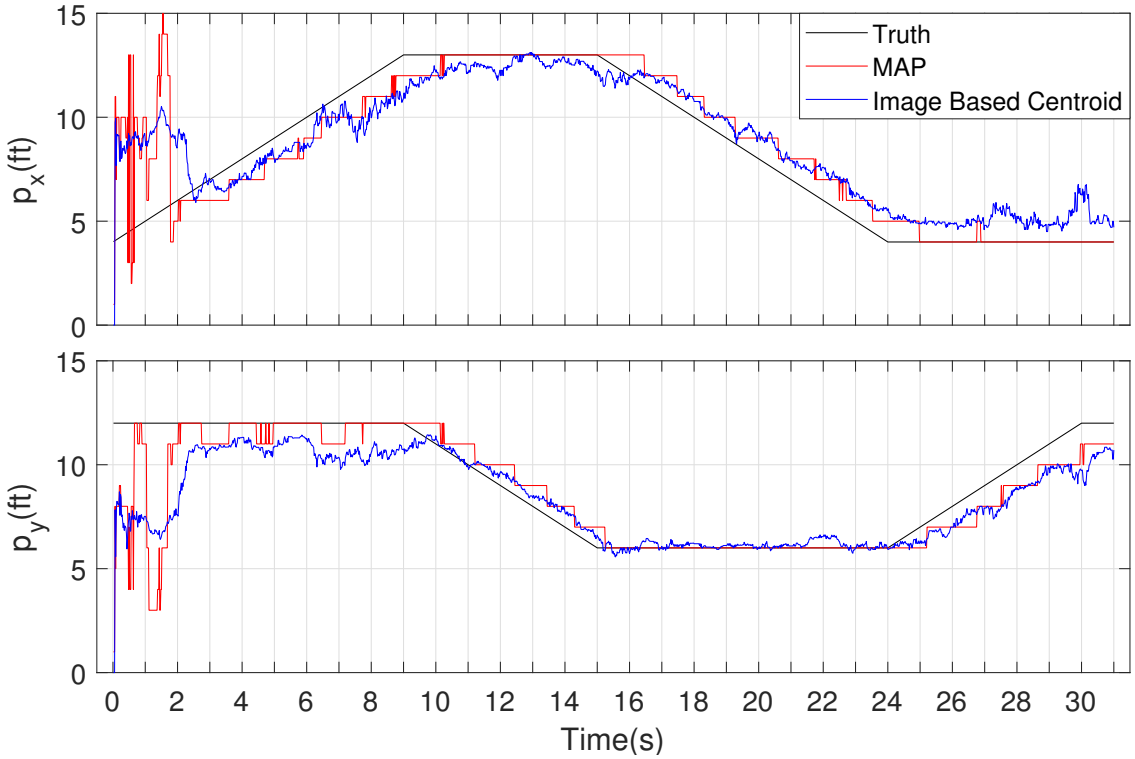

Figure 15: Position tracking results for one run of the MAP and image-based centroid localization methods for the x (top) and y (bottom) directions using method 3.

position estimates during the formulation of the first few frames of the image, shows that method 3 has lower RMSE, while method 1 and method 2 yield statistically identical RMSE for the position estimates. Interestingly, the K-means dispersion is still higher for method 3, despite the lower error on the centroid position estimate.

Figure 18 shows the centroid and MAP estimate RMSE for all three token passing methods versus time. The shaded area indicates the first five seconds that were trimmed to determine the steady-state RMSE for each method. These first five seconds reveal a major reason why method 3 performs better when considering the full path duration. The RMSE during this initial transient period is higher overall for methods 1 and 2, even though method 3 has slightly higher error for a longer period of time. The implication of this data is that method 3 takes slightly longer to reach a steady-state operation, but has lower overall error on the initial estimates. Important

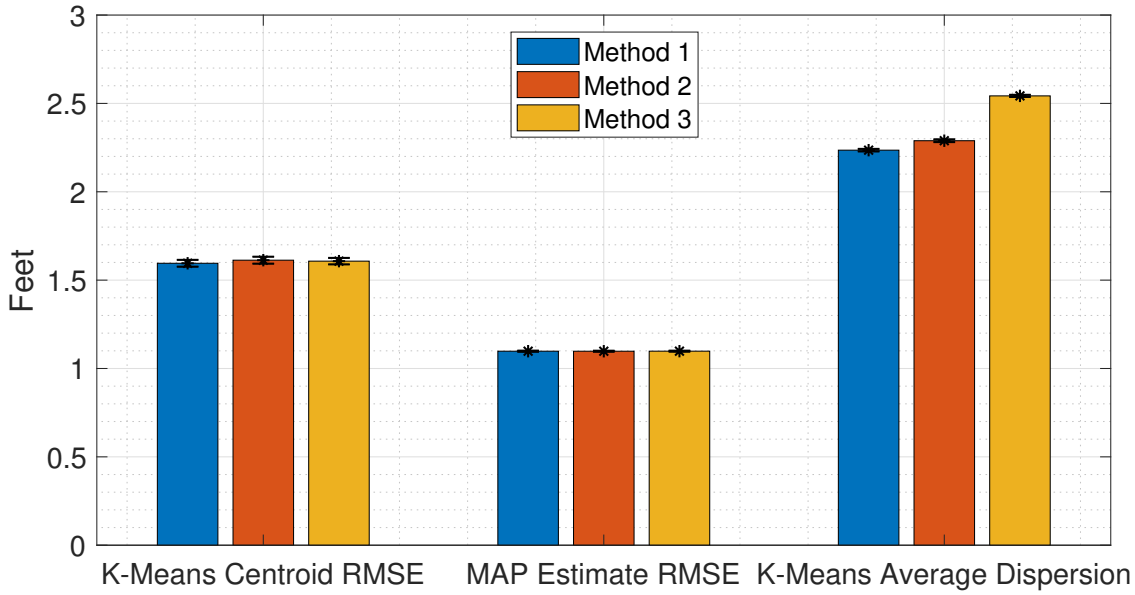

Figure 16: Experiment 1 RMSE and K-means averaged dispersion with 95% confidence intervals over 1000 realizations of the dynamic path during steady state runtime, with 0% packet loss.

to note, however, is that the magnitude of the initial error while using method 3 is larger than or close to the same length as the longest leg of the dynamic path over which the target is being tracked.

Figures 19 and 20 show the RMSE results when the average packet loss of 20% experienced in the Air Force Institute of Technology (AFIT) radio tomographic imaging (RTI) system is added to the simulation. There does not appear to be a major difference between the 0% and 20% packet loss scenarios, with the K-means centroid estimates showing nearly-identical performance and the MAP estimates showing identical performance during steady state tracking. Taking the full duration of the path and tracking into account, method 3 outperforms method 1 and method 2 again due to the initial error as discussed above.

Similar to figures 19 and 20, figures 21 and 22 show results from increasing the packet loss percentage even further from 20% to 50%. Figure 21 shows that token passing method 2 and 3 result in lower RMSE for both the K-means and MAP

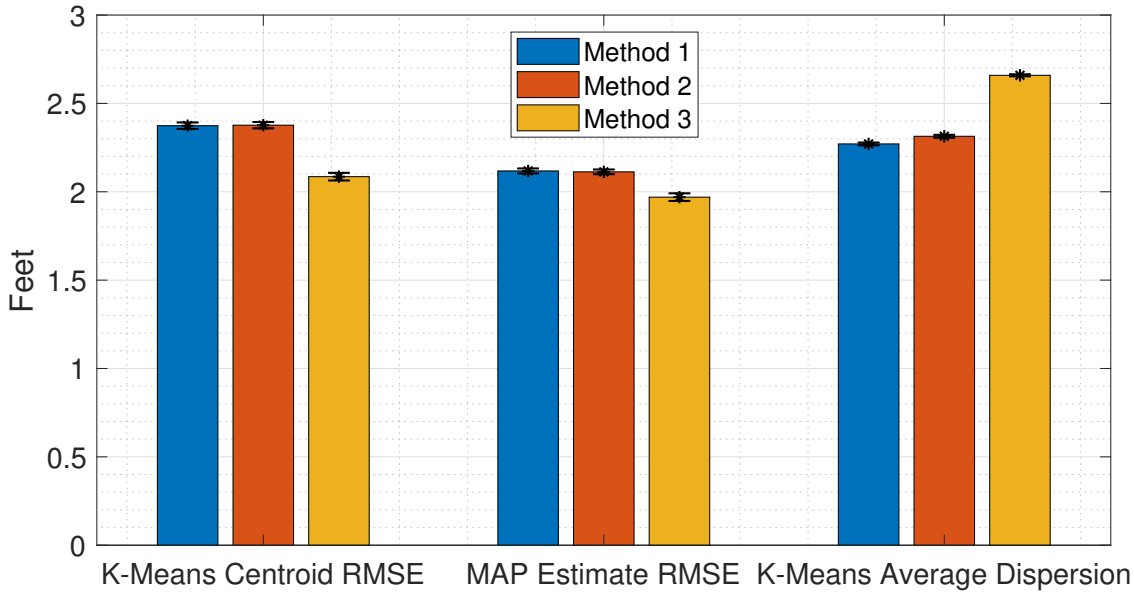

Figure 17: Experiment 1 RMSE and K-means averaged dispersion with 95% confidence intervals over 1000 realizations of the dynamic path for full path duration, with 0% packet loss.

tracking methods. Figure 22 shows that the same trend of token passing method 3 outperforming the other two when considering the full tracking duration. Additionally, method 2 also outperforms method 1 for the full tracking duration when there is 50% packet loss.

Figures 23 and 24 reinforce the findings from the previous 20% and 50% packet loss scenarios. With 85% packet loss, similar results to the 50% packet loss scenario are obtained. Methods 2 and 3 outperform method 1 when looking at both steady-state performance and tracking error over the full duration, and method 3 has a slight edge over method 2 when considering the full duration. An important note must be made on the magnitude of the tracking error, however. The longest leg of the dynamic path is 9 feet long, and the tracking error in the 85% packet loss scenario is nearly half of that; additionally, it is approximately 25% of the x-axis length in the overall scene and approximately 30% of the y-axis length of the overall scene. This indicates that while a slight edge can be gained from using method 2 or 3 in a high packet

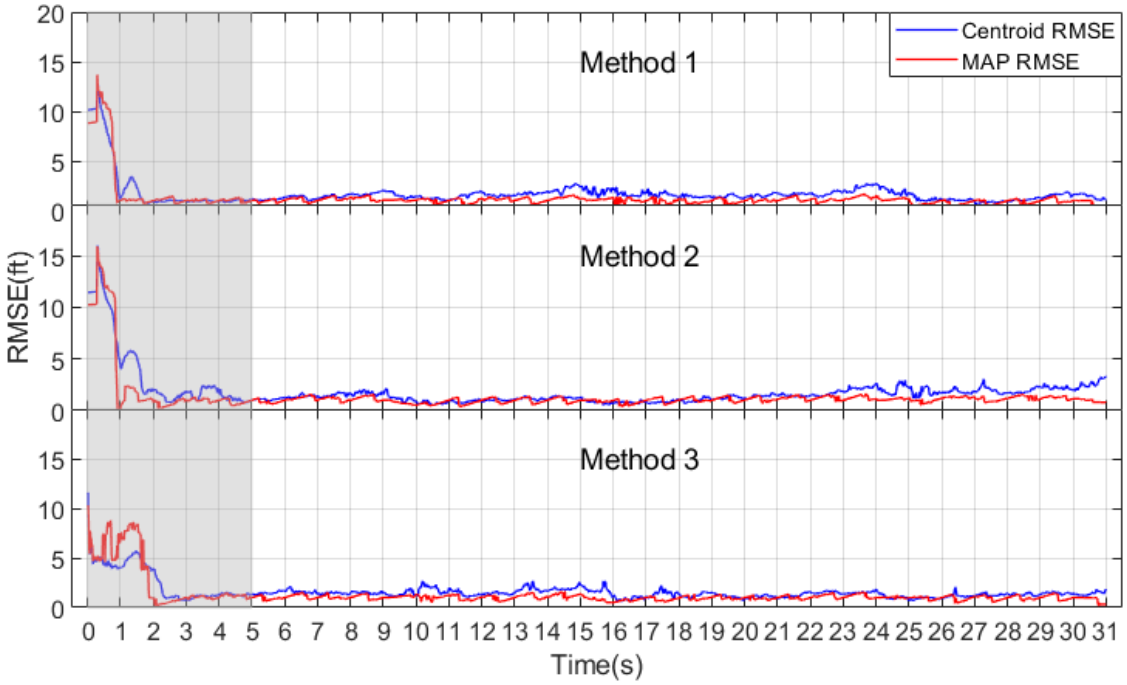

Figure 18: Experiment 1 RMSE versus time for the three methods averaged over 1000 realizations, shaded portion indicates transient data that was removed to obtain the "steady-state" RMSE results.

loss scenario, for the specific context and scene size used for the simulations in this thesis, the amount of overall error would potentially render any position estimate only slightly better than a random guess.

Overall, the results imply that as information is lost, prioritizing reports from nodes that have the most, and the most current, information about the scene results in more accurate localization. Logically it follows that a WSN with fewer nodes, and therefore less information about the scene it is surveilling, could potentially benefit from the use of token passing methods 2 or 3. This reasoning informed the configuration used for experiment 5. The other experiments listed in table 3 were conducted and the results are reported below; however, in the interest of clarity and brevity, only the results for the steady-state runtime for the 0% and 50% packet loss scenarios are displayed in this section, as they best illustrate the impact of the utility-

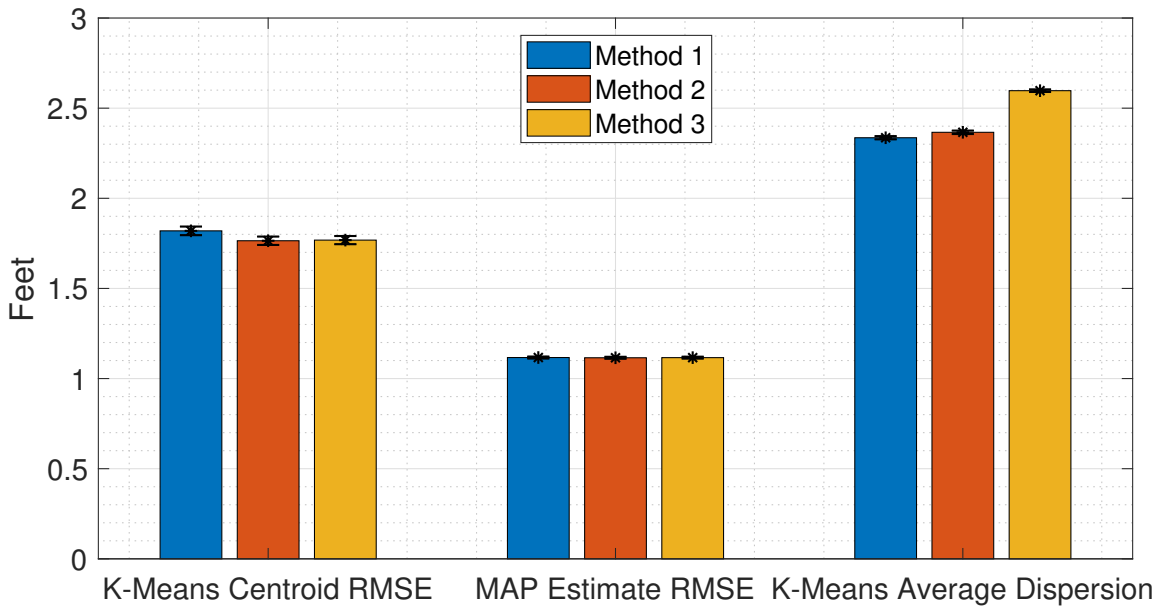

Figure 19: Experiment 1 RMSE and K-means averaged dispersion with 95% confidence intervals over 1000 realizations of the dynamic path during steady state runtime, with 20% packet loss.

prioritized token passing methods. The remaining results are displayed in Appendix A.

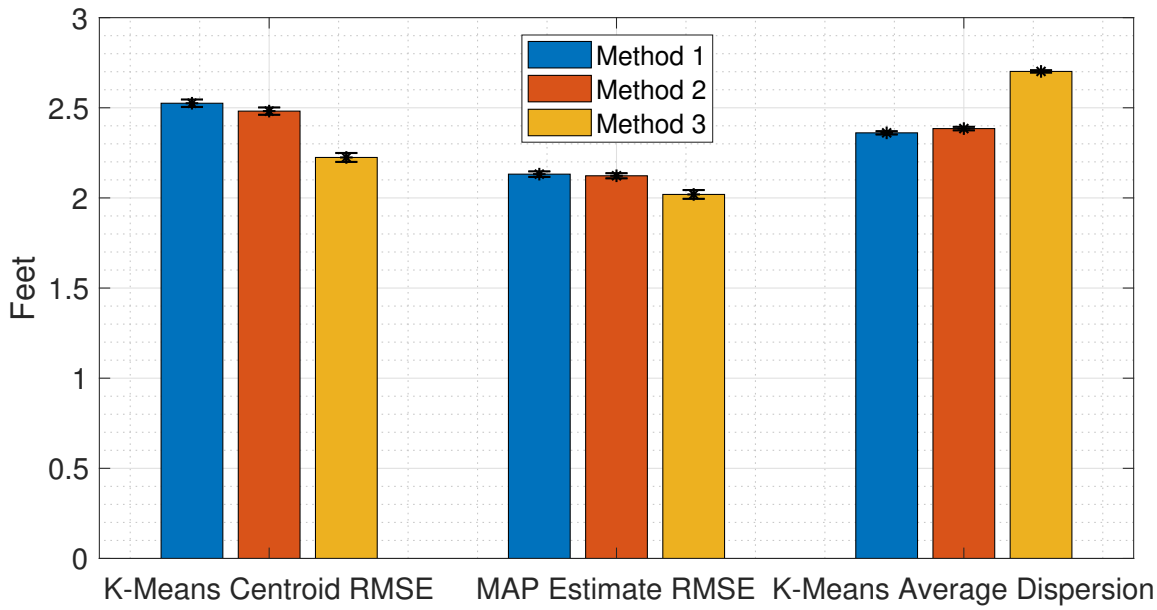

Figure 20: Experiment 1 RMSE and K-means averaged dispersion with 95% confidence intervals over 1000 realizations of the dynamic path for full path duration, with 20% packet loss.

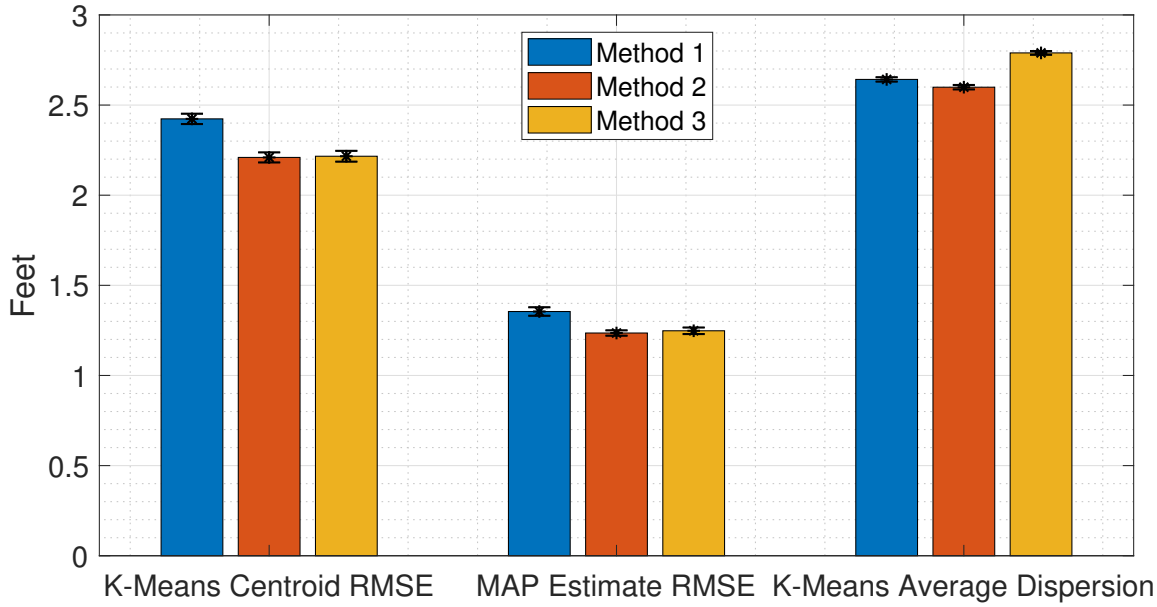

Figure 21: Experiment 1 RMSE and K-means averaged dispersion with 95% confidence intervals over 1000 realizations of the dynamic path during steady state runtime, with 50% packet loss.

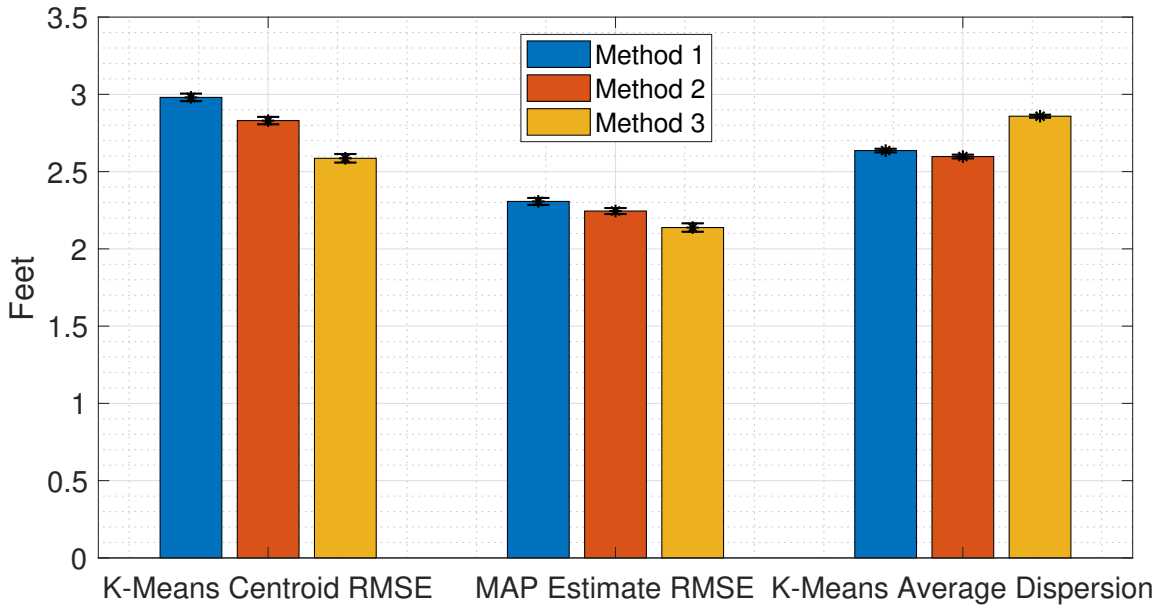

Figure 22: Experiment 1 RMSE and K-means averaged dispersion with 95% confidence intervals over 1000 realizations of the dynamic path for full path duration, with 50% packet loss.

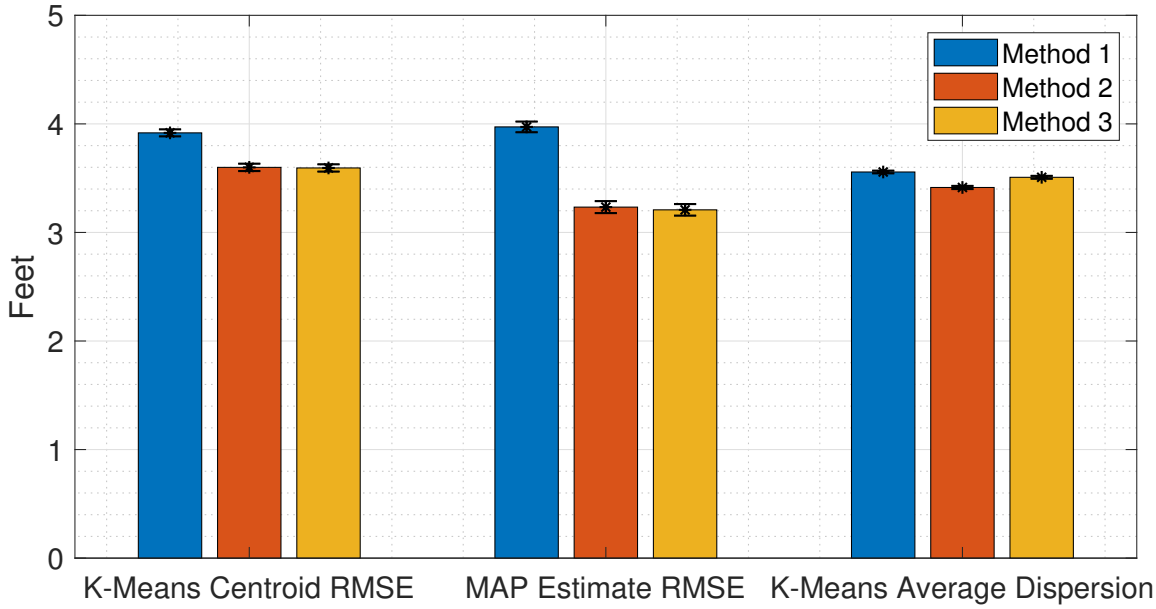

Figure 23: Experiment 1 RMSE and K-means averaged dispersion with 95% confidence intervals over 1000 realizations of the dynamic path during steady state runtime, with 85% packet loss.

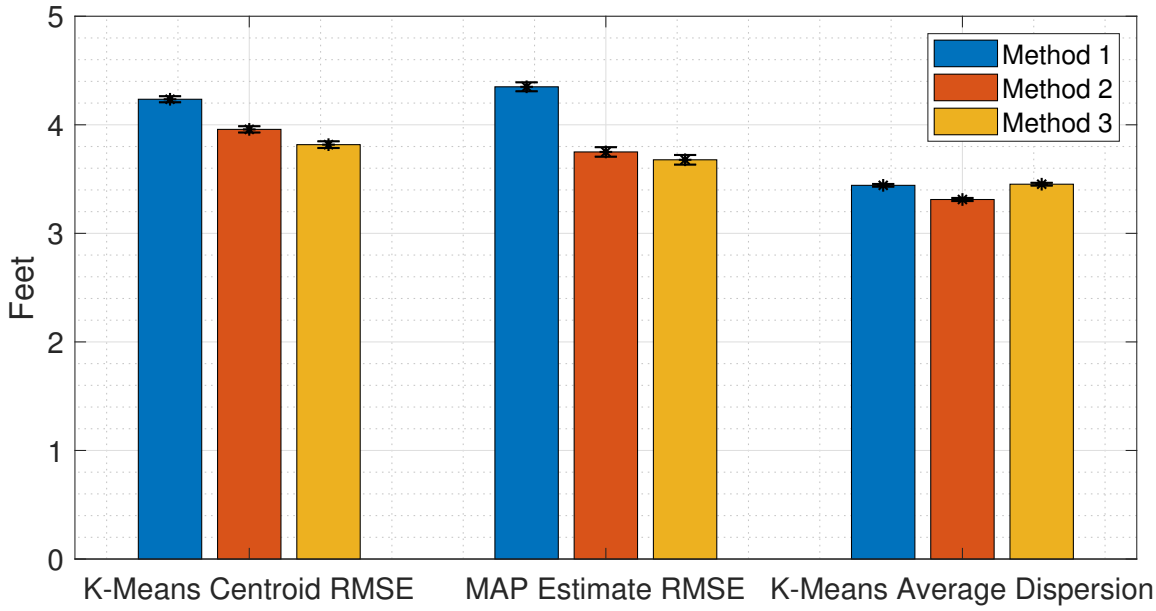

Figure 24: Experiment 1 RMSE and K-means averaged dispersion with 95% confidence intervals over 1000 realizations of the dynamic path for full path duration, with 85% packet loss.

4.2.2 Experiment 2 Results

Experiment 2 essentially uses a different model by changing the excess path length parameter for the NeSh weight matrix model. For this experiment, the excess path length parameter was doubled from experiment 1, so that $\lambda = 0.06$ ft. This widens the ellipse with the two transceivers as the foci, making each link more information-dense. Given the results of experiment 1, this implies that token passing methods 2 and 3 would be less impactful to localization performance even in scenarios with increasing packet loss. This is reflected in figures 25 and 26. While figure 26 does show a small gain in localization performance for the K-means localization, the gain in accuracy for the MAP localization is marginal.

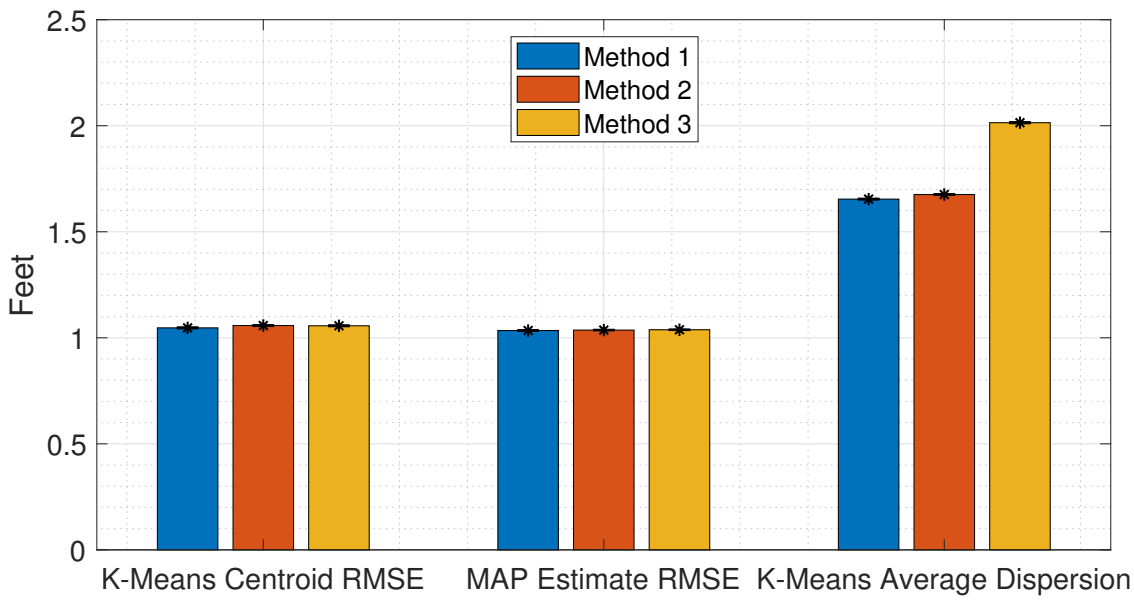

Figure 25: Experiment 2 RMSE and K-means averaged dispersion with 95% confidence intervals over 1000 realizations of the dynamic path during steady state runtime, with 0% packet loss.

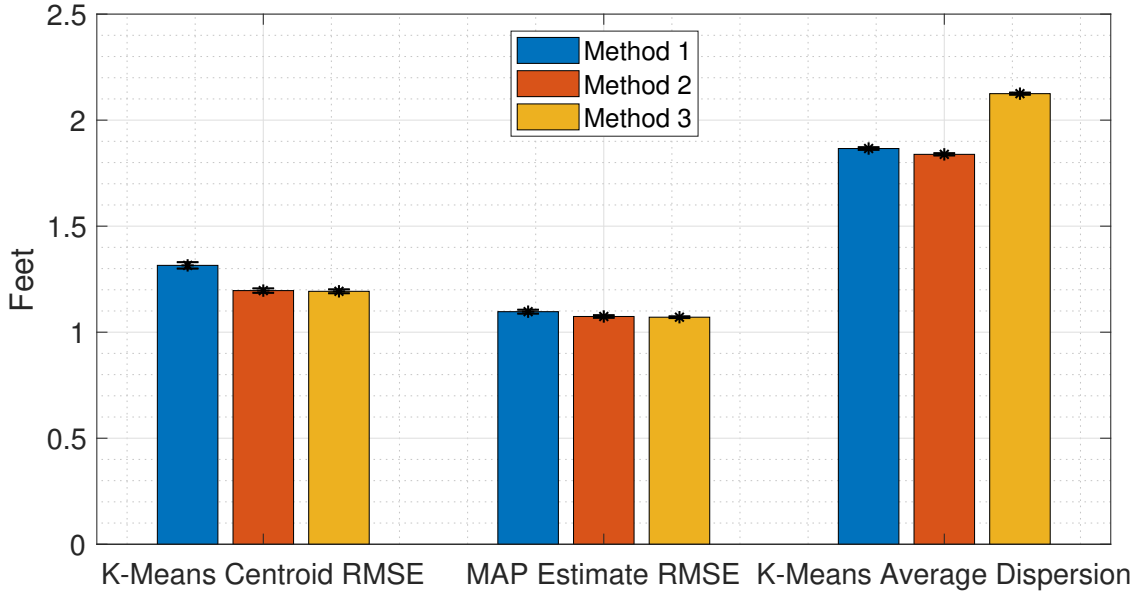

Figure 26: Experiment 2 RMSE and K-means averaged dispersion with 95% confidence intervals over 1000 realizations of the dynamic path during steady state runtime, with 50% packet loss.

4.2.3 Experiment 3 Results

Similar to experiment 2, experiment 3 again varies the excess path length parameter. Utilizing $\lambda = 0.015$ ft, the model narrows the ellipse representing the link between transceivers. This effectively reduces the information on a given link and suggests that token passing methods 2 and 3 would be more beneficial. The results shown in figures 27 and 28 do not entirely support this conclusion. For an ideal, 0% packet loss scenario, methods 2 and 3 underperform method 1 when using K-means localization. MAP localization provides identical performance. In a scenario with 50% packet loss using k-means localization, all methods perform identically when considering the 95% confidence intervals; however, method 2 and method 3 provide better localization when using the MAP estimate.

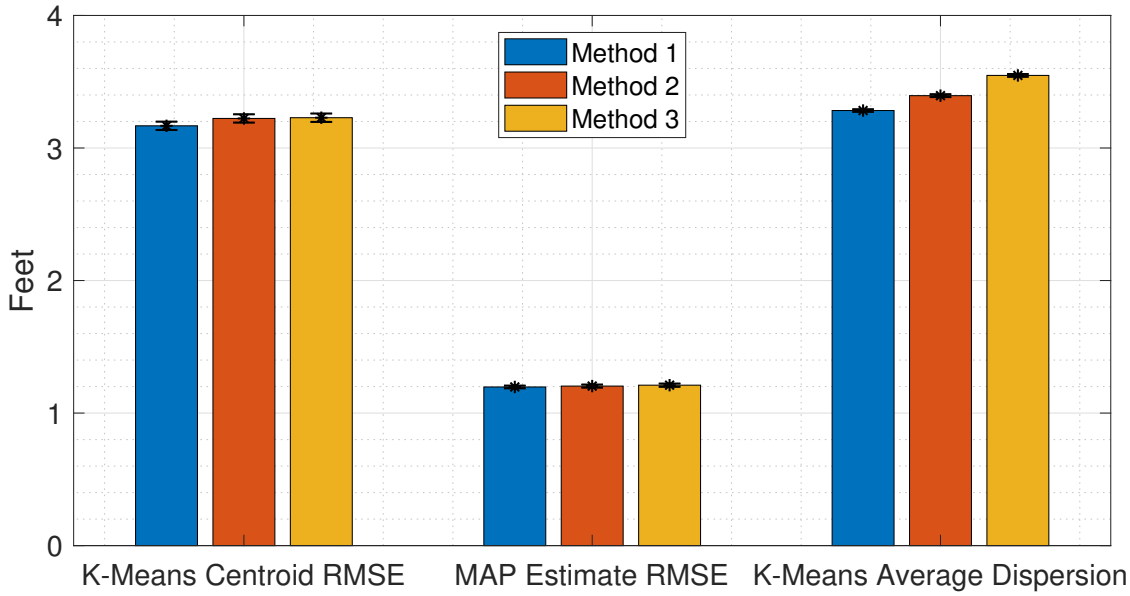

Figure 27: Experiment 3 RMSE and K-means averaged dispersion with 95% confidence intervals over 1000 realizations of the dynamic path during steady state runtime, with 0% packet loss.

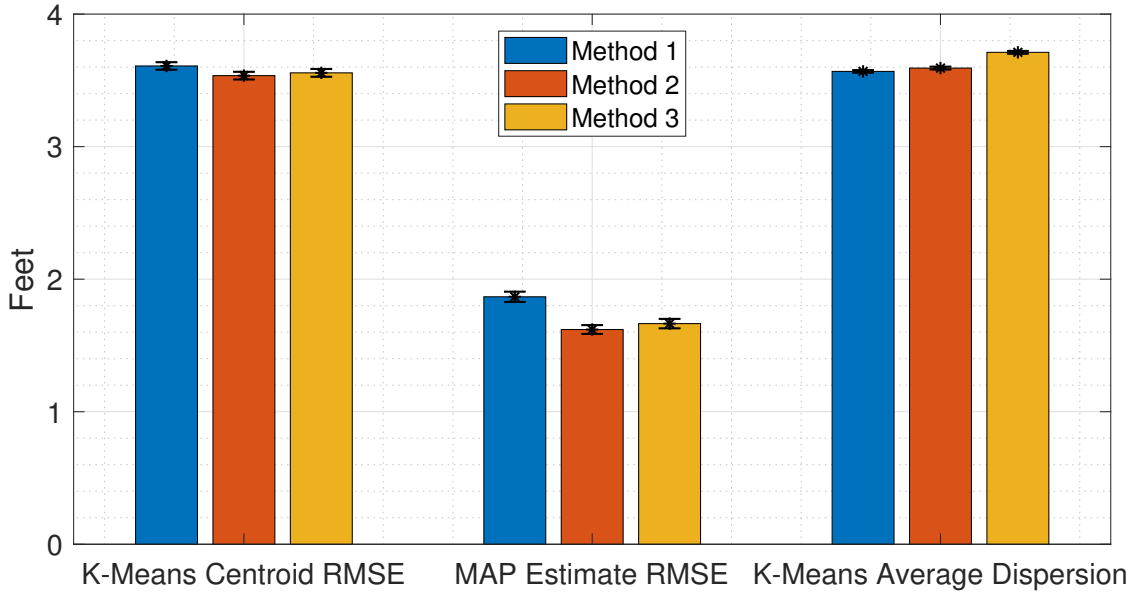

Figure 28: Experiment 3 RMSE and K-means averaged dispersion with 95% confidence intervals over 1000 realizations of the dynamic path during steady state runtime, with 50% packet loss.

4.2.4 Experiment 4 Results

Experiment 4 changes the weight matrix model from the NeSh model to the line model. Again, this implies there might be less information about the scene on a given link, but this trivializes the differences between the two models. Figure 29 shows that methods 2 and 3 are marginally less accurate than method 1 when using the line weight matrix, essentially making the three methods equivalent for the 0% packet loss case. Figure 30 shows an increase in accuracy using both K-means and MAP localization, reinforcing the trend that token passing method 2 and 3 provide increased accuracy when less information is available.

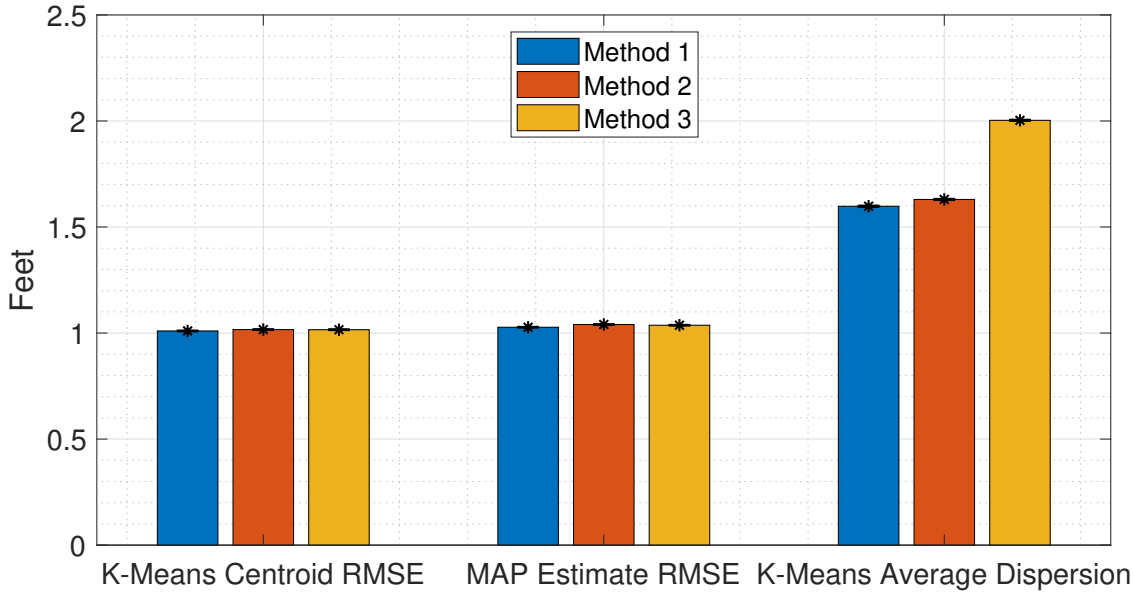

Figure 29: Experiment 4 RMSE and K-means averaged dispersion with 95% confidence intervals over 1000 realizations of the dynamic path during steady state runtime, with 0% packet loss.

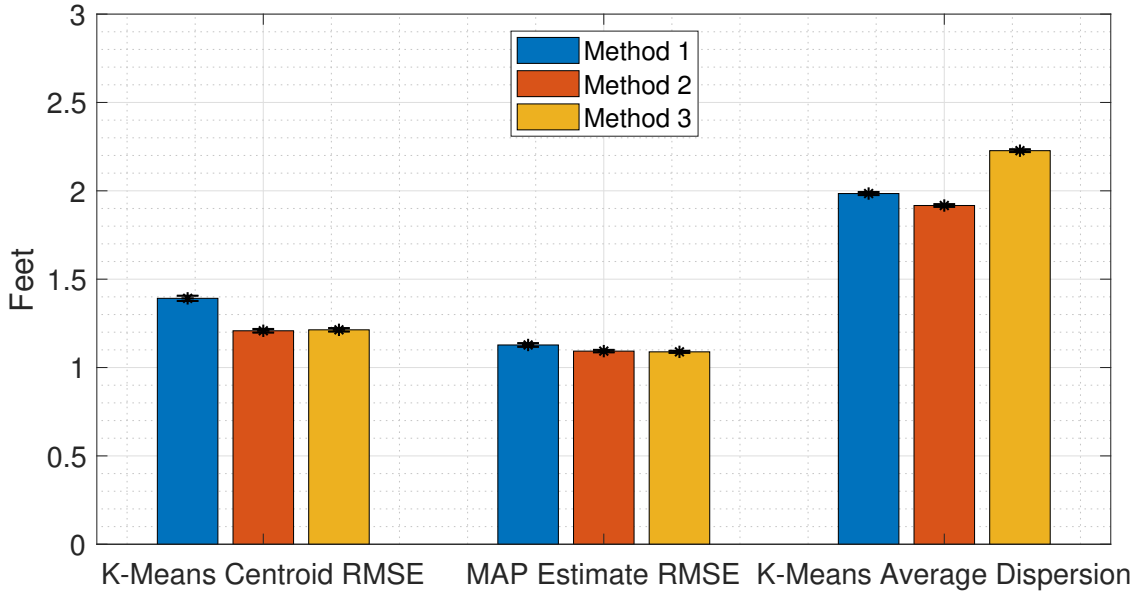

Figure 30: Experiment 4 RMSE and K-means averaged dispersion with 95% confidence intervals over 1000 realizations of the dynamic path during steady state runtime, with 50% packet loss.

4.2.5 Experiment 5 Results

Experiment 5 uses the NeSh weight matrix model with $\lambda = 0.06$ ft again, but reduces the number of nodes in the WSN to 28 while increasing the spacing between each node to 2 ft. Figure 31 shows the 0% packet loss scenario, where method 3 marginally outperforms the other two methods when using K-means localization, but the MAP estimates provide identical performance. Figure 32 shows the results with 50% packet loss, where methods 2 and 3 outperform method 1 using either form of localization.

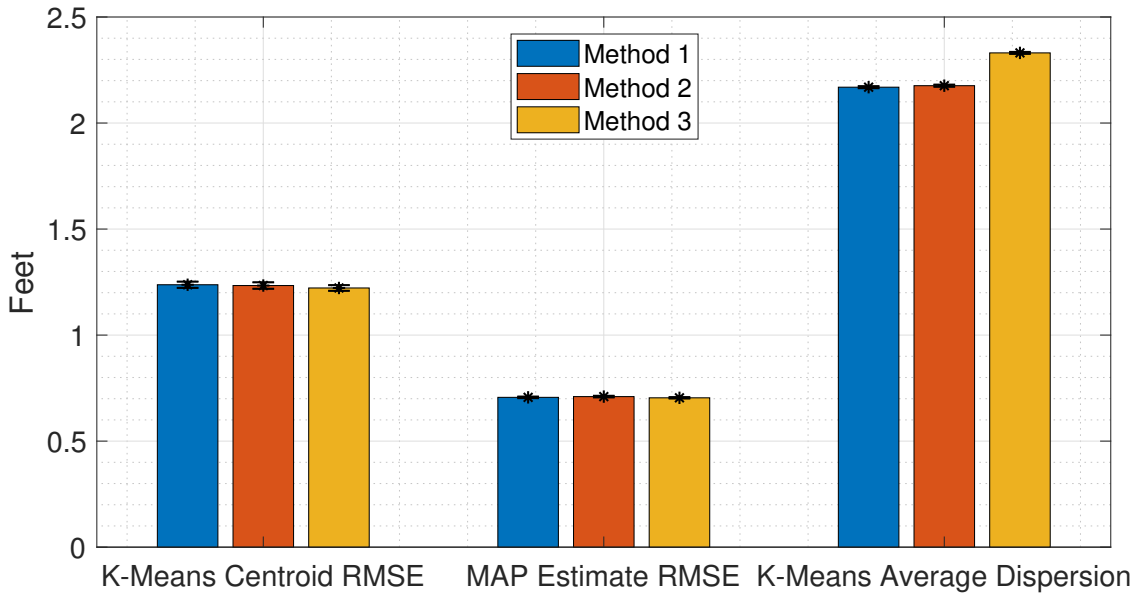

Figure 31: Experiment 5 RMSE and K-means averaged dispersion with 95% confidence intervals over 1000 realizations of the dynamic path during steady state runtime, with 0% packet loss.

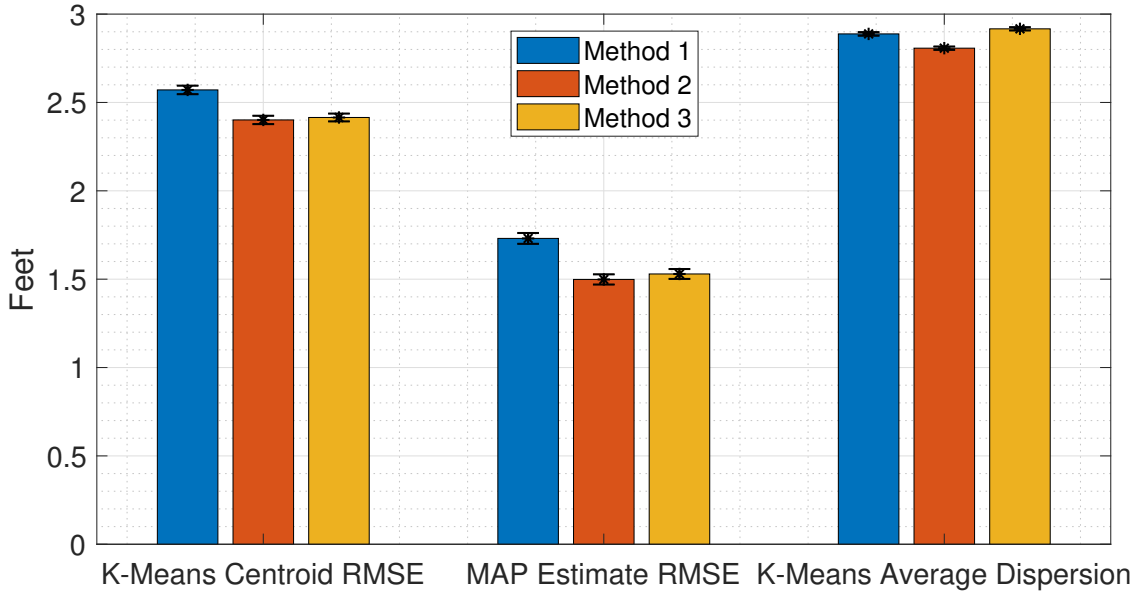

Figure 32: Experiment 5 RMSE and K-means averaged dispersion with 95% confidence intervals over 1000 realizations of the dynamic path during steady state runtime, with 50% packet loss.

V. Conclusions

The work performed in this thesis presents an alternative token passing methodology to the standard sequential token passing method frequently used for radio tomographic imaging (RTI) systems. The token passing methodology is based partly on the Fisher information matrix of the image being produced, which was used to produce a metric for dynamically selecting an optimal node to transmit in the next time step. The intent behind the implementation and testing of this dynamic transmission method was to improve the target localization and tracking performance of RTI systems. An improvement in performance would further the utility of RTI as a useful tool in many force protection applications for the United States Armed Forces ranging from emergency response, like structure fires and active shooter scenarios, to military operations in urban terrain (MOUT) where potential combatants could be localized through walls before entering to clear a building.

An information metric was developed for each node in the wireless sensor network (WSN), and the time that passed since each node in the WSN transmitted was tracked to create two other metrics. These three metrics were combined to form a fourth metric which was used to determine the node with the most, and most recent, information about the scene being monitored. This selection process was used many times to determine any long-term patterns that might emerge. The process was found to be largely driven by the information metric and purely deterministic. Three token passing methods were then tested over 1000 trials for four different packet loss scenarios: 0%, 20%, 50%, and 85% packet loss. The methods used were:

- Method 1: Standard, sequential token passing method for all communication rounds, as discussed in paragraph 2.1.1.

- Method 2: The first round of received signal strength (RSS) reports from each

node uses the standard sequential token passing, all subsequent rounds prioritize the next node to transmit based on the utility values determined by (3.12).

- Method 3: The first round of RSS reports prioritizes the transmission sequence based on the information value per node shown in (3.9), all subsequent rounds prioritize the next node to transmit based on the utility values determined by (3.12).

The performance of the three methods was evaluated by averaging the root-mean-squared error (RMSE) from the K-means clustering centroid position estimate and maximum a posteriori (MAP) position estimate. It was found that improvement in performance is largely context dependent and can vary when considering various models and WSN configurations. However, token passing methods 2 and 3 generally resulted in a lower tracking error than method 1 as packet loss increased, implying that prioritizing reports from nodes with more information about the scene can result in better localization performance when fewer measurements are available.

The results from this work show, through modeling and simulation, a proof-of-concept for optimizing the node transmission sequence through the utility metric presented in (3.12). Specifically, in the context of high-packet loss scenarios, the dynamic, utility-driven, token passing methods have been shown to provide localization and tracking at a lower overall level of error.

5.1 Future Work

While providing a proof-of-concept for the methods presented, further exploration to verify and validate the results could provide more appropriate contexts, and implementation of the methods on a physical system. Future work to further develop the token-passing methodology should include:

- Modeling and simulation similar to this thesis using different weight matrices and other WSN parameters.
- Implementation of state-space tracking methods such as Kalman filters and evaluation of the effects of the token passing methods on the resultant tracking accuracy
- Further exploration of the differences when the following aspects of the WSN are changed:
  - Number of nodes in WSN
  - Geometry/placement of nodes in the WSN
  - Size of the scene being monitored by the WSN
  - Pixel size
- Exploration of the effects of changing the target size, speed, and path.
- Application of the token-passing methods presented in this thesis to experimental RSS data collected on each link.
- Implementation of the token-passing methods presented in this thesis to a physical RTI system, and subsequent exploration of the system's performance.

Appendix A. Additional Results

1.1 Experiment 2 Results

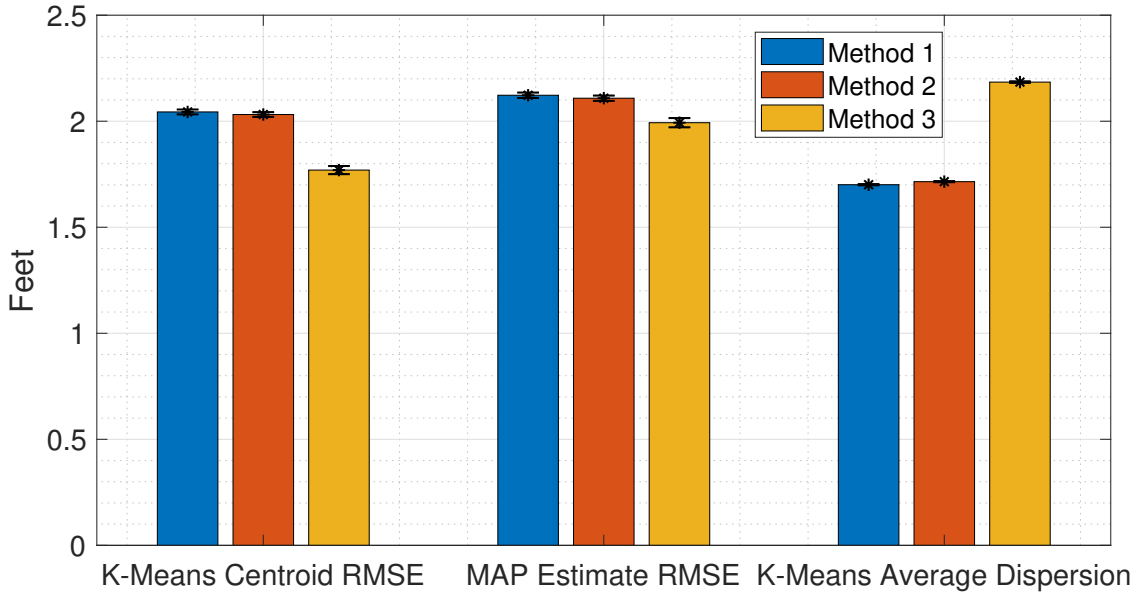

Figure 33: Experiment 2 RMSE and K-means averaged dispersion with 95% confidence intervals over 1000 realizations of the dynamic path for full path duration, with 0% packet loss.

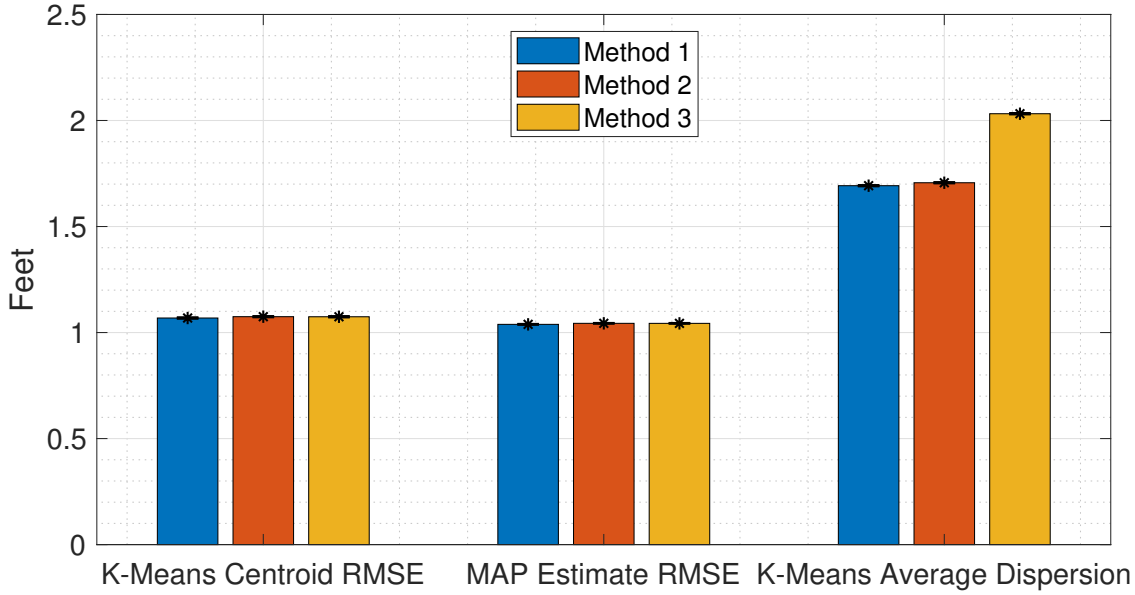

Figure 34: Experiment 2 RMSE and K-means averaged dispersion with 95% confidence intervals over 1000 realizations of the dynamic path during steady state runtime, with 20% packet loss.

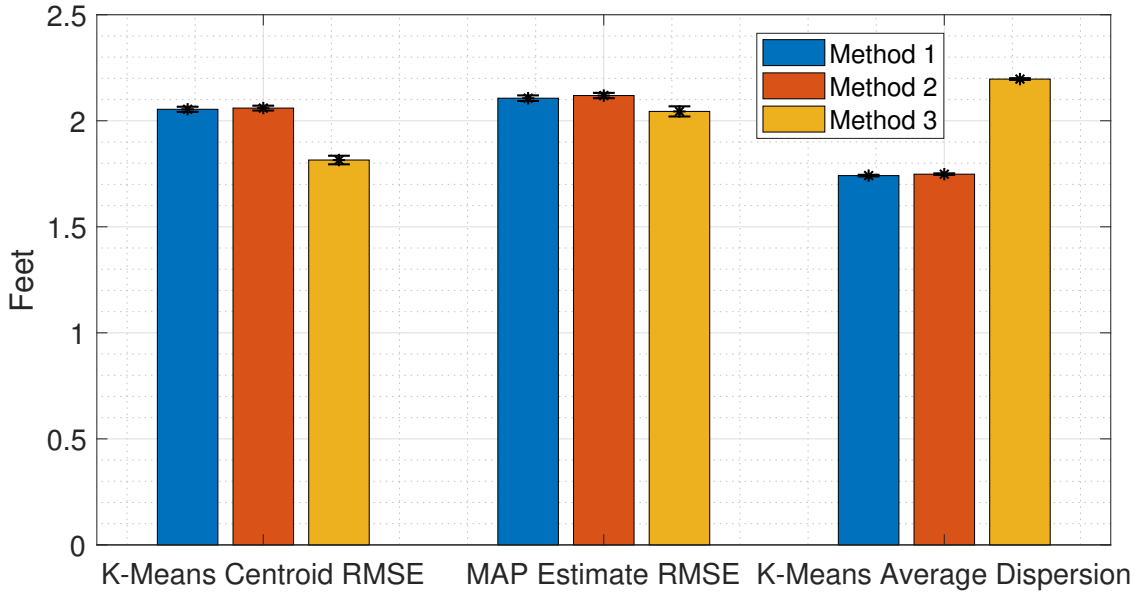

Figure 35: Experiment 2 RMSE and K-means averaged dispersion with 95% confidence intervals over 1000 realizations of the dynamic path for full path duration, with 20% packet loss.

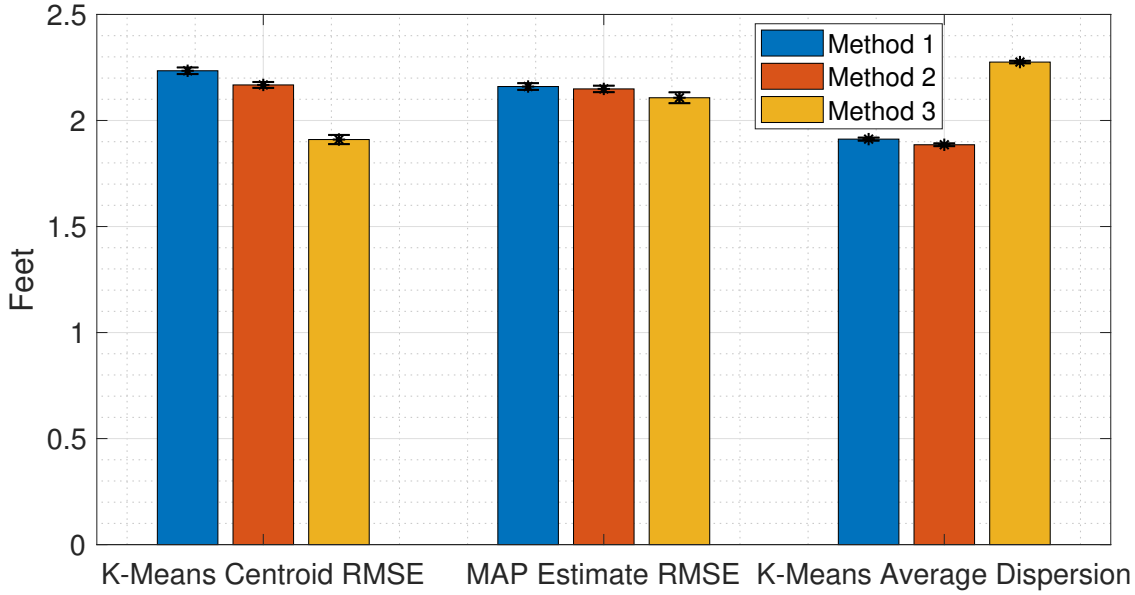

Figure 36: Experiment 2 RMSE and K-means averaged dispersion with 95% confidence intervals over 1000 realizations of the dynamic path for full path duration, with 50% packet loss.

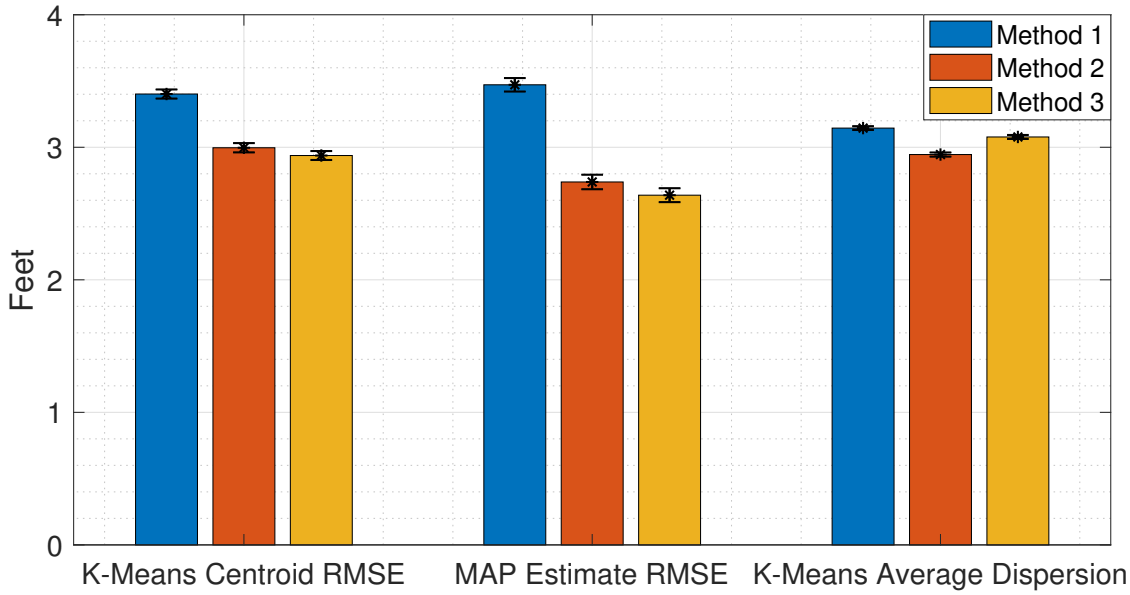

Figure 37: Experiment 2 RMSE and K-means averaged dispersion with 95% confidence intervals over 1000 realizations of the dynamic path during steady state runtime, with 85% packet loss.

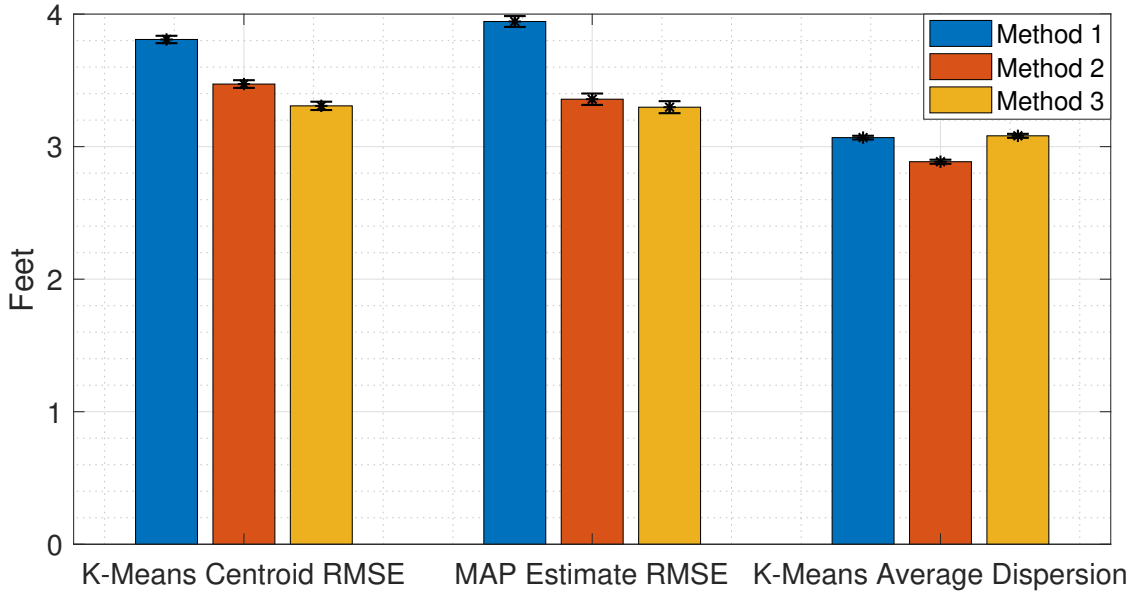

Figure 38: Experiment 2 RMSE and K-means averaged dispersion with 95% confidence intervals over 1000 realizations of the dynamic path for full path duration, with 85% packet loss.

1.2 Experiment 3 Results

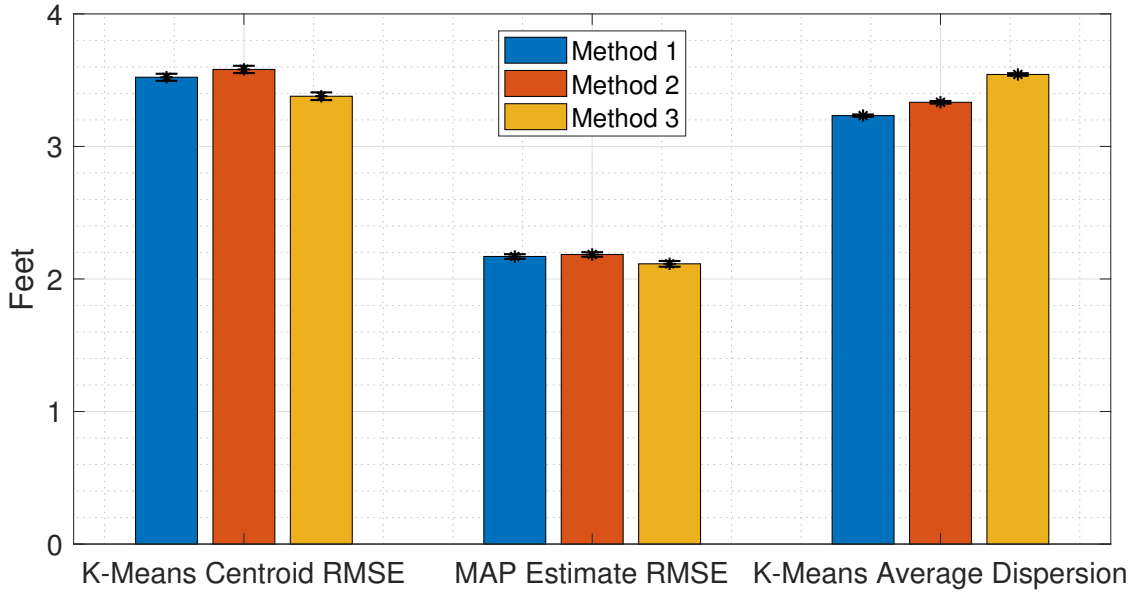

Figure 39: Experiment 3 RMSE and K-means averaged dispersion with 95% confidence intervals over 1000 realizations of the dynamic path for full path duration, with 0% packet loss.

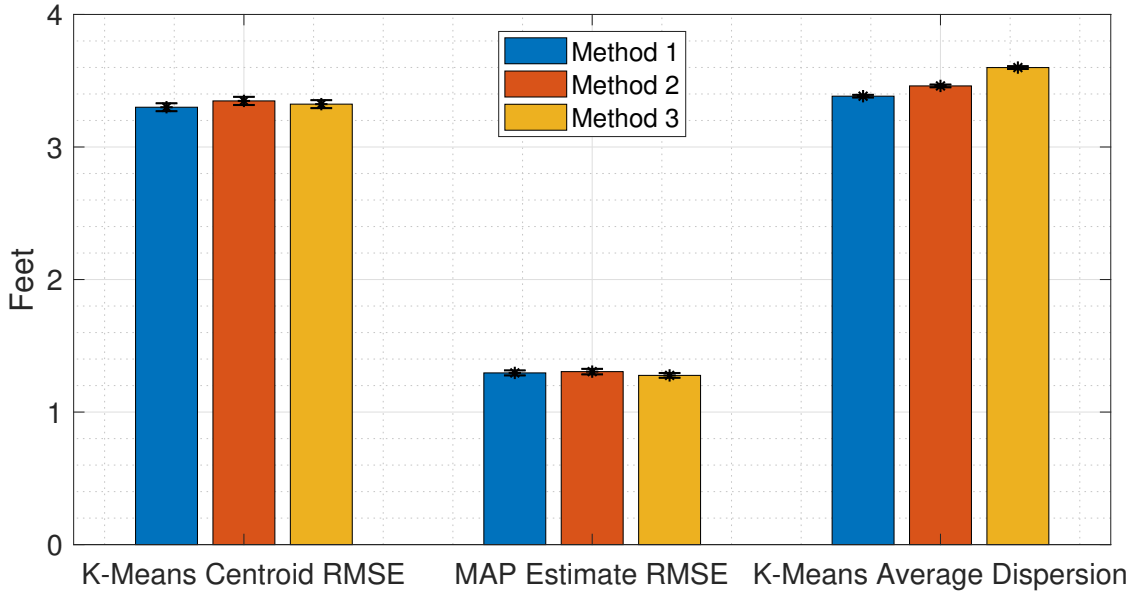

Figure 40: Experiment 3 RMSE and K-means averaged dispersion with 95% confidence intervals over 1000 realizations of the dynamic path during steady state runtime, with 20% packet loss.

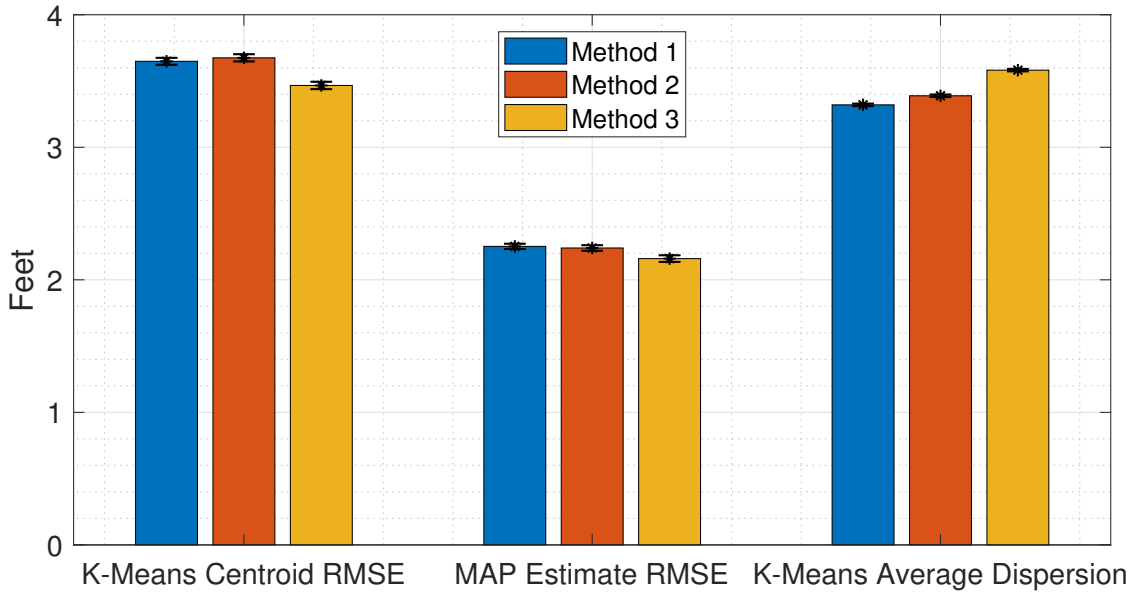

Figure 41: Experiment 3 RMSE and K-means averaged dispersion with 95% confidence intervals over 1000 realizations of the dynamic path for full path duration, with 20% packet loss.

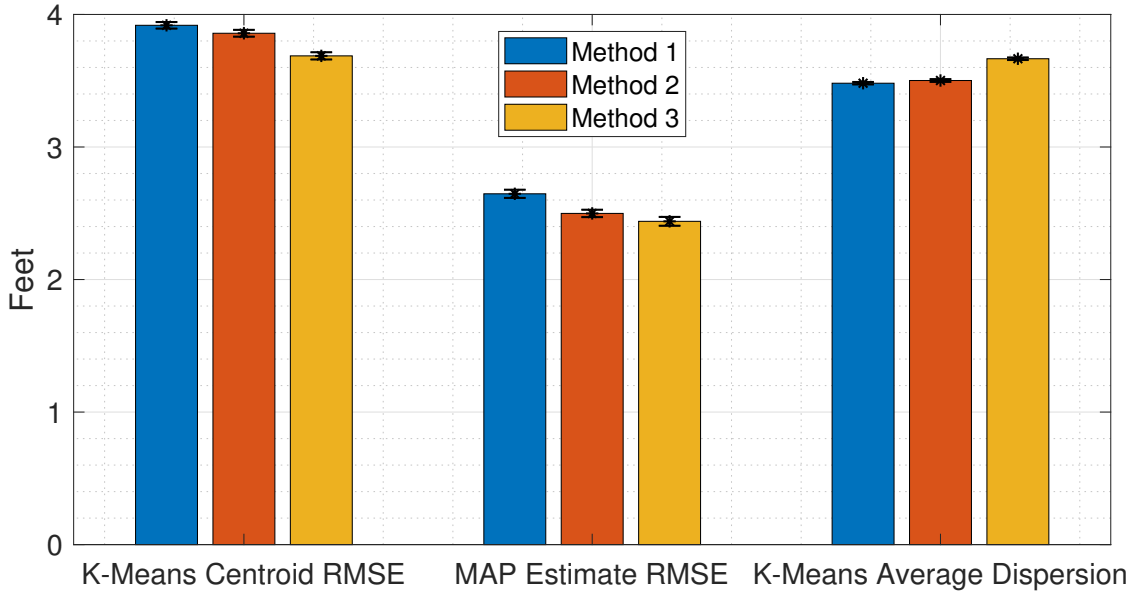

Figure 42: Experiment 3 RMSE and K-means averaged dispersion with 95% confidence intervals over 1000 realizations of the dynamic path for full path duration, with 50% packet loss.

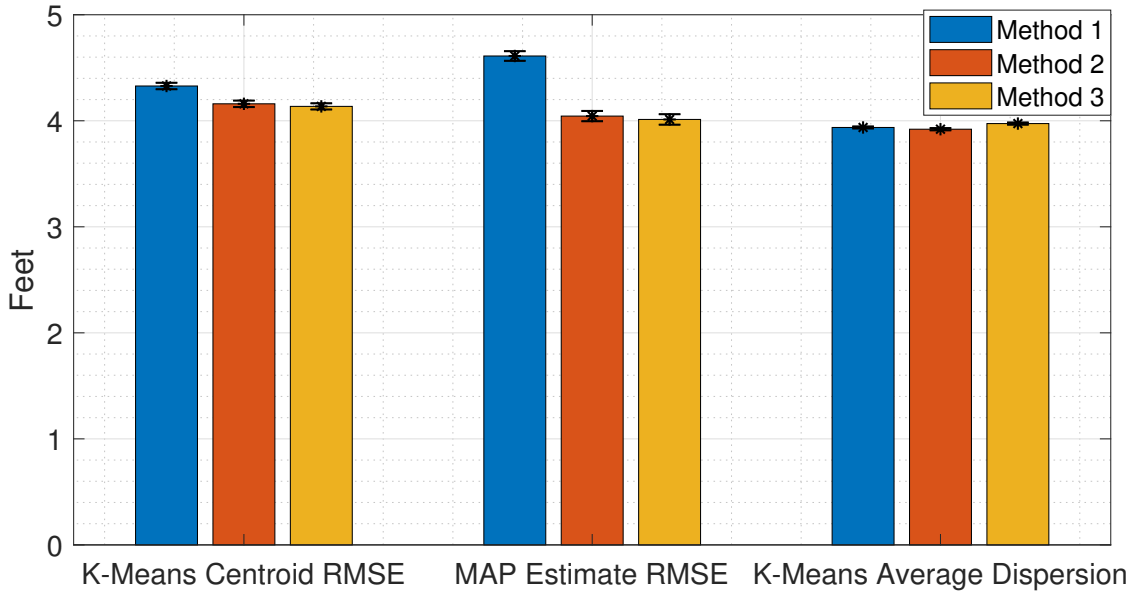

Figure 43: Experiment 3 RMSE and K-means averaged dispersion with 95% confidence intervals over 1000 realizations of the dynamic path during steady state runtime, with 85% packet loss.

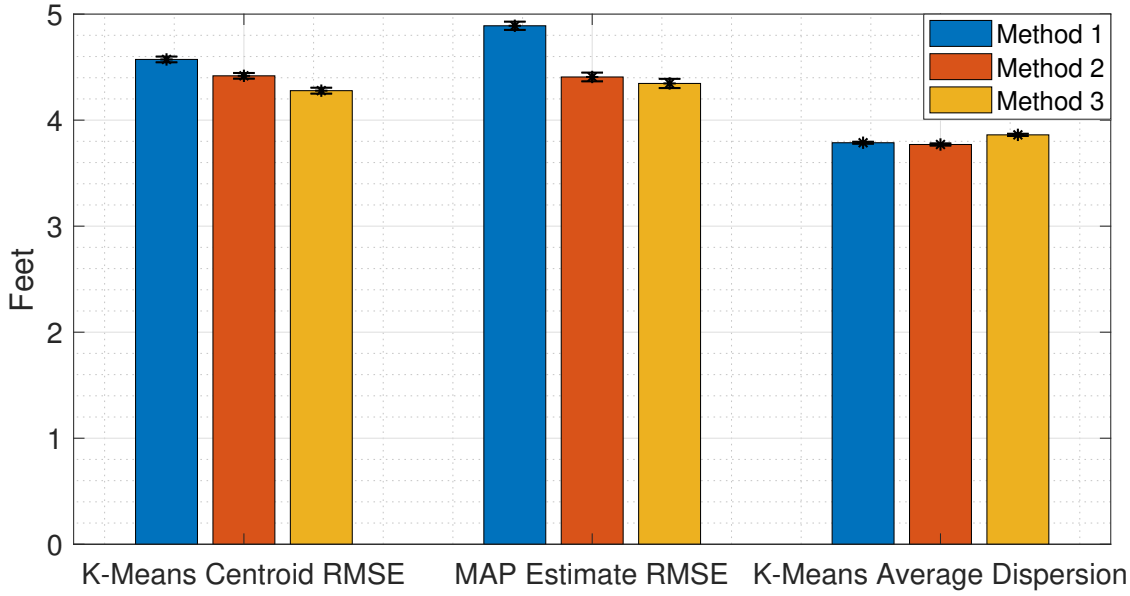

Figure 44: Experiment 3 RMSE and K-means averaged dispersion with 95% confidence intervals over 1000 realizations of the dynamic path for full path duration, with 85% packet loss.

1.3 Experiment 4 Results

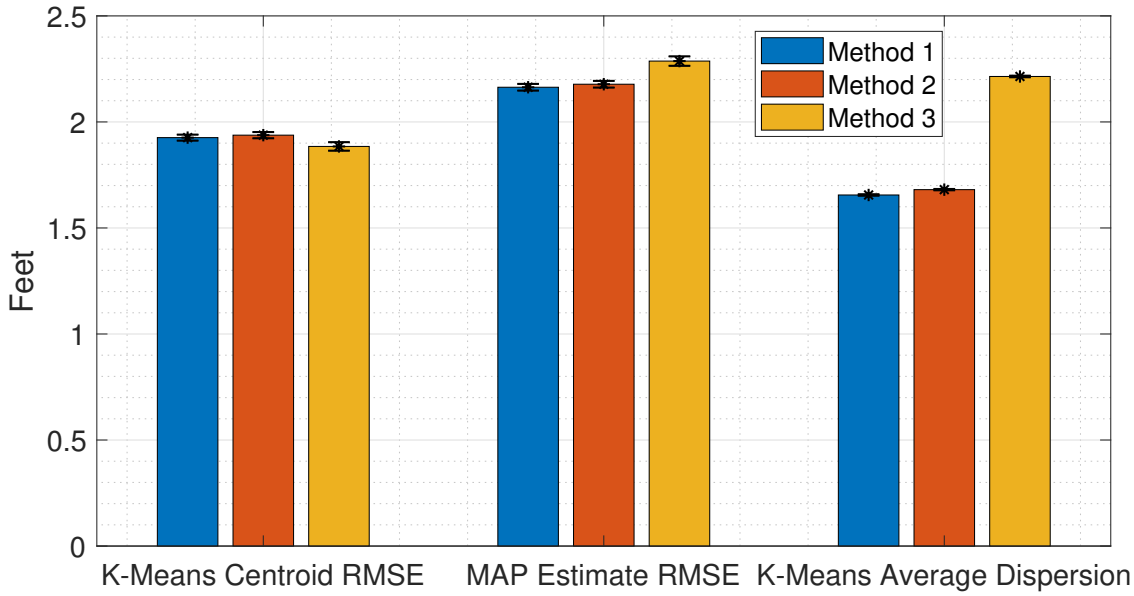

Figure 45: Experiment 4 RMSE and K-means averaged dispersion with 95% confidence intervals over 1000 realizations of the dynamic path for full path duration, with 0% packet loss.

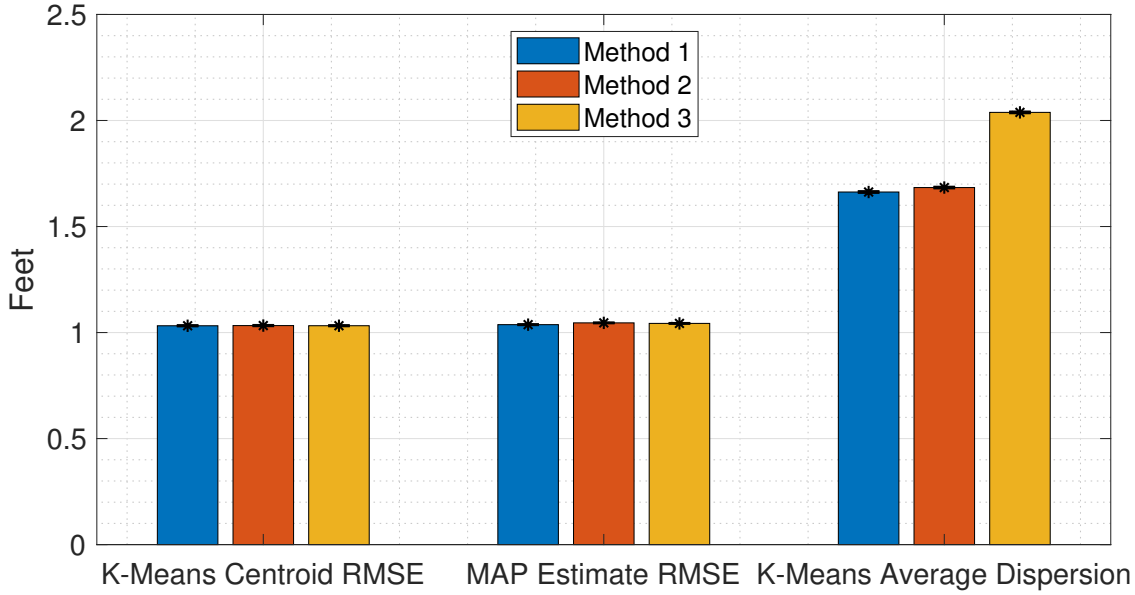

Figure 46: Experiment 4 RMSE and K-means averaged dispersion with 95% confidence intervals over 1000 realizations of the dynamic path during steady state runtime, with 20% packet loss.

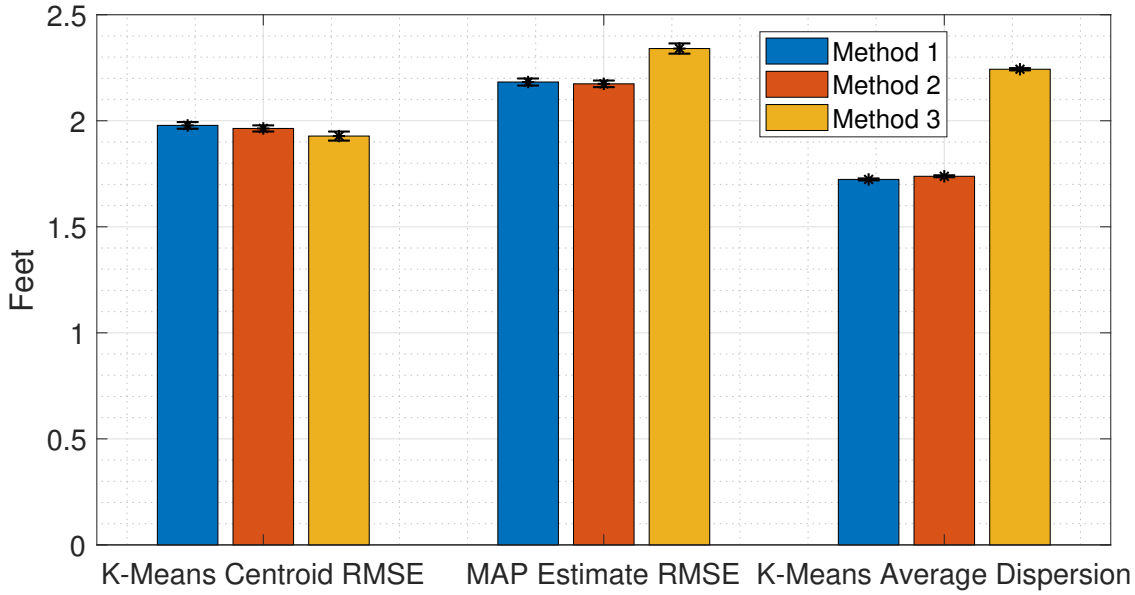

Figure 47: Experiment 4 RMSE and K-means averaged dispersion with 95% confidence intervals over 1000 realizations of the dynamic path for full path duration, with 20% packet loss.

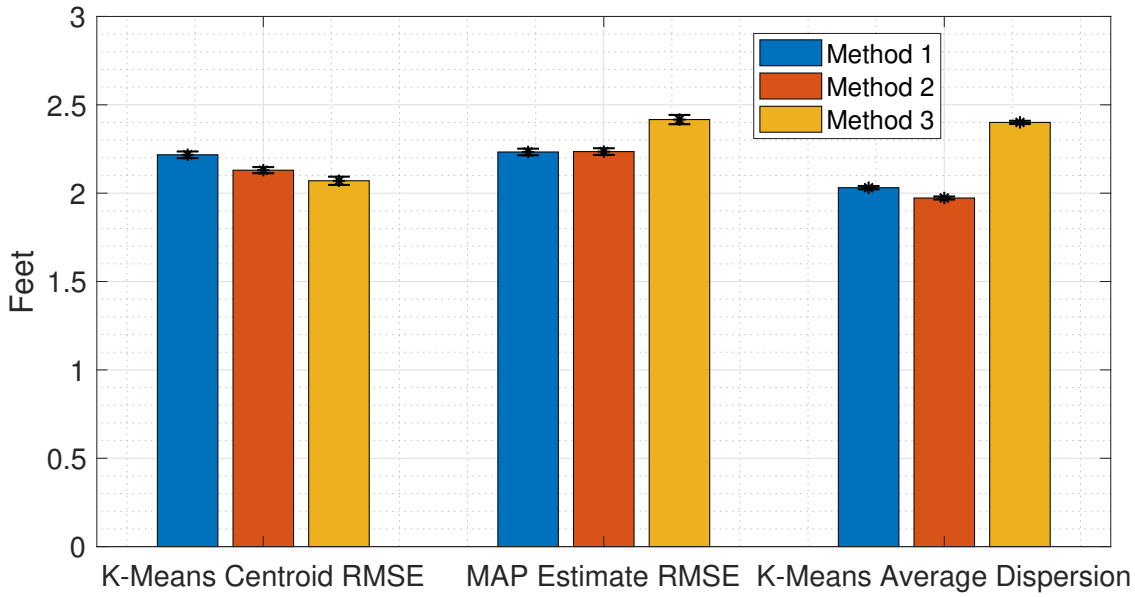

Figure 48: Experiment 4 RMSE and K-means averaged dispersion with 95% confidence intervals over 1000 realizations of the dynamic path for full path duration, with 50% packet loss.

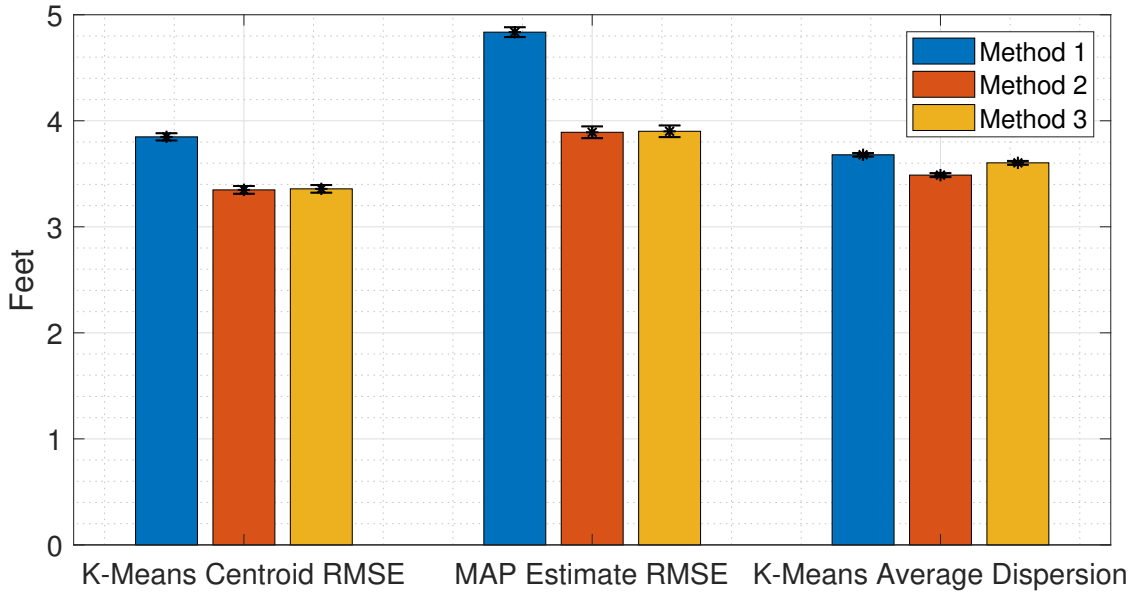

Figure 49: Experiment 4 RMSE and K-means averaged dispersion with 95% confidence intervals over 1000 realizations of the dynamic path during steady state runtime, with 85% packet loss.

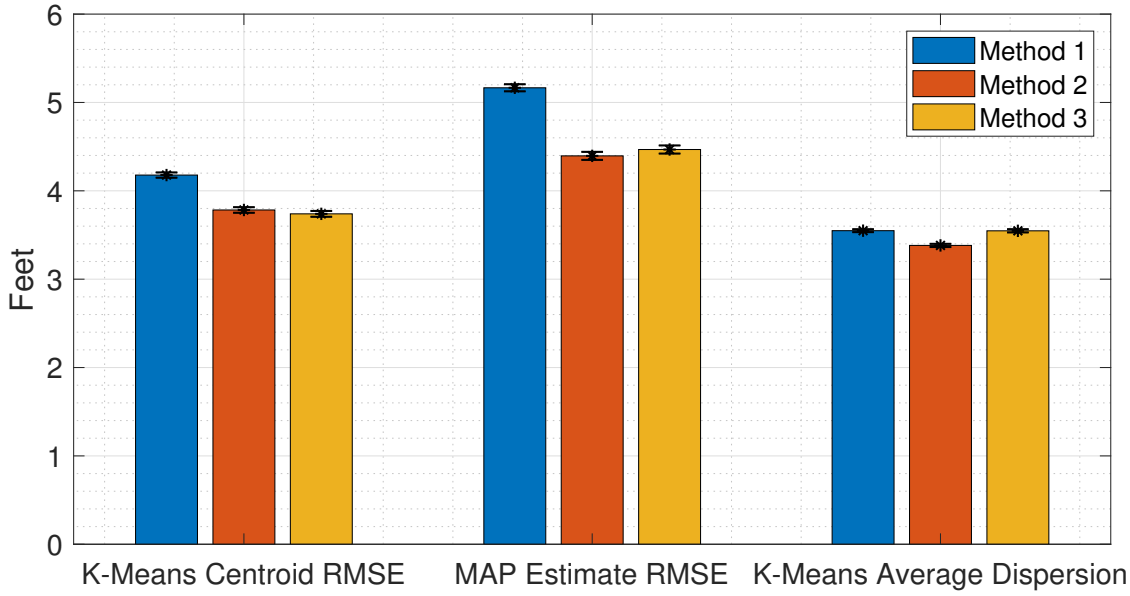

Figure 50: Experiment 4 RMSE and K-means averaged dispersion with 95% confidence intervals over 1000 realizations of the dynamic path for full path duration, with 85% packet loss.

1.4 Experiment 5 Results

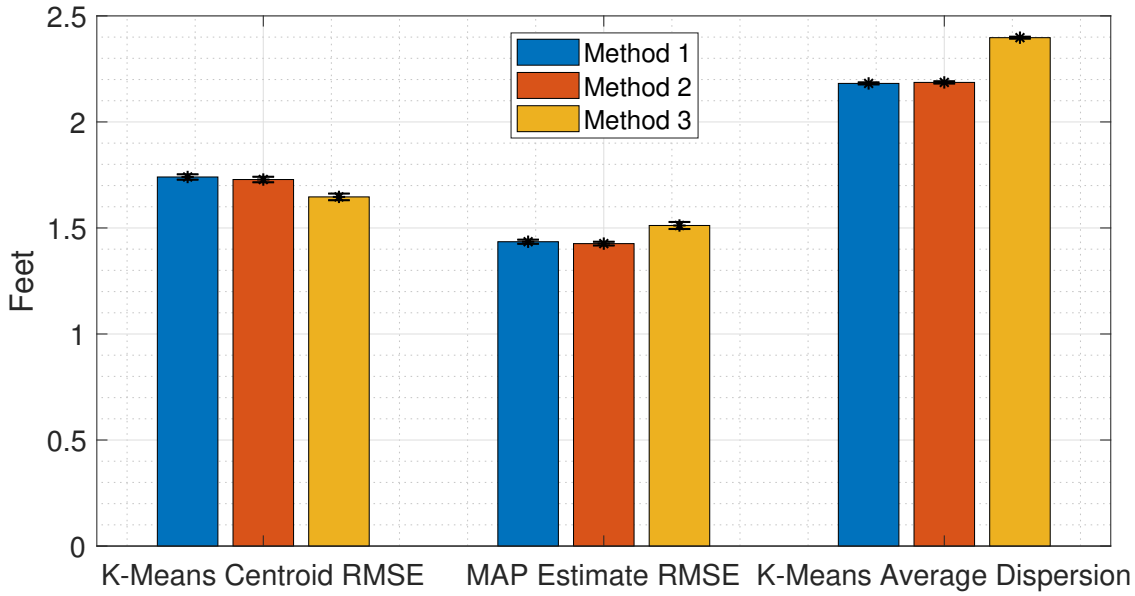

Figure 51: Experiment 5 RMSE and K-means averaged dispersion with 95% confidence intervals over 1000 realizations of the dynamic path for full path duration, with 0% packet loss.

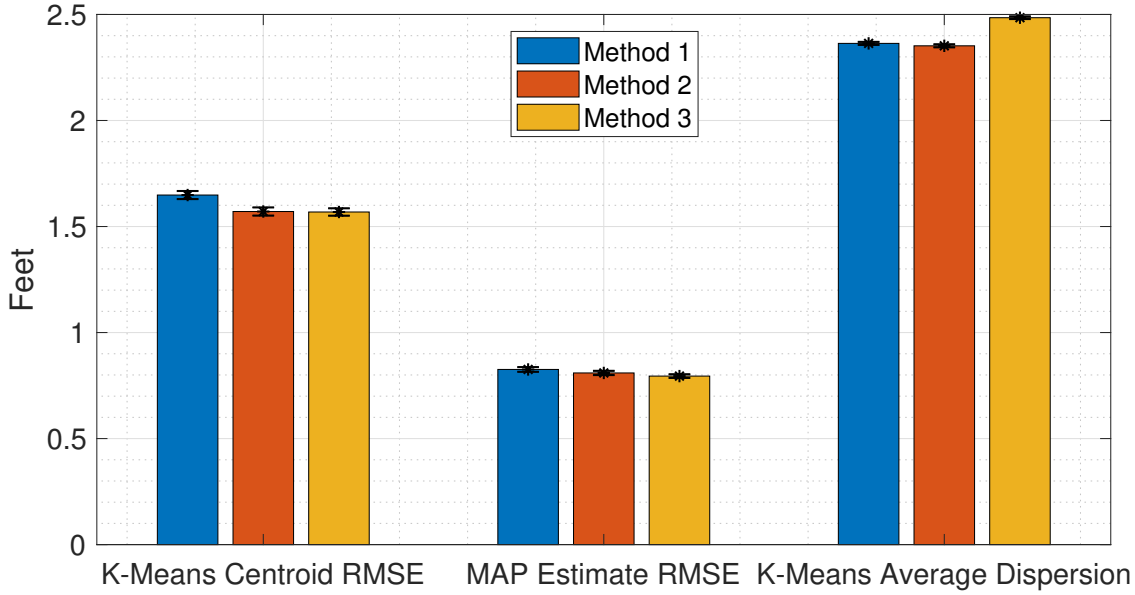

Figure 52: Experiment 5 RMSE and K-means averaged dispersion with 95% confidence intervals over 1000 realizations of the dynamic path during steady state runtime, with 20% packet loss.

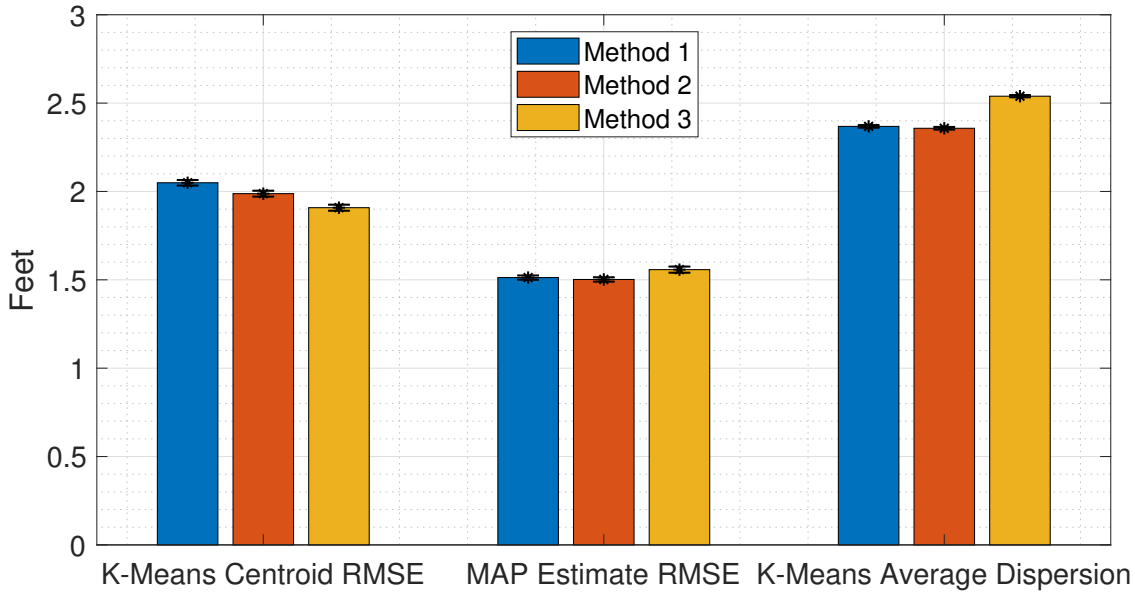

Figure 53: Experiment 5 RMSE and K-means averaged dispersion with 95% confidence intervals over 1000 realizations of the dynamic path for full path duration, with 20% packet loss.

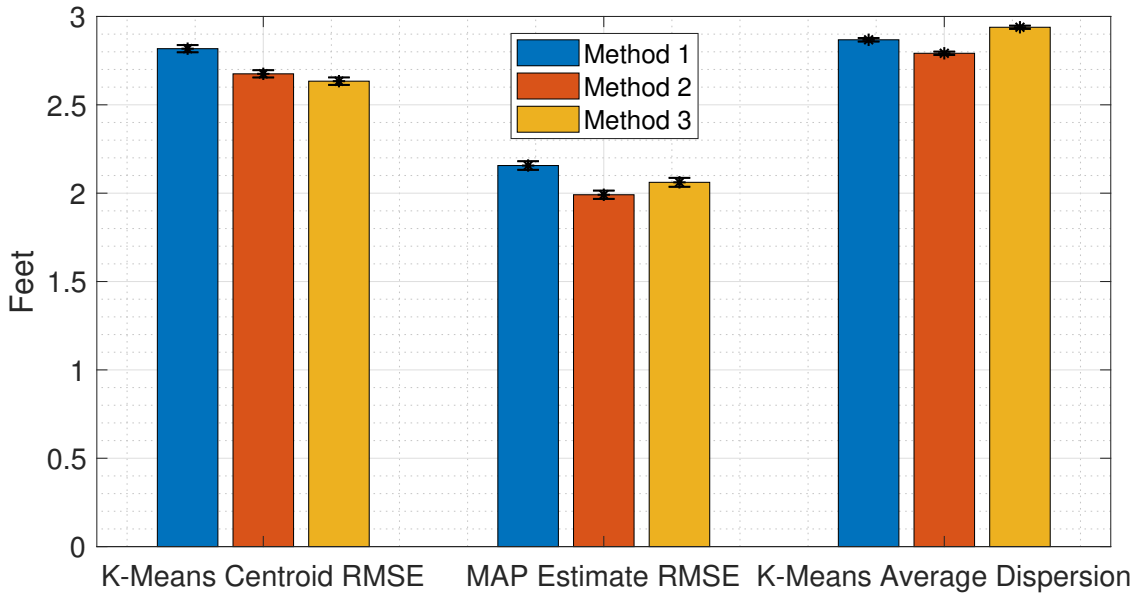

Figure 54: Experiment 5 RMSE and K-means averaged dispersion with 95% confidence intervals over 1000 realizations of the dynamic path for full path duration, with 50% packet loss.

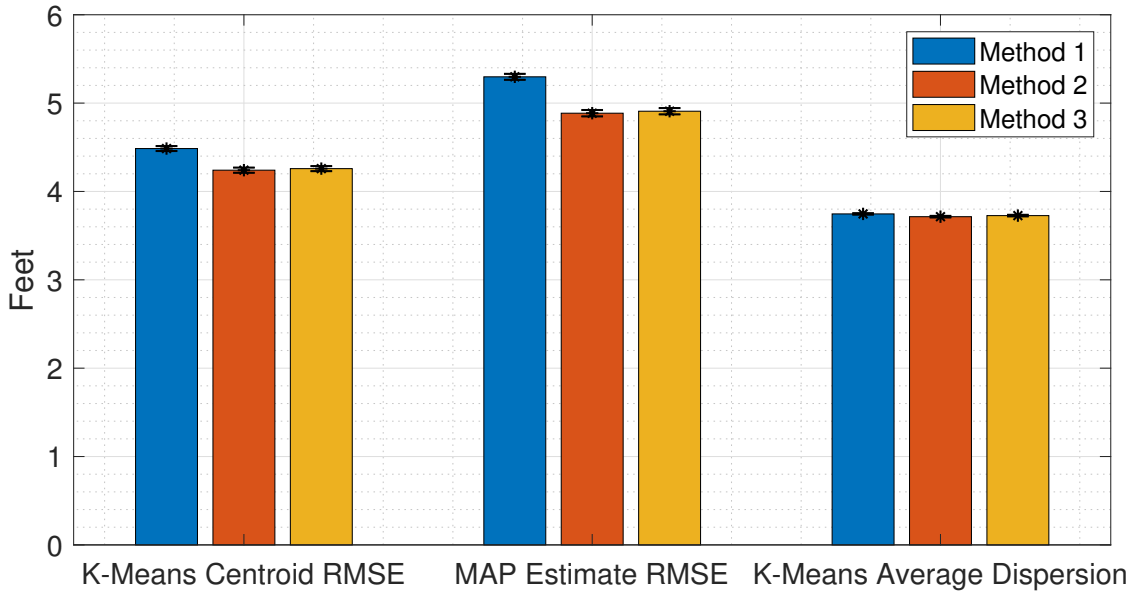

Figure 55: Experiment 5 RMSE and K-means averaged dispersion with 95% confidence intervals over 1000 realizations of the dynamic path during steady state runtime, with 85% packet loss.

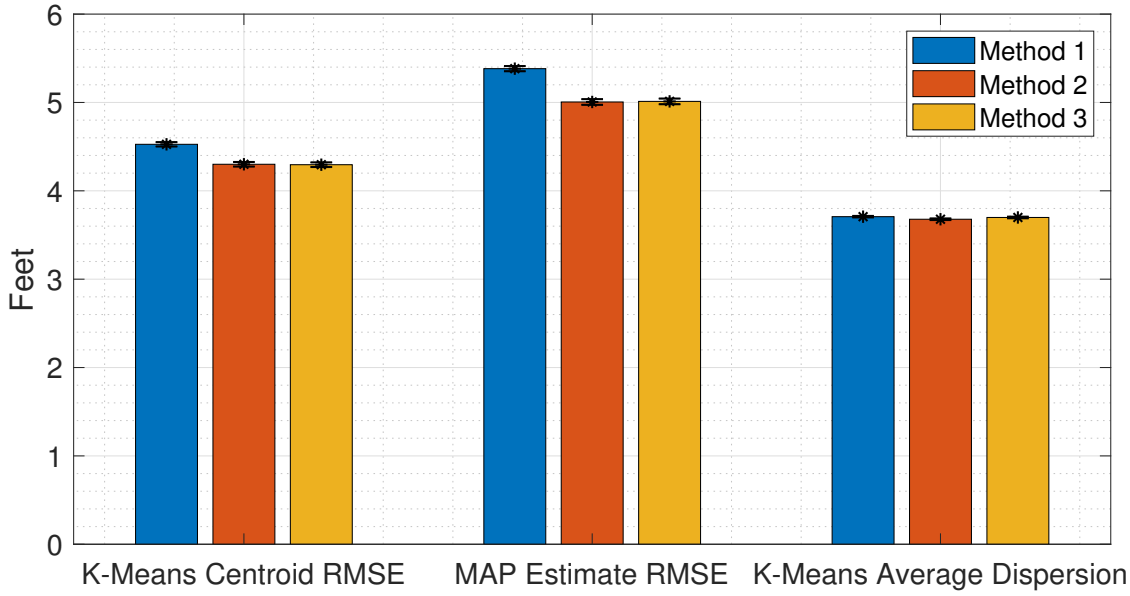

Figure 56: Experiment 5 RMSE and K-means averaged dispersion with 95% confidence intervals over 1000 realizations of the dynamic path for full path duration, with 85% packet loss.

Bibliography

1. S. Palipana, B. Pietropaoli, and D. Pesch, "Recent advances in RF-based passive device-free localisation for indoor applications," *Ad Hoc Networks*, vol. 64, pp. 80–98, 2017.

2. T. Van, *Characterizing Multiple Wireless Sensor Networks for Large-Scale Radio Tomography*. Master's thesis, ENG, AFIT, Wright-Patterson AFB, OH, 2015.

3. C. Vergara, *Multi-Sensor Data Fusion Between Radio Tomographic Imaging and Noise Radar*. Master's thesis, ENG, AFIT, Wright-Patterson AFB, OH, 2019, no. March.

4. J. Nishida, *Estimating Single and Multiple Target Locations Using K-Means Clustering with Radio Tomographic Imaging in Wireless Sensor Networks*. Master's thesis, ENG, AFIT, Wright-Patterson AFB, OH, 2015.

5. J. Xiao, Z. Zhou, Y. Yi, and L. M. Ni, "A Survey on Wireless Indoor Localization from the Device Perspective," *ACM Computing Surveys*, vol. 49, no. 2, pp. 1–31, 2016.

6. J. Wilson and N. Patwari, "Radio tomographic imaging with wireless networks," *IEEE Transactions on Mobile Computing*, vol. 9, no. 5, pp. 621–632, 2010.

7. V. Smallbon, T. Potie, M. D'Souza, A. Postula, and M. Ros, "Implementation of Radio Tomographic Imaging based Localisation using a 6LoWPAN Wireless Sensor Network," *2015 12th International Joint Conference on e-Business and Telecommunications (ICETE)*, vol. 06, pp. 27–32, 2015.

8. A. C. De Alwis, C. Keppitiyagama, A. Sayakkara, and D. Piumwardane, "Radio tomographic imaging using extremely resource constrained devices," *16th Inter-*

national Conference on Advances in ICT for Emerging Regions, ICTer 2016 - Conference Proceedings, pp. 222–228, 2017.

9. B. Beck, X. Ma, and R. Baxley, "Ultrawideband tomographic imaging in uncalibrated networks," *IEEE Transactions on Wireless Communications*, vol. 15, no. 9, pp. 6474–6486, 2016.

10. J. Wilson and N. Patwari, "See-through walls: Motion tracking using variance-based radio tomography networks," *IEEE Transactions on Mobile Computing*, vol. 10, no. 5, pp. 612–621, 2011.

11. M. Bocca, O. Kaltiokallio, and N. Patwari, "Radio tomographic imaging for ambient assisted living," in *Communications in Computer and Information Science*, vol. 362, 2013, pp. 108–130.

12. M. Cimdins and H. Hellbruck, "Modeling received signal strength and multipath propagation effects of moving persons," in *14th Workshop on Positioning, Navigation and Communications*, January, 2017, pp. 1–6.

13. M. Cimdins, M. Pelka, and H. Hellbrück, "Sundew: Design and Evaluation of a Model-Based Device-Free Localization System," in *9th International Conference on Indoor Positioning and Indoor Navigation*, September, 2018, pp. 24–27.

14. M. Bocca, A. Luong, N. Patwari, and T. Schmid, "Dial it in: Rotating RF sensors to enhance radio tomography," in *11th Annual IEEE International Conference on Sensing, Communication, and Networking (SECON)*, June-July, 2014, pp. 600–608.

15. B. Beck, R. Baxley, and X. Ma, "Improving Radio Tomographic Images using multipath signals," *IEEE International Conference on Wireless Information Technology and Systems (ICWITS)*, pp. 1–4, November, 2012.

16. O. Kaltiokallio, R. Hostettler, N. Patwari, and R. Jäntti, "Recursive Bayesian Filters for RSS-Based Device-Free Localization and Tracking," in *9th IEEE International Conference on Indoor Positioning and Indoor Navigation (IPIN)*, September, 2018, pp. 1–8.

17. K. Huang, S. Tan, Y. Luo, X. Guo, and G. Wang, "Enhanced radio tomographic imaging with heterogeneous Bayesian compressive sensing," *Pervasive and Mobile Computing*, vol. 40, pp. 450–463, 2017. [Online]. Available: http://dx.doi.org/10.1016/j.pmcj.2017.03.001

18. Y. Guo, K. Huang, N. Jiang, X. Guo, Y. Li, and G. Wang, "An exponential-rayleigh model for RSS-based device-free localization and tracking," *IEEE Transactions on Mobile Computing*, vol. 14, no. 3, pp. 484–494, 2015.

19. Y. Zhao and N. Patwari, "Noise reduction for variance-based radio tomographic localization," in *8th Annual Communications Society Conference on Sensor, Mesh and Ad Hoc Communications and Networks (SECON)*, no. 3, June, 2011, pp. 155–157.

20. Y. Li, X. Chen, M. Coates, and B. Yang, "Sequential Monte Carlo radio-frequency tomographic tracking," in *Proceedings - IEEE International Conference on Acoustics, Speech and Signal Processing (ICASSP)*, May, 2011, pp. 3976–3979.

21. R. K. Martin, C. Anderson, R. W. Thomas, and A. S. King, "Modelling and analysis of radio tomography," in *4th International IEEE Workshop on Computational Advances in Multi-Sensor Adaptive Processing (CAMSAP)*, December, 2011, pp. 377–380.

22. R. K. Martin, A. Folkerts, and T. Heinl, "Accuracy vs. resolution in radio tomography," *IEEE Transactions on Signal Processing*, vol. 62, no. 10, pp. 2480–2491, 2014.

23. N. Patwari and P. Agrawal, "NeSH: A joint shadowing model for links in a multi-hop network," *IEEE International Conference on Acoustics, Speech and Signal Processing - Proceedings (ICASSP)*, pp. 2873–2876, March-April, 2008.

24. N. Patwari and J. Wilson, "Spatial models for human motion-induced signal strength variance on static links," *IEEE Transactions on Information Forensics and Security*, vol. 6, no. 3, pp. 791–802, 2011.

25. ——, "RF sensor networks for device-free localization: Measurements, models, and algorithms," in *Proceedings of the IEEE*, vol. 98, no. 11, 2010, pp. 1961–1973.

26. N. Patwari and P. Agrawal, "Effects of correlated shadowing: Connectivity, localization, and RF tomography," *Proceedings - International Conference on Information Processing in Sensor Networks (IPSN)*, pp. 82–93, April, 2008.

27. V. Rampa, G. G. Gentili, S. Savazzi, and M. D'Amico, "Electromagnetic models for device-free localization applications," in *IEEE-APS Topical Conference on Antennas and Propagation in Wireless Communications (APWC)*, January, 2017, pp. 4–7.

28. V. Rampa, S. Savazzi, M. Nicoli, and M. D'Amico, "Physical Modeling and Performance Bounds for Device-free Localization Systems," *IEEE Signal Processing Letters*, vol. 22, no. 11, pp. 1864–1868, 2015.

29. C. Zhu and Y. Chen, "Distance attenuation-based elliptical weighting-g model in radio tomography imaging," *IEEE Access*, vol. 6, pp. 34 691–34 695, 2018.

30. Q. Wang, H. Yiitler, R. Jäntti, and X. Huang, "Localizing Multiple Objects Using Radio Tomographic Imaging Technology," *IEEE Transactions on Vehicular Technology*, vol. 65, no. 5, pp. 3641–3656, 2016.

31. H. Yigitler, R. Jantti, O. Kaltiokallio, and N. Patwari, "Detector Based Radio Tomographic Imaging," *IEEE Transactions on Mobile Computing*, vol. 17, no. 1, pp. 58–71, 2017. [Online]. Available: http://arxiv.org/abs/1604.03083

32. C. Y. Chiu and D. Dujovne, "Experimental characterization of radio tomographic imaging using Tikhonov's regularization," *IEEE Biennial Congress of Argentina (ARGENCON)*, pp. 468–472, June, 2014.

33. H. Liu, Z. H. Wang, X. Y. Bu, and J. P. An, "Image reconstruction algorithms for radio tomographic imaging," *Proceedings - IEEE International Conference on Cyber Technology in Automation, Control, and Intelligent Systems (CYBER)*, no. 1, pp. 48–53, May, 2012.

34. D. Zhang, M. Jian, Q. Chen, and L. M. Ni, "An RF-based system for tracking transceiver-free objects," *Proceedings - Fifth Annual IEEE International Conference on Pervasive Computing and Communications (PerCom)*, pp. 135–144, March, 2007.

35. S. Denis, R. Berkvens, G. Ergeerts, and M. Weyn, "Multi-frequency sub-1 GHz radio tomographic imaging in a complex indoor environment," *International Conference on Indoor Positioning and Indoor Navigation (IPIN)*, September, 2017.

36. B. R. Hamilton, *Applications of Bayesian Filtering in Wireless Networks : Clock Synchronization, Localization, and RF Tomography.* Ph.D. dissertation, Georgia Inst. of Technol., Atlanta, GA, 2012.

37. C. R. Anderson, R. K. Martin, T. O. Walker, and R. W. Thomas, "Radio tomography for roadside surveillance," *IEEE Journal on Selected Topics in Signal Processing*, vol. 8, no. 1, pp. 66–79, 2014.

38. M. A. Kanso and M. G. Rabbat, "Efficient Detection and Localization of Assets in Emergency Situations," *3rd Intl. Symposium on Medical Information & Communication Technology (ISMICT)*, February, 2009.

39. ——, "Compressed RF tomography for wireless sensor networks: Centralized and decentralized approaches," *Lecture Notes in Computer Science (including subseries Lecture Notes in Artificial Intelligence and Lecture Notes in Bioinformatics)*, vol. 5516 LNCS, no. 1, pp. 173–186, 2009.

40. J. A. Roberts and J. R. Abeysinghe, "Two-state Rician model for predicting indoor wireless communication performance," *IEEE International Conference on Communications*, vol. 1, pp. 40–43, June, 1995.

41. C. Sun, F. Gao, H. Liu, S. Xu, and J. An, "A Radio Tomographic Imaging Method Using Channel State Information and Image Fusion," *Proceedings - 8th IEEE International Conference on Electronics Information and Emergency Communication (ICEIEC)*, no. 2, pp. 223–227, June, 2018.

42. O. Kaltiokallio, R. Jäntti, and N. Patwari, "ARTI: An Adaptive Radio Tomographic Imaging System," *IEEE Transactions on Vehicular Technology*, vol. 66, no. 8, pp. 7302–7316, 2017.

43. S. M. Kay, *Fundamentals of Statistical Signal Processing: Estimation Theory.* Upper Saddle River, NJ, USA: Prentice Hall, 1993.

44. S. Särkkä, *Bayesian Filtering and Smoothing.* Cambridge University Press, 2013.

Acronyms

6LoWPAN IPv6 Over Low-Power Wireless Personal Area Networks. 2

AFIT Air Force Institute of Technology. 6, 29, 37, 38, 39, 54

AWGN additive white Gaussian noise. 14, 37, 38

DFL device-free localization. 1, 5

DFPL device-free, passive localization. iv, 1

EKF extended Kalman Filter. 24, 25, 27, 29, 31

GMM Gaussian mixture model. 14

GPS Global Positioning System. 5

GUI graphical user interface. 29

MAP maximum a posteriori. 19, 20, 21, 26, 42, 43, 52, 53, 54, 61, 63, 65, 67, 70

MOUT military operations in urban terrain. iv, 2, 69

NeSh Network Shadowing. 11, 12, 46

PDF probability density function. 21

RF radio frequency. 1, 2, 5, 29

RFID radio frequency identification device. 5

RMSE root-mean-squared error. ix, x, xi, xii, xiii, 42, 43, 52, 53, 54, 53, 54, 55, 56, 61, 63, 65, 67, 70, 72, 76, 80, 84

RSS received signal strength. 1, 3, 5, 6, 8, 9, 11, 12, 16, 17, 21, 22, 26, 27, 29, 30, 31, 32, 33, 34, 35, 36, 37, 38, 43, 52, 69, 70, 71

RTI radio tomographic imaging. iv, 1, 2, 3, 4, 5, 6, 7, 8, 9, 10, 11, 14, 15, 16, 18, 19, 22, 25, 26, 29, 32, 34, 37, 38, 39, 54, 69, 71

SPAN Sensing and Processing Across Networks. 6

TDMA time division multiple access. 6, 33

UWB ultra-wideband. 2

WSN wireless sensor network. iv, viii, xiv, 1, 2, 5, 6, 16, 17, 19, 29, 30, 35, 36, 37, 38, 37, 38, 42, 46, 52, 56, 67, 69, 70, 71